Oxford Materials Department

Atomic Scale Characterisation of Radiation Damage and Radiation Induced Precipitation in Tungsten-Rhenium Alloys

---

DPhil Thesis

Alan Xu

St Edmund Hall

A Thesis Submitted for the Degree of Doctor of Philosophy

Trinity 2015

To My Family

“If I have seen further, it is by standing on the shoulder of giants”

Isaac Newton

Abstract

Tungsten is considered the prime candidate material for plasma facing components within fusion reactors. However, exposure of tungsten to neutron flux brings about transmutation of tungsten into by-products: Re, Os and Ta. Under increasing levels of radiation damage, irradiation induced clustering/precipitation takes place that embrittles and thus reduces lifetime of such tungsten components. This thesis was undertaken to explore this subject on a deeper level.

There are three components to this study. The first part considers the effect of Re content on irradiation induced clustering. Lab-made plate W-xRe (x: 2, 5, 10 and 25at.%) alloys were exposed to 1.2, 3.9 and 33dpa, self-ion irradiated at 773K. Analysis of cluster number density and volume fraction found they increase with damage level and bulk Re content. Based on these trends and existing literature data, a hypothesis was proposed suggesting clusters originate from vacancy clusters. Also, at 33dpa, rod shaped clusters form in W-25Re alloys while spherical clusters are present in other alloys. The clusters show close correspondence with irradiation induced precipitates and appear to be precursor phase.

In the second part of this thesis, the effect of Os and Ta on cluster formation and alloy mechanical properties is examined. Lab-made plate W-1Re-1Os and W-2Re-1Ta alloys were irradiated at 33dpa at 573 and 773K and compared against control W-2Re alloy. At 33dpa and 573K, the Os and Ta presence suppresses cluster formation. Both ternary alloys contain smaller cluster diameter, composition, number density and volume fraction than the W-2Re alloy. However, at 33dpa and 773K, Os and Ta have opposing effects on cluster behaviour. Os increases the cluster nucleation rate and raises irradiation hardening (compared to W-2Re). Meanwhile, Ta presence decreased cluster number density and reduced the irradiation hardening (compared to W-2Re alloy). As well, Ta showed no evidence of clustering, only Re clusters form in the W-2Re-1Ta alloy.

The final aspect of the thesis analyzes the effect of material microstructure and external variables on cluster formation in W-Re alloys. Commercial wire form W-25Re alloy was irradiated at 1.2dpa at 573 and 773K as atom probe needles and bulk sample. The larger free surface on atom probe needle samples appears to act as a sink for self-interstitials and vacancies at both temperatures.

The effect of grain size and dislocation density was examined by irradiating commercial W-5Re wire (0.5-1µm diameter) and plate (1-3mm diameter) samples (annealed and unannealed) to 33dpa and 573K. It was found grain boundaries and dislocations act as defect sinks at 573K. Additionally, radiation enhanced Re grain boundary enrichment was observed for first time. The effect of grain size on cluster behaviour at 773K was also analysed. Commercial wire and lab-made plate W-3Re, W-5Re and W-25Re alloys were irradiated to 33dpa at 773K. The larger grain boundary area in wire samples is suspected of acting as a sink for self-interstitials leaving more vacancies for promoting cluster formation compared to lab-made samples.

The discoveries made in this thesis broaden our current understanding of irradiation induced phase formation in tungsten. Their implications on plasma facing component design are discussed as well as recommendations for improvements. Further, areas requiring further research in this field are also highlighted.

Preface

The work presented in this doctoral thesis has been carried out at the Department of Materials, University of Oxford from October 2011 to June 2015, under the supervision of Prof. Steve G. Roberts and Dr. Paul A. J. Bagot. All of the research carried out for this thesis is original and where the work of others has been included it has been clearly referenced and acknowledged. No part of this thesis has been submitted for a degree at this, or any other university. Some of the work has been published in peer reviewed journals and presented at conferences and seminars as detailed below:

Journals

A.Xu, C.Beck, D.E.J.Armstrong, K.Rajan, G.D.W.Smith, P.A.J.Bagot, S.G.Roberts; *"Ion-Iirradiation-Induced Clustering in W-Re and W-Re-Os Alloys: a Comparative Study Using Atom Probe Tomography and Nanoindentation Measurements"* **Acta Materialia, Volume 87, Pages 121-127.**

P.D.Edmondson, A.London, **A.Xu**, D.E.J.Armstrong, S.G.Roberts; *"Small-scale characterisation of irradiated nuclear materials: Part I - Microstructure"* **Journal of Nuclear Materials, Volume 462, Pages 369-373.**

M.Dagan, L.R.Hanna, **A.Xu**, S.G.Roberts, G.D.W.Smith, B.Gault, P.D.Edmondson, P.A.J.Bagot, M.Moody; *"Imaging of Radiation Damage Using Complementary Field Ion Microscopy and Atom Probe Tomography"* **Ultramicroscopy, In Press.**

Conferences

A.Xu, P.A.J.Bagot, S.G.Roberts; *(Presentation) "Low Dose Radiation Damage Study of W-Re Alloys for the Fusion Reactor Divertor"* **Euromat Conference, Sevilla, Spain (8-13 Sept 2013).**

A.Xu, P.A.J.Bagot, C.Beck, S.G.Roberts; *(Poster) "The Role of Re and Os Transmutation Species Formed in W Plasma Facing Components for Fusion Reactors: an Atomic Scale Investigation"* **Tungsten Workshop, Oxford, UK (23-25 Sept 2013).**

A.Xu, C.Beck, D.E.J.Armstrong, K.Rajan, P.A.J.Bagot, S.G.Roberts; *(Presentation) "Ion-Irradiation Induced Clustering in a W-Re and W-Re-Os Alloy"* **APT & M Conference, Stuttgart, Germany (31 Aug – 5 Sept 2014).**

M.Dagan, L.R.Hanna, **A.Xu**, S.G.Roberts, G.D.W.Smith, B.Gault, P.D.Edmondson, P.A.J.Bagot, M.Moody; *(Presentation) "3D Field Ion Microscopy: An Atom-by-Atom Reconstruction Approach for Characterization of Atomic Scale Radiation Damage in Fusion Related Materials"* **APT & M Conference, Stuttgart, Germany (31 Aug – 5 Sept 2014).**

G.Smith, **A.Xu**, L.Hanna, M.Dagan, P.Bagot, M.Moody; *(Presentation) "The Effect of Transmutation Elements on the Radiation Response of Tungsten Alloys"* **28th SOFT Conference, San Sebastian, Spain (29 Sept – 3 Oct 2014).**

D.Armstrong, **A.Xu**, P.Bagot, S.Roberts, B.Briton; *(Presentation) "A Multi Technique Study of the Radiation Hardening Response of Tungsten 5wt% Rhenium"* **MRS Fall Conference, Boston, USA (30 Nov – 5 Dec 2014).**

Acknowledgements

I would like to express my deepest gratitude to my supervisors Prof Steve G. Roberts and Dr Paul A. J. Bagot as well as my Mentor Prof George D. W. Smith. This thesis would not be possible without their support, patience and guidance from the very beginning. I am eternally grateful. As well, I am appreciative for the generous funding provided by EPSRC, Oxford Materials Department and St Edmund Hall which supported me financially during the four years of my DPhil. I am truly fortunate to have the opportunity to study in the UK not to mention, chance to develop my interest in material science growing up in Australia.

Special thanks go to the technicians which trained me on the many laboratory equipments at Oxford Materials. They are Dr Gareth Hughes, Dr Neil Young, Dr Bob Lloyd, Mr Laurie Walton, Mr Graham Wyatt, Mr Chris Salter and Ms Gabriella Chapman. Acknowledgement goes to Dr Nianhua Peng at National Ion Beam Facility, University of Surrey for conducting the irradiation experiments. I am also grateful to Dr Dave Armstrong and Mr Christian Beck for taking hardness test measurements of samples. Their work is appropriately acknowledged and referenced in this thesis.

I thoroughly enjoyed the helpful and relaxed atmosphere in the Oxford Atom Probe and the Materials for Fusion and Fission Power research groups. Big thanks go to Prof Michael Moody, Dr Phil Edmondson and all post-docs, DPhil students and Part II students who provided many useful discussions and suggestions.

Last but not least, thanks to my family and all my friends outside of work who supported me throughout my DPhil.

Table of Contents

Introduction

In 2014, the International Energy Agency published a report titled: “Key World Energy Statistics” detailing the world’s energy consumption between the years 1971 and 2012 [1]. Between these four decades, the global energy consumption roughly doubled showing no signs of plateau towards 2012. Of the various fuels used, a remarkable 80% of the world’s energy consumption is derived from fossil fuels an energy source known to have a long history of causing environmental degradation [1-3]. Not to mention, fossil fuel has been linked to the increase in global CO_2 content and is widely suspected of accelerating the climate change that is currently taking place globally [2, 3]. In order to meet the increasing energy demands as well as to help protect the natural environment, a clean, efficient and reliable energy source is needed. In fact, one of the most promising alternatives is nuclear energy, specifically fusion energy whose fuel can be derived from sea water, has zero CO_2 emission and produces no pollutants during operation [4, 5].

In designing and testing materials to be used to survive the harsh fusion reactor environment, the phenomenon of irradiation induced precipitation embrittlement arises and it presents critical materials challenge [6, 7]. It especially concerns tungsten, the material of choice for plasma facing components which transmutate into Re, Os and Ta under neutron exposure [8-10]. Understanding this phenomenon is important for optimising materials design and prolong tungsten lifetime. This thesis is focused on irradiation induced clusters, an intermediate stage which can aide in understanding the underlying mechanisms of precipitation [11, 12]. The fine scale of these clusters warrants a nanoscale analysis of their physical, chemical and

mechanical properties. It is achieved here using Atom Probe Tomography (APT), Transmission Electron Microscopy (TEM) and Nanoindentation [12].

This thesis is structured to begin with a literature survey in chapter 1, detailing various aspects of tungsten and its alloys in both irradiated and unirradiated conditions. Chapter 2 describes the materials, method and calibration tests involved with the experimental setup and data analysis. Chapters 3, 4 and 5 analyse the phenomenon of irradiation induced clustering / precipitation from three different yet inter-related perspectives. Chapter 3 illustrates the evolution of clusters with dose across a range of W-Re alloys (Re is the most prominent transmutation species) and different stages of hardening involved with radiation damage. Chapter 4 studies the effect of Os and Ta on Re clustering in ternary alloys. Chapter 5 considers the effect of dislocation density, grain size and temperature on commercial W-Re alloys. Its aim is to determine the efficiency of defect sinks on hindering development of clusters and how temperature affects clustering in other W-Re compositions. The thesis is summarised and concluded in chapter 6 and 7 while references are covered in chapter 8.

1. Literature Review

1.1 Introduction

A magnetic confinement fusion reactor is among the most promising source of energy for the coming century. It requires two fuels: deuterium which can be derived from sea water and tritium a non-naturally occurring element produced in-situ in a power plant via irradiating lithium. Their nuclei fuse under high temperatures of millions of degrees Celsius to release energy and by-products: neutron and helium atom. As little as 97 kg of deuterium and tritium is enough to power the whole world for a day [1]. Unlike fossil fuel power plants, fusion reactor generates zero pollutants and CO_2 gases [4].

The fusion technology has gone a long way since its first models built in the 1970s. The most recent achievements have been attained at Joint European Torus (JET), UK. Through maintaining a steady state operation for a record 5 seconds, the feasibility of producing fusion power was demonstrated. To scale these fusion research reactors to power-plant capacity, there are two more intermediate stages. The International Thermonuclear Experimental Reactor (ITER) is the next stage in fusion reactor development [13]. Its purpose is to demonstrate the sustainability of a fusion reaction for continuous periods longer than an hour [14, 15]. Once successful, the following phase is construction of DEMOnstration fusion reactor, which as the name suggests, intends to produce electrical energy on a small scale [5, 16, 17]. The neutron flux in ITER and DEMO fusion reactors are anticipated to generate a damage rate, measured in displacements per atom, of <1dpa/annum and 3 dpa/annum respectively [18, 19]. They are an order of magnitude smaller compared

to the final phase: full power fusion reactor whose annual dose would be >20dpa [20].

Within a fusion reactor, fusion reaction takes place within superheated plasma magnetically confined to circulating around a doughnut shaped hollow (tokamak) without touching the wall. To ensure the reaction is sustainable, a divertor component is introduced as shown in Figure 1.1.1 [21, 22]. The divertor is designed to filter out helium ash by undergoing direct contact with it reducing plasma energy down to gas phase [15, 16]. During operation, the divertor is heated to an exceptionally high temperature of 1200K in addition to helium ion bombardment [8, 9, 23, 24]. Non-divertor plasma facing components operate at lower temperatures of 773K but will still experience the same 14MeV neutron flux as the divertor.

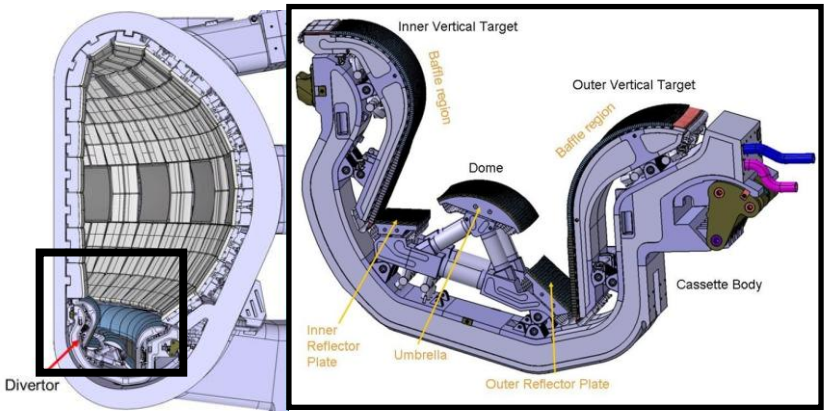

Figure 1.1.1 Schematic of a ITER divertor and its location within the Tokamak [25, 26].

Tungsten is a most promising candidate material for Plasma Facing Components (PFC). Its high melting point and creep resistance withstands the 1300K operating temperature while its high thermal conductivity fulfils its purpose of cooling down He ash [8, 9]. The greatest material challenge surrounds the effect of neutron irradiation which introduces dislocations and voids in tungsten having an embrittling effect [27, 28]. Additionally, neutrons transmute W into Re, Os and Ta that bring about

formation of radiation induced precipitates. PFCs harden significantly under such chemical and microstructural changes and the current understanding is very limited [29].

This literature review chapter begins by reporting physical, chemical and mechanical data on tungsten in §1.2. Tungsten's thermodynamic phase stabilities with solutes are covered in §1.3. §1.4 covers fundamentals of radiation damage and the defect-solute interactions. §1.5 and §1.6 report microstructural and mechanical changes of tungsten and its alloys under neutron and ion irradiation.

1.2 Tungsten: Properties and Neutron Transmutation

1.2.1 Physical Properties

Tungsten is a refractory metal with a melting point 3683K, thermal conductivity 173W.m^{-1}.K^{-1} and thermal expansion 4.5µm.m^{-1}.K^{-1} [30]. Tungsten recovers in the temperature range of 1073-1273K and recrystallises at ~1473K [31-33]. Tungsten has an atomic number of 74 and BCC crystal structure with a lattice spacing of 0.316nm (at room temperature). It has a high density 19.25g.cm^{-3}, atomic radius of 182pm [30].

1.2.2 Chemical Properties

At room temperature, tungsten is chemically inert and oxidation resistant. Tungsten is unreactive to most acids and alkali with the exception of concentrated nitric and hydrofluoric acids [30, 31]. Tungsten is even capable of withstanding corrosion at much higher temperatures above 1273K in the absence of oxygen. However, in atmospheres with oxygen present, tungsten forms a blue oxide above 673K. The oxidation behaviour becomes catastrophic above 1073K, as a brown oxide forms that has a tendency to sublime [30].

1.2.3 Mechanical Properties

Tungsten has a high Ductile to Brittle Transition Temperature (DBTT) 623-723K, below which, tungsten has a low fracture toughness of ~5MPa.$m^{1/2}$ [34-36]. The brittleness of tungsten is also characterised by limited dislocation mobility. At room

temperature, dislocations in Tungsten are only active on the (110)[111] and (112)[111] slip systems and are incapable of cross-slip. Above DBTT, the fracture toughness of Tungsten rises to 20-100MPa.$m^{1/2}$ for temperatures 673-1073K. The transition from brittleness to toughness is further shown in Figure 1.2.1, the results of Charpy Impact test for tungsten measured across a range of temperatures [34, 36]. The upper and lower limit of the measured Charpy energy drops to zero within the DBTT range, coinciding with the low fracture toughness.

Also at room temperature, Tungsten has a Young's Modulus 411GPa, Vickers Hardness 3.4-4.6GPa and ultimate tensile stress ~1000MPa [30]. Upon increasing the temperature to 1273K, its Young's modulus and ultimate yield stress drops in a linear manner to 3.7GPa and 75MPa at 1273K [30, 31]. The variation of these properties with temperature is quite large illustrated further in Figure 1.2.1a-b) for the tungsten tensile strength [34, 36]. Between 350 and 800K, there is an order of magnitude drop in the measured tensile strength.

1.2.4 Neutron Transmutation

Gilbert et al. simulated the Re, Os and Ta expected after years of operation in ITER and DEMO reactor [18, 19]. The transmutation of W into Re, Os, and Ta with time is shown in Figure 1.2.2 below with the main difference between them being the different neutron fluence experienced (mentioned earlier). It appears the transmutation issue is insignificant in ITER as only 0.15at.% Re formed after even 14 years of research reactor operation. It is significant in DEMO though as it reaches Re, Os and Ta content of 3.80, 1.38 and 0.55at.% respectively after 5 years of operation. Extrapolating to 12 years of operation predicts a solute content of 9.12,

4.32 and 1.32at.% which is a large change in composition. No simulations have been done for a full power fusion reactor. But, given the enormous annual damage expected: >20dpa (as compared to 1-3dpa for DEMO), the transmutation rate should be much more severe.

a)

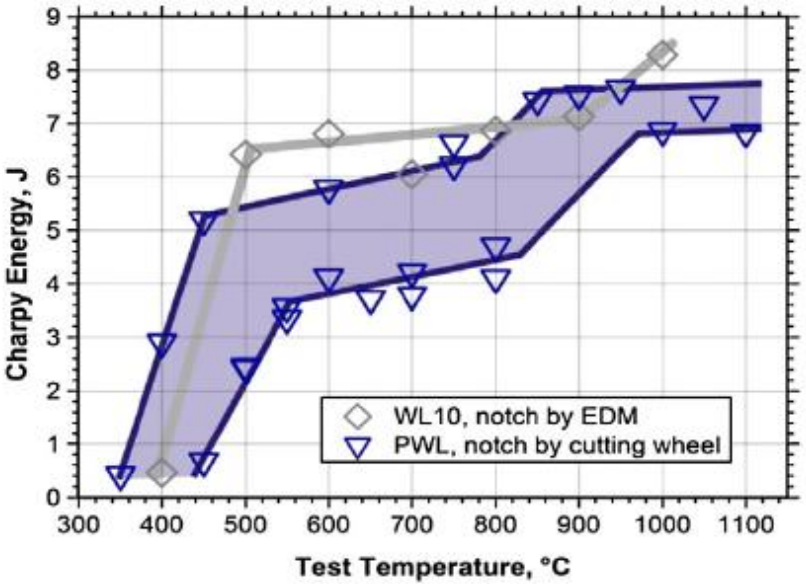

b)

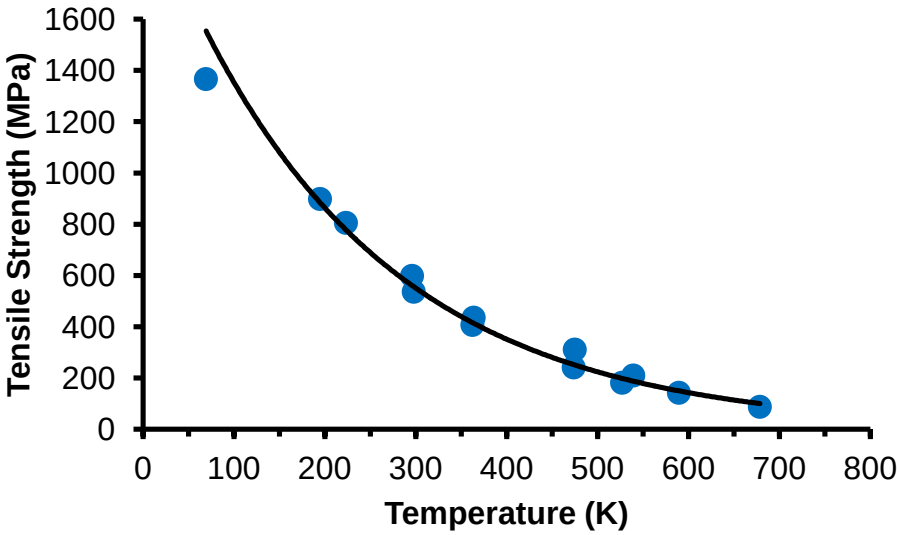

Figure 1.2.1 a) Charpy impact test of W measured at different temperatures. b) Variation of tensile strength of W with temperature [34, 36].

a)

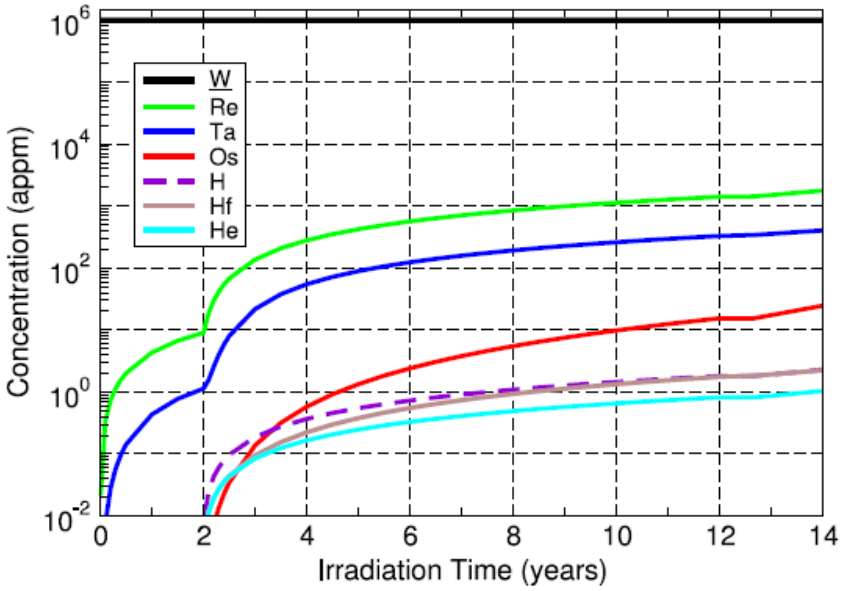

b)

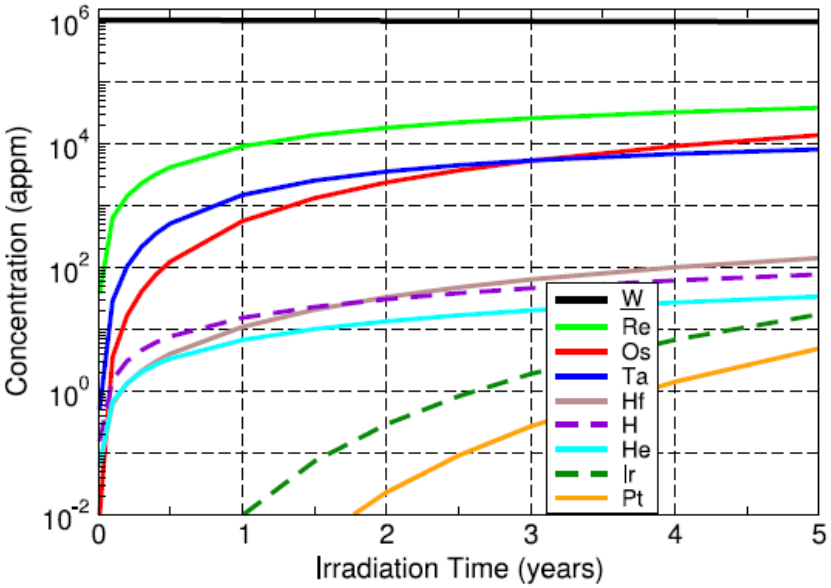

Figure 1.2.2 The transmutation of W into solutes with years of operation inside a (a) ITER fusion reactor (b) DEMO fusion reactors [18, 19].

1.3 Phase Stability of Tungsten Alloys

Binary and ternary phase diagrams involving W, Re, Os or Ta illustrate the phases expected to form under equilibrium non-irradiation conditions. The phase diagrams here are all taken from the ASM series Handbooks of Ternary Alloy Phase Diagrams and are based on experimental studies [37]. Such studies identified phases and solid solutions through fabricating different alloys, heat treating them and analysing the resulting microstructure with optical and electron microscopy techniques [37]. The equilibrium intermediate phases that forms are a good reference point for later sections describing irradiation induced precipitates.

1.3.1 Binary Phase Diagrams

1.3.1.1 W-Re

The experimentally determined W-Re phase diagram is shown in Figure 1.3.1a). The Tungsten BCC and Rhenium HCP single phase at either end of the phase diagram exhibit a good mutual solubility of either element. Re has ~27at.% solubility at 1773K in tungsten beyond which, intermediate Sigma phase (σ) will form followed by Chi phase (χ) at higher Re contents [37]. In comparing the size of σ and χ phase areas, the former appear to encompass the greatest region: 27-72at.% Re (at 1500K), indicating it is a more stable phase. χ phase only forms at temperatures below 2398K.

The low diffusion rates of tungsten and rhenium means phases could not be ascertained below 1773K in Figure 1.3.1a) [38, 39]. A CALPHAD simulated phase diagram for W-Re system is shown in Figure 1.3.1b) and predicts phases expected

down to 500K [40]. According to this phase diagram, χ phase is the only stable intermediate phase below ~850K, but the accuracy of this computer generated phase diagram has yet to be supported by experimental work.

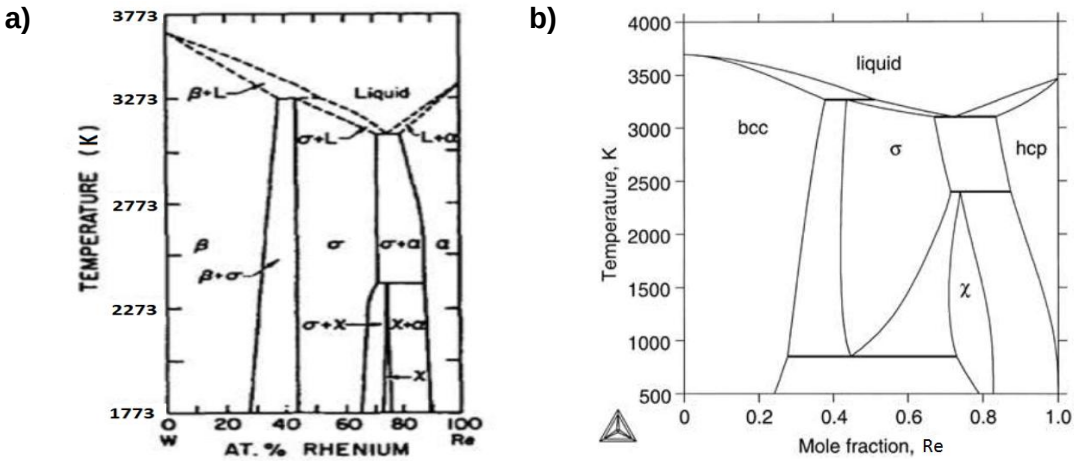

Figure 1.3.1 (a) experimentally determined phase diagram for W-Re system [37, 41, 42]. (b) the computer modelling determined phase diagram [40].

1.3.1.2 W-Os

The W-Os phase diagram is shown in Figure 1.3.2 below, having some similar features to the W-Re phase diagram [37]. Firstly, the phase diagram only predicts phases down to 1523K due to the low diffusivity of Os and W below that temperature. Secondly, Osmium has an HCP structure and is soluble in the Tungsten BCC single phase up to 12at.% Os at 1773K. Finally, the intermediate σ phase encompasses a large region: 12-72at.% Os, although, it is the only intermediate phase found for this system. No computer modelling predictions have been done on this system to date.

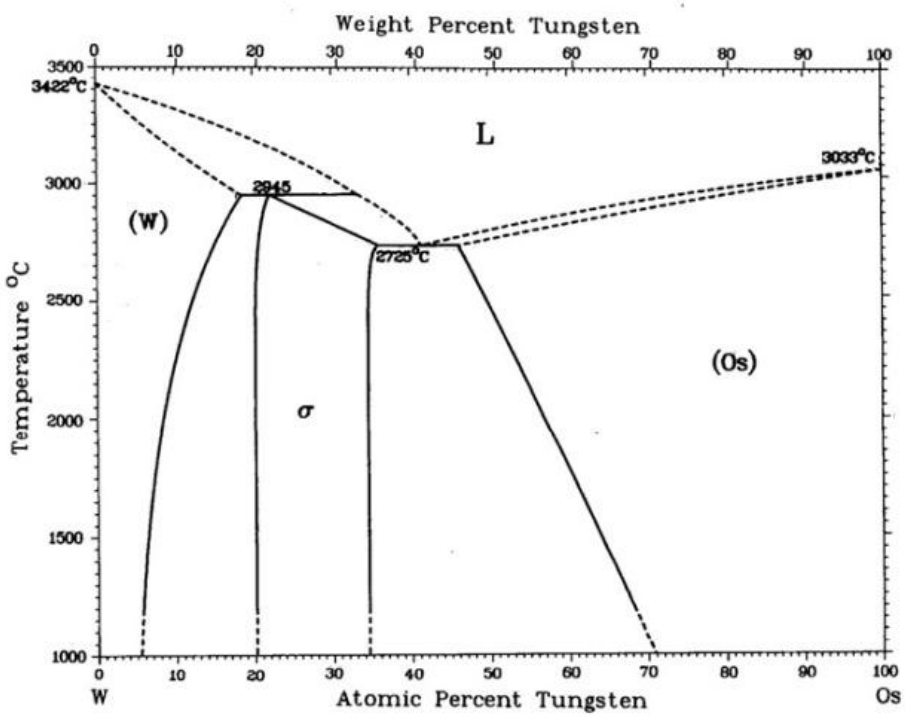

Figure 1.3.2. Experimentally determined binary phase diagram for W-Os system [37].

1.3.1.3 W-Ta

The experimental W-Ta phase diagram in Figure 1.3.3a) shows W and Ta have complete solid solubility with each other, as W and Ta both have a BCC lattice structure and they have the same atomic radii of 137pm [43]. The phase diagram has been experimentally verified only down to a temperature 3173K [37]. Computer modelling predictions of phases below 3173K have identified two stable structures. Figure 1.3.3b) shows there is a dominant B_2 phase with WTa stoichiometry and CuZn structure and a smaller $D0_3$ phase with WTa_3 stoichiometry and Fe_3Al structure [44].

a)

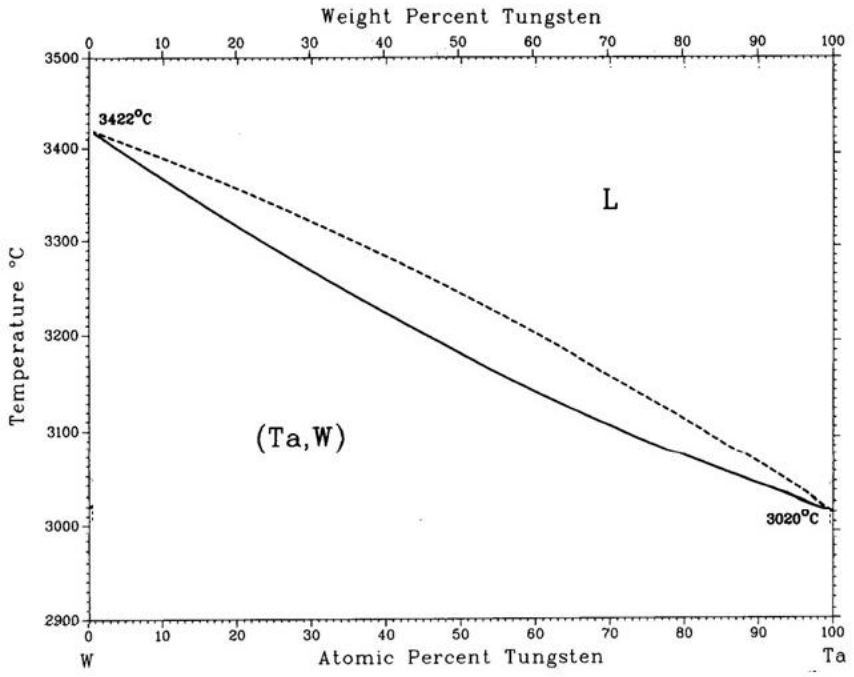

b)

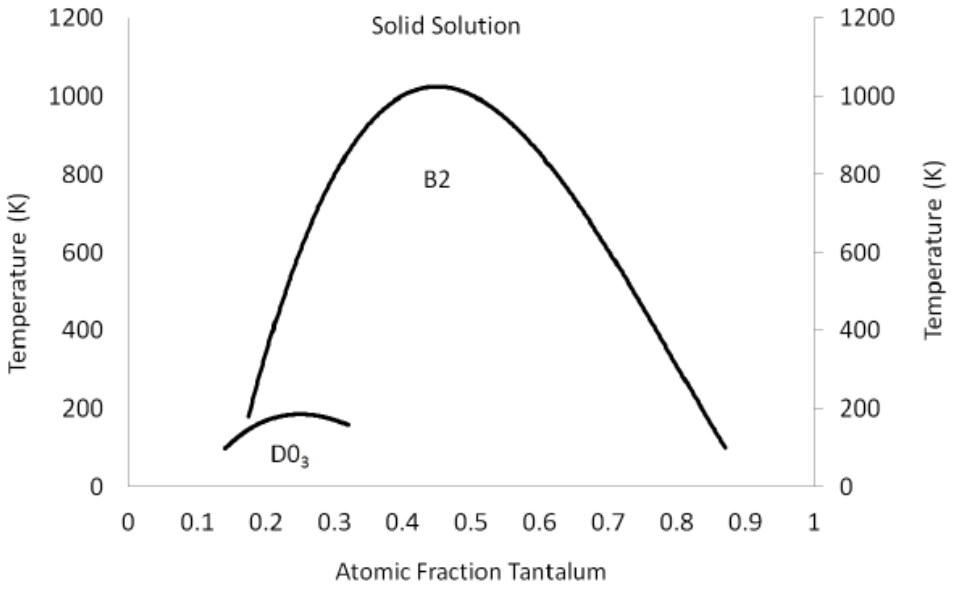

Figure 1.3.3. a) Experimentally determined binary phase diagram for Ta-W system [37].b) Computational predictions of stable phases for W-Ta system below 1200 K [44].

1.3.2 Ternary Phase Diagrams

1.3.2.1 W-Re-Os

A partial ternary phase diagram for the W-Re-Os system is shown in Figure 1.3.4 at the 1873K isotherm [37]. The black regions represent single phases. The smaller black coloured region on the W corner is W BCC solid solution and the larger black area represents σ phase. The white region between the two black regions is composed of a mixture of σ phase and W BCC phase. It is unknown all the phases in the other white region as it has not yet been investigated but, at least σ and Os HCP phase are present [37].

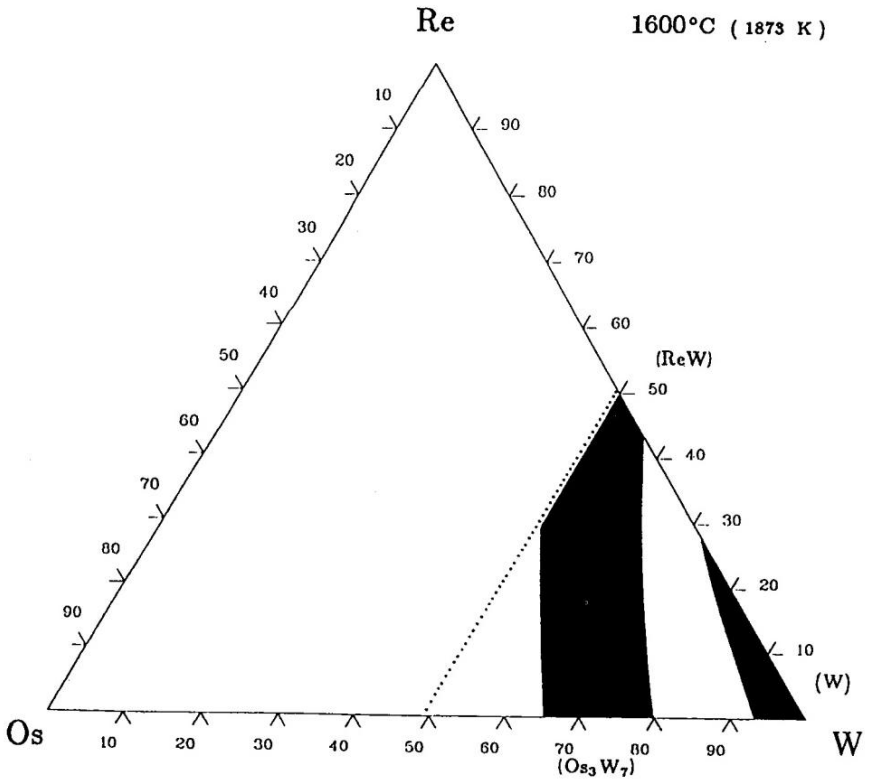

Figure 1.3.4 Partial ternary phase diagram W-Re-Os system as determined experimentally at 1873K isotherm [37].

1.3.2.2 W-Re-Ta

A ternary phase diagram is shown for the W-Re-Ta system in Figure 1.3.5 at the 1473K isotherm [37]. Roughly half of the phase diagram is covered by the BCC solid solubility phase: the black area over the W and Ta corners. The σ and χ phases have similar sized single phase regions [37]. The smallest single phase region appears to be the Re HCP solid solution at the Re corner.

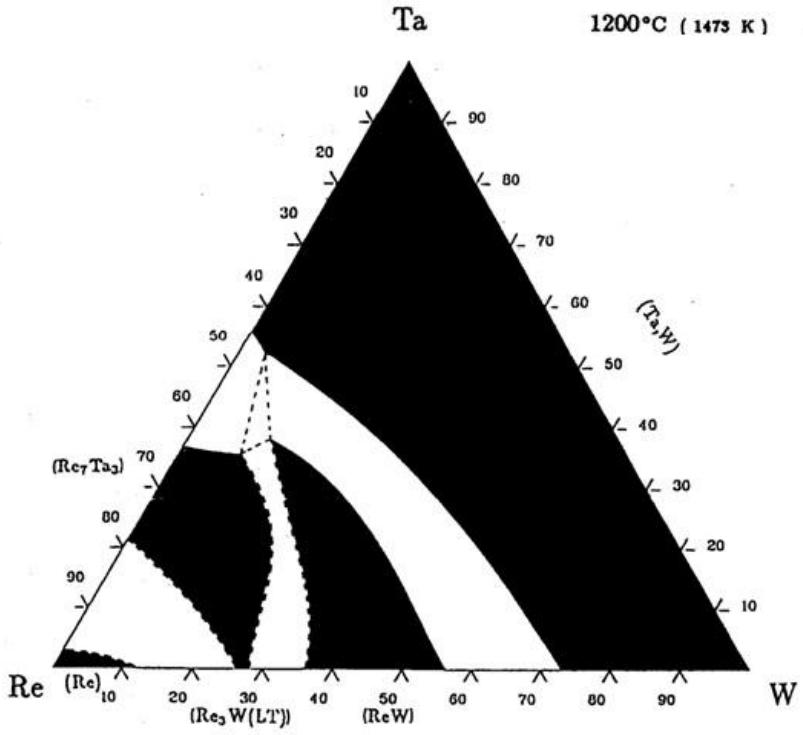

Figure 1.3.5. Ternary phase diagram at 1473K isotherm for the W-Re-Ta system as determined experimentally [37].

1.3.3 Comparison with Transmutation Rates

According tungsten neutron transmutation rates in aforementioned §1.2.4, it is possible to predict the thermodynamic stability of transmuted tungsten alloys under

thermo-equilibrium conditions. For 14 years of ITER operation, the total amount of transmutation species formed doesn't exceed 5at.%. It will largely be a solid solution in accordance with equilibrium phase diagrams. Similarly, this condition is also satisfied for tungsten undergoing 5 years of operation within DEMO. At 14 years of DEMO operation, the Re and Os reaches levels of 11 and 15at.% respectively, making precipitate formation favourable according to the phase diagrams.

1.3.4 Precipitates

Examination of the W-Re, W-Os, W-Ta, W-Re-Os and W-Re-Ta phase diagrams showed only two intermediate phase form among the four atomic species considered here: Sigma (σ) and Chi (χ). The σ phase possesses a FeCr structure ($D8_b$, Pearson symbol tP30, space group $P4_2/mnm$) composed of (Re,Os)/W stoichiometry of 30-50at.% [40, 45]. The χ phase has a α-Mn structure (A12, Pearson symbol cI58, space group I-43m) having a Re/W stoichiometry of 70-80at.% [40, 45]. Shown in Figure 1.3.6, both crystal structures are highly complex, involving a minimum of 20 atoms per unit cell. Other research into these crystal structures found they have no slip planes for dislocation movement [46, 47].

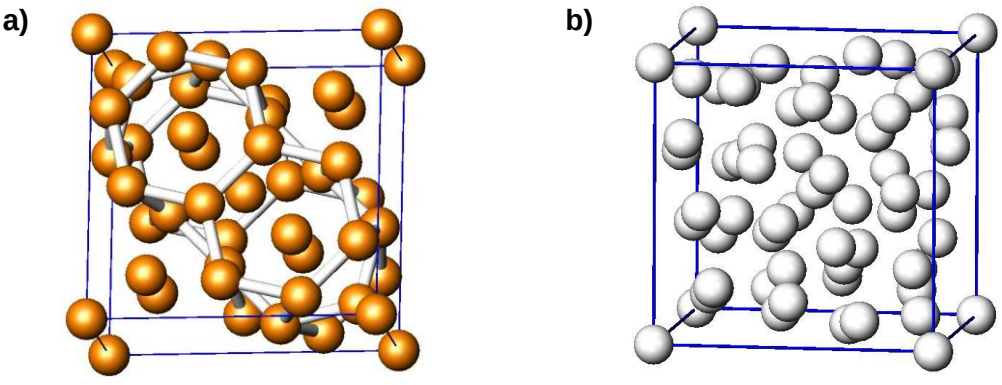

Figure 1.3.6 Atomic positioning for (a) Sigma FeCr crystal structure and (b) Chi α-Mn crystal Structure [45].

1.4 Theory of Radiation Damage in Metals

1.4.3 The Collision Cascade

As a neutron or high energy particle impacts a metal it collides with a lattice atom to create a primary knock-on atom. In a chain reaction, secondary and tertiary knock-on atoms are created producing a damage cascade. The Kinchin-Pease model is an effective way of predicting such damage [48]. It assumes the collisions are elastic and a critical displacement energy E_d is needed to displace the atoms. The model involves certain simplifications, that is, the metal is at 0K, has no lattice structure and all collisions are head-on [49]. A mathematical representation of amount of displacements created for a knock-on atom of energy E_p is shown below.

$$v(E_p) = 0, \qquad E_p < E_d$$

$$v(E_p) = 1, \qquad E_d \leq E_p \leq 2E_d$$

$$v(E_p) = \frac{E_p}{2E_d}, \qquad 2E_d \leq E_p \leq E_c$$

$$v(E_p) = 0, \qquad E_p > E_c$$

In this mathematical model, v is the number of atoms displaced and E_c is the ionization energy. No displacements occur above this energy as the knock-on atom is no-longer charge neutral, but ionic and any collision will be inelastic [48, 50].

Based on the Kinchin-Pease model, Ziegler created software called Stopping Ranges of Ion in Matter (SRIM) [51]. SRIM is tailored to simulate in 3D the damage from knock-on atoms only [51, 52]. Once the simulation is started, SRIM calculates the collision cascade for each atoms that penetrates the metal, accumulating the damage and stopping the simulation at a user specified number of ions [51]. Apart

from creating a visual representation of the damage cascade created, SRIM collects the ion distribution, recoil energy and collision events per penetrating atom (φ) as a function of depth [49]. The collision event data can be converted to give the predicted damage created in displacements per atom (dpa), calculated using the following equation:

$$dpa = \frac{fluence \times \varphi}{N_{at}}$$

Where fluence is the number of ions that bombards a unit area of the material and N_{at} is the number of matrix atoms per unit volume [53].

1.2.4 Channelling, Focusing and Displacement Spikes

The Kinchin-Pease model simplifies some aspects of radiation damage because it ignores the presence of an ordered lattice. Channeling and focusing are long range damage mechanisms illustrated in Figure 1.4.2 below. Channeling occurs where the penetrating atom travels down a direction where interstitial spaces are aligned much like a channel. Whilst it loses energy in glancing collisions, no direct collisions occur and the ion can penetrate to be 2-5 times the SRIM predicted depth [54]. In focusing, a high energy particle collide a lattice atom at a critical angle close to a close packed direction. It becomes captured by the lattice and energy is transferred along this direction and distributed over a long row of atoms [49, 50].

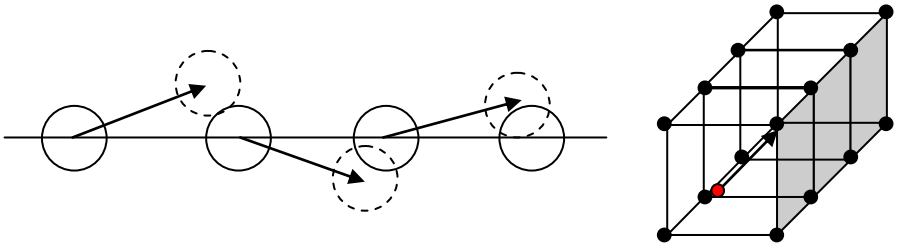

Figure 1.4.2 (left) focusing is the transfer of displacement down a line of atoms. (right) channelling involves travelling down interstitial channels in the metal lattice[49].

Spike phenomena are sudden local increases in either vacancies (displacement), lattice vibrations (temperature) or strain (plasticity) that are created as an energetic particle slows down. These three types of damage last a few nanoseconds in the metal lattice but create a huge number of point defects [49, 50]. A displacement spike is created as a primary knock-on ion comes to rest. The distance between consecutive collisions in the metal falls below the metal inter-atomic spacing, so multiple atoms are displaced within a small volume[49, 50]. A core of vacancies is created, surrounded by a dense shell of interstitial atoms as shown in Figure 1.4.3 [49]. This defect then either remains as a void or collapses to form a dislocation loop [50, 55]. The displacement spike introduces a huge amount of local damage to the material.

In a thermal spike, a lattice atom is imparted with energy that is just below the displacement energy. This atom vibrates at a high frequency which is quickly transferred to nearby atoms [49]. A spherical volume of atoms at the melting point temperature is created. Since the metal lattice confines the thermal spike, approximately a few lattice planes in size is created of a superheated solid which can generate a huge number of vacancies (~500000) [49].

A plasticity spike is a large lattice strain that follows in the aftermath of a displacement or thermal spike. The strain is relieved by the creation and propagation of nearby dislocations and rapidly hardens the material [49]. All three spikes induce a significant amount of damage. SRIM does not account for the latter two: thermal and plastic and thus under predicts degree of radiation damage.

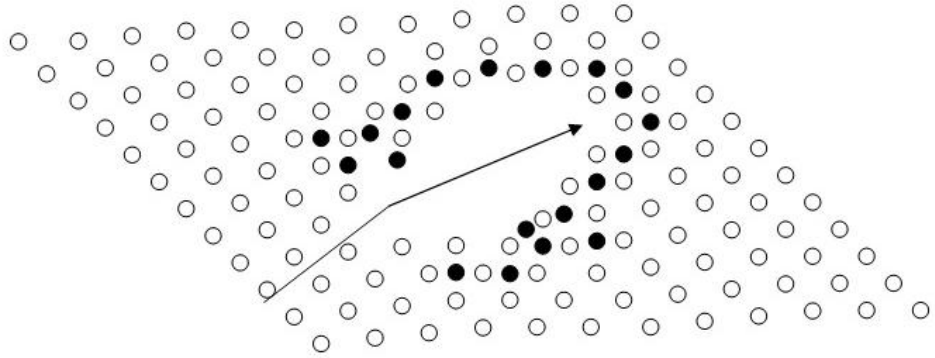

Figure 1.4.3 Schematic of a displacement cascade. Lattice atoms are white and interstitial atoms are coloured black.

1.4.1 Defects in Pure Tungsten

Vacancies and self-interstitials are common point defects within any crystal. A vacancy is an unoccupied lattice site while a self-interstitial is an atom that has occupied a non-lattice site [49, 50]. In most metals, the formation energy (U_f) for a vacancy is lower than the formation energy for an interstitial. In the case of pure tungsten, the vacancy has a formation energy of 3.3-4.9eV [48, 50], threefold smaller than the formation energy of self-interstitials (9.73-11.20eV) [56]. At thermal equilibrium, vacancies will form more easily than self-interstitials making it the major driving force of recovery and recrystallisation within pure tungsten with interstitials having a minimal effect.

However, under irradiation, the concentration of both point defects is exceeded far beyond their expected equilibrium levels [48, 50]. Under such conditions, more complex defects arise. The simplest configuration is a Frenkel defect which consists of a vacancy and a self-interstitial produced when a lattice atom is knocked off its lattice site. The interstitial typically occupies octahedral and tetrahedral sites in the BCC lattice [56]. Because these formation energies are so high, the initial interstitial configuration formed is unstable and will become a crowdion: close packed line of atoms as shown in Figure 1.4.1. Its formation energy is 8.89eV as per DFT modelling by Nguyen et al [57] much lower than the interstitial formation energy. Once the self-interstitial atom forms a crowdion, its energy becomes dispersed along the <111> direction [57, 58].

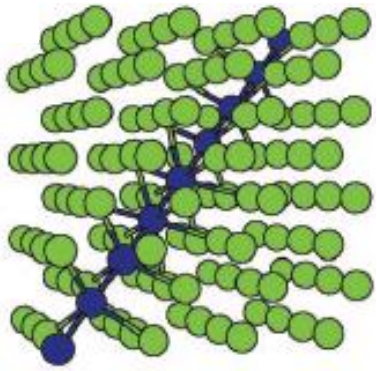

Figure 1.4.1 Schematic of crowdion defect highlighted by the red atoms [49, 57].

Similarly, vacancies can also combine to form more stable configurations. A pair of vacancies can combine to form a divacancy with a binding energy of 1.37eV [48, 50]. More complex vacancy configurations of trivacancy and even vacancy clusters are also energetically favourable than divacancy but they have a higher activation energy for their formation [48, 50].

1.4.2 Radiation damage in Tungsten Alloys

Radiation damage in tungsten alloyed with transmutation species involves many complex interactions with self-interstitials and vacancies. The energetics of these interactions has been investigated by modelling [59]. Kong et al and Becquart et al calculated the energies of Re, Os and Ta solutes in W as different interstitial configurations [60-62]. A metastable configuration for Re and Os interstitials was found to be a dumbbell oriented along the <110> direction while the Ta interstitial tends to form a crowdion along the <111> direction [60]. The W-Re dumbbells have also been ascertained experimentally in FIM studies of irradiated W-Re alloys by Seidman [63-66], Wilson et al [67] and Suvorov et al [68]. Kong et al and Becquart et al also investigated the interaction of solutes with vacancies [60-62]. The binding energy between vacancy and Re or Os is found to be: 0.20 and 0.35eV respectively so it is favourable for vacancy-solute pairs to form. Ta, has a repulsive energy with vacancy: –0.25eV, meaning it is unlikely for Ta to bind with vacancies.

1.5 Irradiation Effects in tungsten: Microstructural Changes

The studies summarised in this section illustrate the trends discovered to date regarding the effect of temperature and dose on tungsten and its alloys. The work has been achieved on a nano to micro level through using Field Ion Microscopy (FIM), Atom Probe Tomography (APT) and Transmission Electron Microscopy (TEM). All alloys referred to here are in at.% units.

1.5.1 Dislocation loops

A review of measurements of dislocation loop size and number density for neutron irradiated tungsten and its alloys didn't show any distinct trends with temperature, dose or solute content. The data points are too few, inconsistent and clouded by the presence of other defect types: voids and precipitates [69]. However, the ion irradiation experiments by Ciupinski et al, Yi et al and Ferroni et al [70-75] induced dislocations exclusively, whose trends can be characterised more clearly.

W was irradiated to fluences of 0 to 3.6dpa (0 to 2.5 x 10^{19}ions/m^2) at temperatures ranging from 573 to 1023K [74]. TEM analysis found dislocation loops that, with increasing dose, coalesce and grow into a dislocation network. Below 0.4-1.2dpa, formation of dislocations loops occur which consists of a mix of interstitial and vacancy type loops. Increased dose and irradiation temperature generally increases the proportion of interstitial loops. This is shown in Figure 1.5.1a) where fraction of interstitial loops measured is plotted against irradiation temperature. At 573K (300C), the fraction of interstitial loops increases by 20% in tungsten between 0.4

and 1.2dpa. For 1.2dpa, 773K (500C) in tungsten, almost all the loops measured are interstitial type, compared to 75% for 1.2dpa, 573K for tungsten.

Beyond 1.2dpa, a general saturation of dislocation density takes place and the dislocation loops coalesce and evolve into dislocation strings instead. This critical dose is consistent across the temperature range 573-773K. Figure 1.5.1b) shows the number density measured plotted against different irradiation temperatures. At 773K, there is minimal change in dislocation loop density between 0.4, 1.2 and 3.6dpa. All the dislocations formed across all the doses and temperatures in tungsten are either b=1/2<111> or b=<100> nature with a majority being the former [70, 73].

W-5Re and W-5Ta alloys were also investigated under the same irradiation conditions. Analysis showed an overall suppressed dislocation size and number density in W-5Re alloy compared to tungsten. In Figure 1.5.2a), the loop size frequency distribution is plotted for W, W-5Re and W-5Ta irradiated to 0.4dpa, 573K (300C) for 1-10nm size range. The W-5Re alloy has 15% higher frequency of 0-1nm sized loops than pure tungsten. It is further evidenced in Figure 1.5.2b), the amount of loops with sizes >4nm in the W-5Re alloy is consistently smaller than tungsten for 0.4-1.2dpa and 573-773K. The dislocation size measured in the W-5Ta alloy show no deviations from tungsten. In both Figure 1.5.2a) and b), the loop sizes for W and W-5Ta are similar and their error bars overlap each other. It indicates Ta does not suppress loop size like Re does [74].

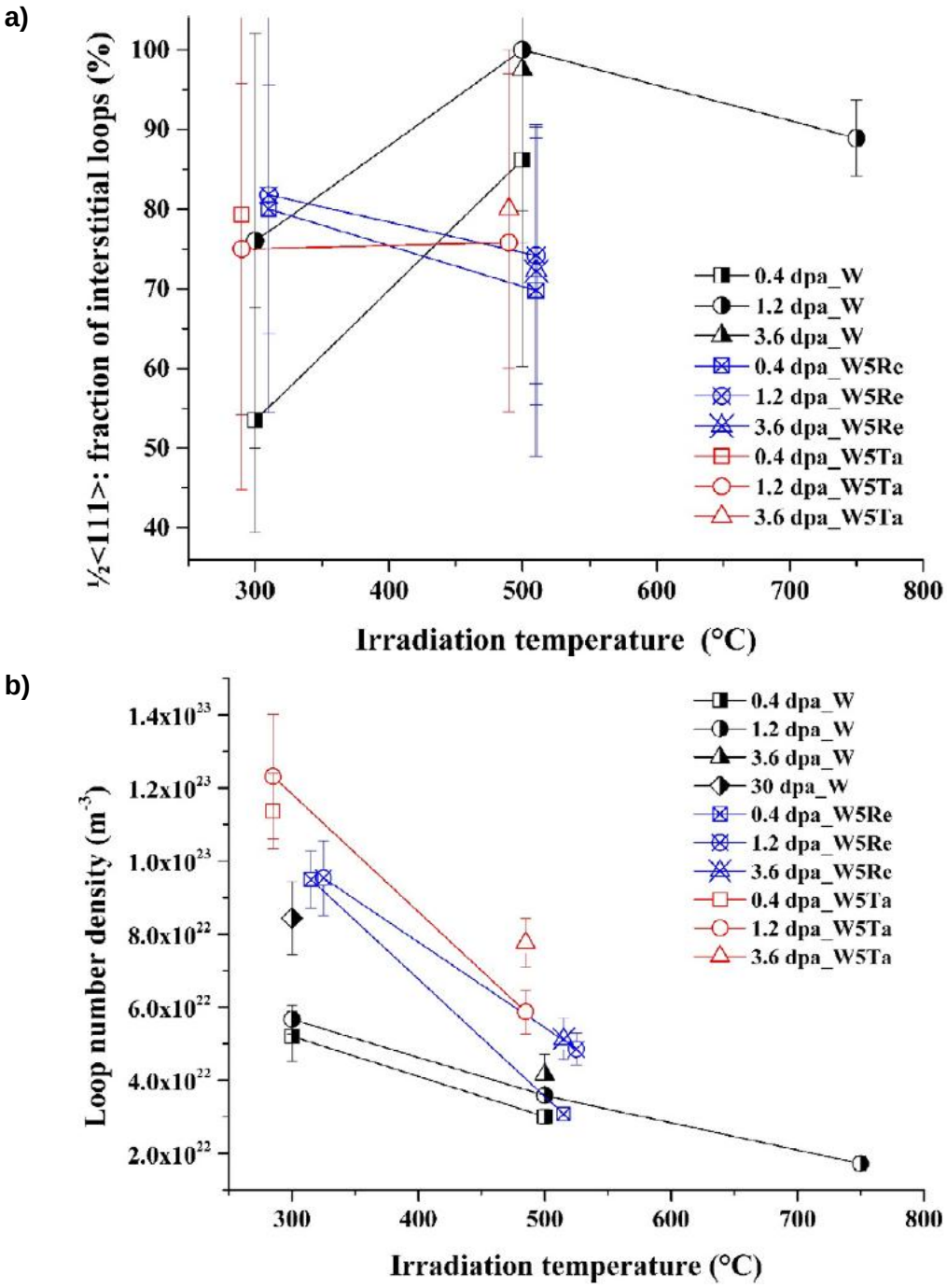

Figure 1.5.1 (a) Fraction of ½<111> loops having an interstitial nature plotted against irradiation temperature for W, W-5Re and W-5Ta. The remaining ½<111> loops are of a vacancy type. (b) Measured dislocation loop number density plotted against irradiation temperature for W, W-5Re and W-5Ta [70, 73].

a)

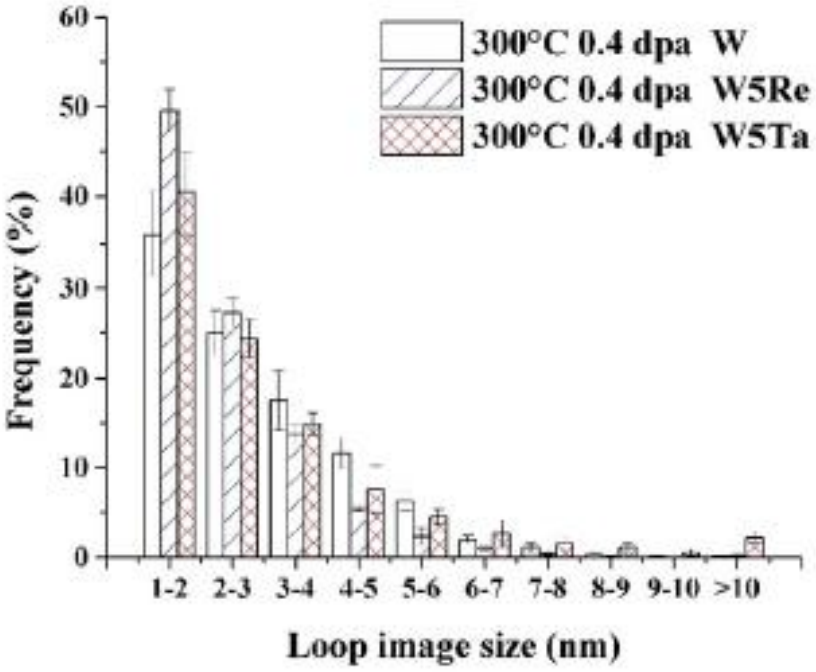

b)

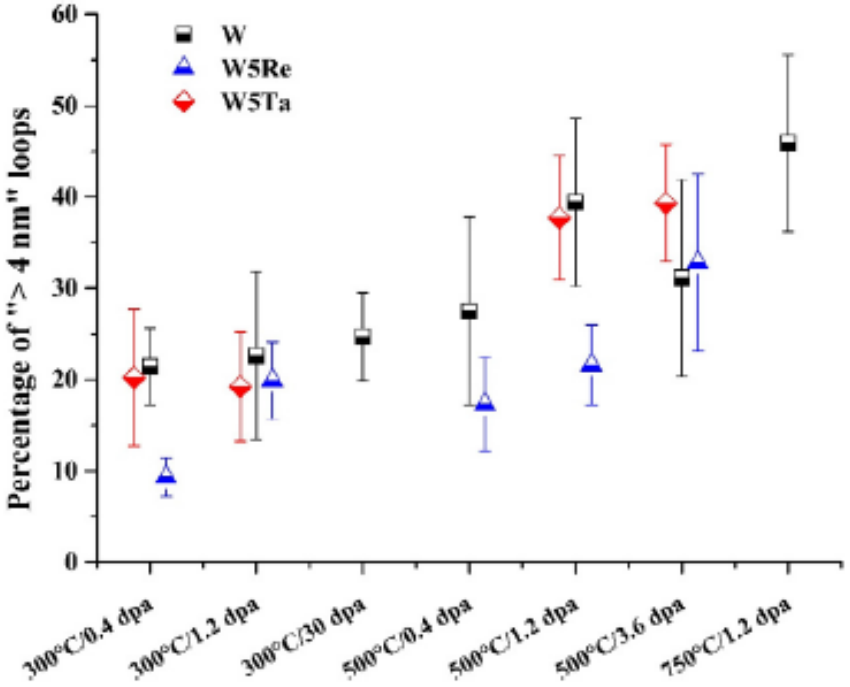

Figure 1.5.2 (a) Irradiation induced dislocation loop size distribution for W, W-5Re and W-5Ta at 0.4dpa 573K (300C). (b) The average of loops with diameters greater than 4nm, plotted for the same aforementioned alloys at various irradiation conditions [70, 73].

1.5.2 Void Formation

The effect of increasing the irradiation temperature and dose on void formation has been investigated by Tanno et al, Rau et al and He et al [46, 69, 76-80]. Table 1.5.1 summarises the void diameter and number density for pure tungsten neutron irradiated at variety of conditions. In the first two columns the dose is constant at 0.15dpa allowing the temperature effect to be derived. So between 873 and 1073K, a higher irradiation temperature increased void size and reduced the cluster number density.

	0.15dpa 873K	0.15dpa 1073K	0.40dpa 1013K	1.54dpa 1023K
Mean Diameter (nm)	1.3	1.9	2.9	4.7
Density (x $10^{22}/m^3$)	6.4	4.2	13	12

Table 1.5.1 Table of Void diameter, density and volume fraction measured for pure tungsten under four different irradiation conditions [46, 80].

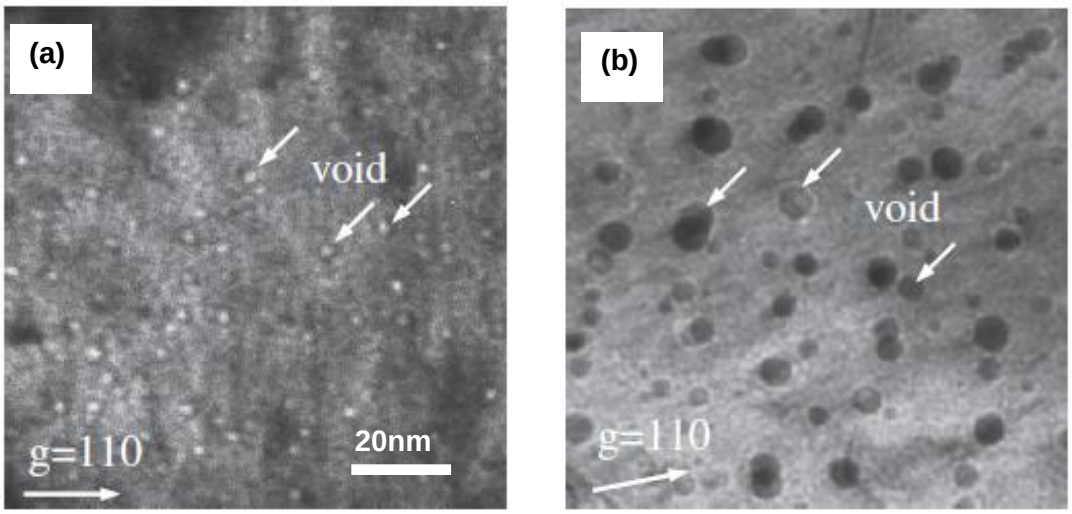

Figure 1.5.3 Neutron irradiated tungsten, TEM analysis, (a) 0.40dpa 1013K and (b) 1.54dpa 1023K. The voids in (b) are black because they were taken in "over focus" condition [80].

The effect of dose on void formation in tungsten can be derived for the last two columns of Table 1.5.1 where the irradiation temperatures are similar: 1013 and 1023K. Between 0.40 and 1.54dpa, the void diameter doubles from 2.9 to 4.7nm with a slight decrease in its number density. At 1.54dpa 1023K, the voids have been even saturated forming a lattice type arrangement shown in TEM micrographs in Figure 1.5.3a-b) [46, 80].

Atomic scale images of voids have been achieved by Sato et al and Seidman et al [81-83], who performed FIM analysis of ion (Ni^+ or W^+) irradiated tungsten needles. The irradiation occurred in situ on a ~50-100nm diameter needle at 10-18K. The voids were imaged in 3D via reconstruction of FIM data. They were found to be vacancy clusters having a diameter range of 3-10nm which overlapped the void diameters measured via TEM in Table 1.5.1.

The presence of Re and Os transmutation species has a capacity to suppress the formation of voids. Tanno et al [46, 76, 80] compared the void lattices present in pure tungsten neutron irradiated to 0.96dpa at 811K and 1.54dpa at 1023K against W-10Re alloy irradiated under the same conditions. At 0.96dpa 811K, no voids were observed at all for W-10Re alloy. For 1.54dpa 1023K condition, the void diameter and number density in W-10Re dropped fourfold compared to pure tungsten [46]. Further, Os has a stronger void suppression effect compared to Re. W-3Os and W-5Re-3Os alloys irradiated to 1.54dpa, 1023K showed no voids at all [46, 76, 80] whilst the W-10Re alloy still features voids. No studies have been done to date on the effect of Ta on void formation in irradiated W.

1.5.3 Cluster Formation

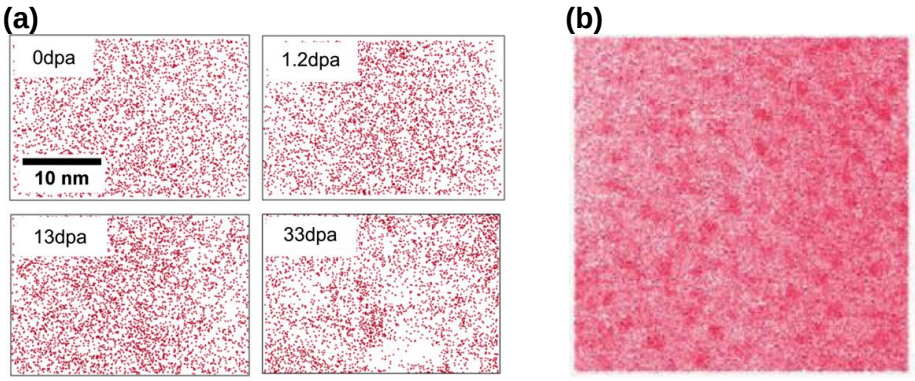

Figure 1.5.4 Atom probe analysis of self-ion irradiated (a) W-5Re alloy from 0 to 33dpa, 573K and (b) W-25Re alloy at fluence 1.2dpa, 773K [11, 12].

Cluster formation is a precursor to irradiation induced precipitate formation [84, 85]. Unfortunately, Re and Os both have the same electron scattering factor as tungsten so bright/dark field TEM analysis cannot reveal their presence [86]. Atom probe analysis has been able to identify Re clusters in W-5Re alloys W-ion irradiated at 0-33dpa ($2.5x10^{19}$ions/m^2) at 573 K (Figure 1.5.4a) [11]. Re clusters evolved from faint to strong segregations under increasing dose. In another experiment, W-25Re alloys irradiated to 1.2dpa ($1.1x10^{18}$ions/m^2) at 773 K also contained clusters (Figure 1.5.4b) [12]. They are 2 – 3 nm in diameter and strongly segregated. The cluster analysis reported thus far on W-Re alloys is mostly qualitative. No cluster analyses of irradiated W-Os and W-Ta alloys have been done to date.

1.5.4 Irradiation Induced Precipitation

TEM analysis of neutron irradiated W-xRe (x: 5 and 10 at.%) alloys at 0.96dpa, 811K and 1.54dpa 1023K identified the presence of precipitates even though phase diagram predicts complete solubility for such compositions [29, 46, 80]. The

presence of these precipitates is shown in Figure 1.5.5a-d); TEM micrographs of the aforementioned irradiated alloys. Some precipitates have a needle shape having a [110] orientation [80]. They were identified via X-ray diffraction to be χ phases. Spherical precipitates are also present which are speculated to be σ phase. Neither X-ray diffraction nor chemical data have verified this.

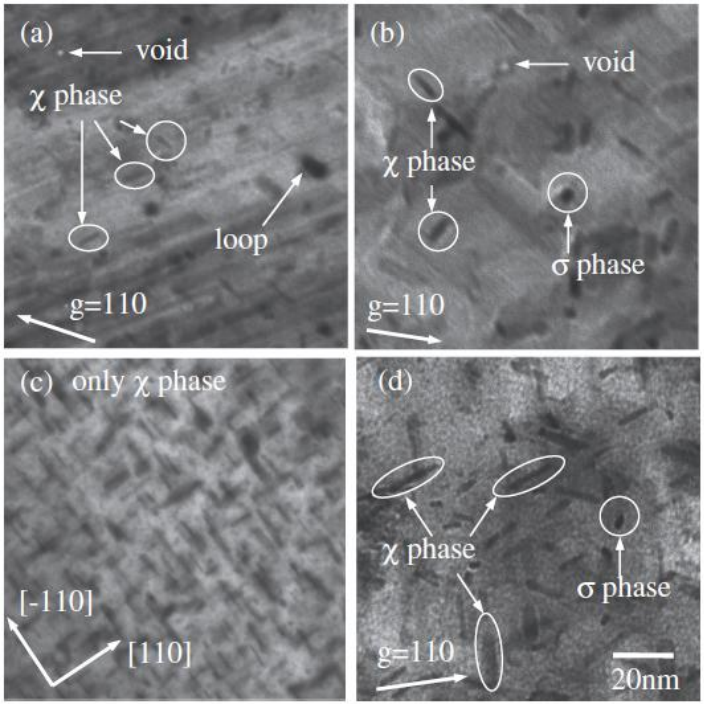

Figure 1.5.5 Neutron irradiated (a) W-5Re 0.96dpa 811K, (b) W-5Re 1.54dpa 1013K, (c) W-10Re 0.96dpa 811K and (d) W-10at.%Re 1.54dpa 1013K. Neutron induced precipitates, loops and voids are labelled in the figure [80].

Table 1.5.2 summarises the length and number density for χ phase precipitates in W-5Re, W-10Re, W-3Os and W-5Re-3Os alloys irradiated to 1.54 dpa 1023 K. Comparing between W-5Re and W-10Re alloy, the higher Re content increases precipitate volume fraction by twofold and the number density by an order of magnitude. However, the measured precipitate length drops from 14 to 9.5 nm. Where Os is present, the precipitate development is altered. In the W-3Os alloy, the

precipitate number density is an order of magnitude smaller than the W-5Re alloy even though the former contains a lesser amount of solutes. In the W-5Re-3Os alloy, Os appears to dominate the precipitation behaviour. The volume fraction approaches that of the W-10Re alloy and the precipitate number density in the ternary exceeds the W-10Re alloy.

	W-5Re	W-10Re	W-3Os	W-5Re-3Os
Mean Length (nm)	14	9.5	7.3	6.8
Density ($x10^{22}/m^3$)	7.3	42	22	67
Volume Fraction (%)	1.5	3.6	0.8	3.4

Table 1.5.2 Needle shaped, χ phase precipitates within W-5Re, W-10Re, W-3Os and W-5Re-3Os all irradiated to 1.54 dpa at 1023 K. The precipitate length, density and volume fraction are tabulated here [46].

Precipitates in irradiated W-Re alloys have been imaged on an atomic scale using FIM/APT analysis by Herschitz and Seidman [63, 64, 87]. Platelets were identified in W-10Re and W-25Re alloys neutron irradiated to 8.6dpa ($4.0x10^{26}$neutron/m^2) at 848-948K. The compositions measured for the platelets appear to correlate with sigma and chi precipitates: 50 and 70 at.% respectively. Additionally, the precipitates are found to be 1-3 atomic layers thick and 4.0 – 5.7 nm in diameter [63, 64]. Also it was noted precipitates nucleate homogeneously rather than nucleating heterogeneously from dislocations or voids.

1.6 Irradiation Effects: Mechanical Properties

The presence of high dislocation density, voids, clusters and precipitates after exposure to radiation hardens and embrittles plasma facing components. Given the small sample size and/or limited radiation penetration regarding neutron or self-ion irradiation experiments, special techniques tailored for characterising the mechanical properties on small-scale specimens are described here [88-93]. The irradiation hardening data regarding tungsten and its alloys under different irradiation conditions are also discussed.

1.6.1 General Preparation Techniques and Effects

Special techniques to manufacture micron sized samples have been developed to measure strength, toughness and hardness on a micro scale. Focused Ion Beam (FIB) microscope is used to sculpt, using an eroding stream of Ga^{+} ions, dog-bone, pillar or cantilever shapes on the material surface [88-93]. The tensile and compressive strength and fracture toughness is engaged through the use of micron-sized clamps and nanoindenters. The details of which can be found in [88-93].

Neutron irradiation hardening can be measured with a Vickers Hardness test where indentations are typically hundreds of microns to millimetres in depth. However, self-ion implantations typically produce a variation of dose over a nanometric to micron sized depth. The hardness of such thin layers can be measured with a Nanoindenter. Using Continuous Stiffness Method (CSM), an Berkovitch tip oscillates as it indents the material surface to give hardness and Young's Modulus as a function of depth [94, 95].

1.6.2 Irradiation Effects on Mechanical Properties of pure W

Armstrong et al analysed the effect of irradiation induced loop formation on mechanical properties [11, 96]. In the experiment, pure tungsten was self-ion irradiated to dose of 0-33dpa (fluence: $2.5x10^{19}$ions/m^2) at 573K. The irradiation hardening was measured at various doses within this damage range and plotted in Figure 1.6.1. The hardening is divided into two stages with the first being a linear increase between 0-0.4dpa and followed by a plateau stage where irradiation hardening only increases slightly. The transition point between the two stages corresponds with point of dislocation saturation as characterised in TEM micrographs by Yi et al [74, 75]. The radiation damage is typically characterised micro-structurally as amount of dislocation loops formed and Yi et al measured minimal increase in dislocation loop density from 0.4dpa onwards.

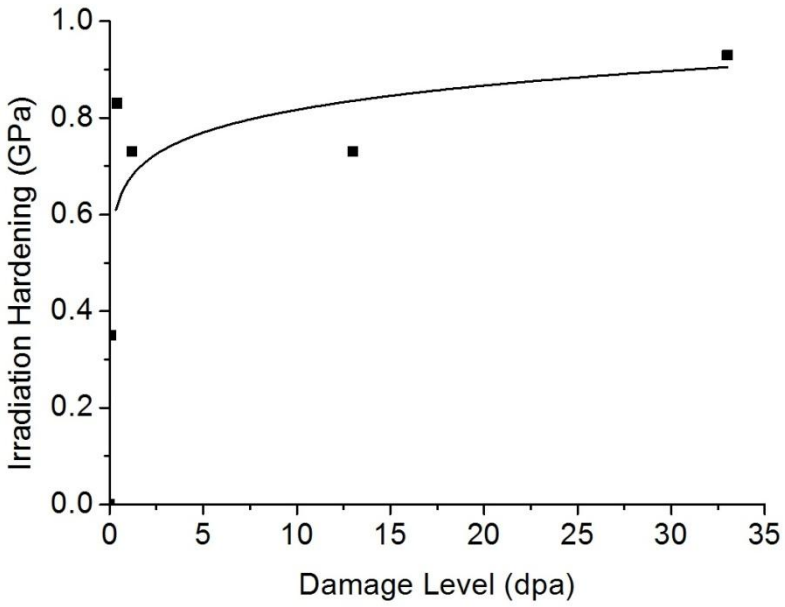

Figure 1.6.1 Pure tungsten self-ion irradiated to 33dpa at 573K. The radiation damage in dpa is plotted against the measured irradiation hardening [11, 96].

Neutron irradiation of tungsten at 0.15dpa at 873K brings about formation of voids in conjunction with dislocation loops [46]. Under this irradiation condition, the irradiation hardening is 2.19GPa, more than twofold higher than the dislocation saturation hardening for self-ion irradiated tungsten (33dpa 573K) in Figure 1.6.1 [69]. At even higher neutron doses and irradiation temperature: 1.54dpa and 1023K, the irradiation hardening experienced reaches 3.70GPa, which is four times the aforementioned dislocation saturation hardening in self-ion irradiated tungsten.

Rau et al and Steichen et al showed that tungsten is embrittled by neutron radiation damage [97-99]. Tensile testing at 673K of tungsten samples neutron to $4.0x10^{19}$neutrons/m^2 measured an elongation of 0.3% compared to 45.6 % in the unirradiated state. The same studies also showed a two fold increase in tensile strength for tungsten exposed to fluence 9×10^{25}neutrons/m^2.

1.6.3 Mechanical Properties of W Alloys

W-Re alloys have been most extensively studied because Re has many beneficial effects on tungsten in unirradiated state. It decreases DBTT and increases strength and toughness both of which has been linked to the ability of Re to reduce dislocation stacking fault energy and to segregate to grain boundaries [34, 100-103]. It is most evident for W-25Re alloy. At room temperature, its elongation is 4% while pure tungsten has no elongation. Also the tensile strength of W-25Re at room temperature is 729MPa [34] compared to 172 MPa for pure tungsten.

The only data on mechanical properties of W-Os alloys show that Os has a strong solid solution hardening effect. A 5at.% Os presence increases the materials hardness threefold compared to pure tungsten [76, 78]. There isn't much research

on tungsten tantalum alloys. Cantilever indentation of a W-5Ta alloy indicated its DBTT is well above 1173K twice as high as pure tungsten. Between room temperature and 1173K, the cantilever consistently fails in a brittle intergrannular manner, measuring a low fracture toughness of ~5 - 20 MPa.$m^{1/2}$ [104-106]. There are no data available on the mechanical properties of W-Re-Os and W-Re-Ta alloys.

1.5.3 Ion Irradiation Effects on Mechanical Properties of W Alloys

Ion irradiation of W-5Re and W-5Ta alloys have been investigated by Armstrong et al at 0-33dpa and 773 K [11, 107]. The irradiation hardening measured at various damage levels are plotted in Figure 1.5.2 for pure tungsten, W-5Re and W-5Ta alloys. It is immediately evident Re and Ta have very different hardening behaviours. The W-Re alloy exhibited a sharp rise in hardness between 0 – 1.2 dpa, which was attributed to dislocation formation. Beyond 1.2 dpa, the irradiation hardening still rises but at a shallower slope, unlike pure tungsten which has a plateau. Atom probe analysis attributed the absence of a plateau to the presence of Re clusters whose degree of segregation became stronger with dose. More detailed data is unavailable as the atom probe analysis was conducted on a qualitative level.

On the other hand, the W-5Ta alloy hardens to a greater extent between 0 – 1.2 dpa as the hardening value at 1.2 dpa is 150% greater than the corresponding hardening value for the W-5Re alloy. For doses greater than 1.2 dpa, the hardening values plateau instead, much like that for pure tungsten. Between 1.2 and 33dpa the hardening increase is less than 0.5 GPa for W-Ta alloy, whereas the hardening for the W-5Re alloy rose by almost 3GPa. There was no reliable APT or TEM analysis associated with W-Ta alloy so it is unknown whether clusters are present or not.

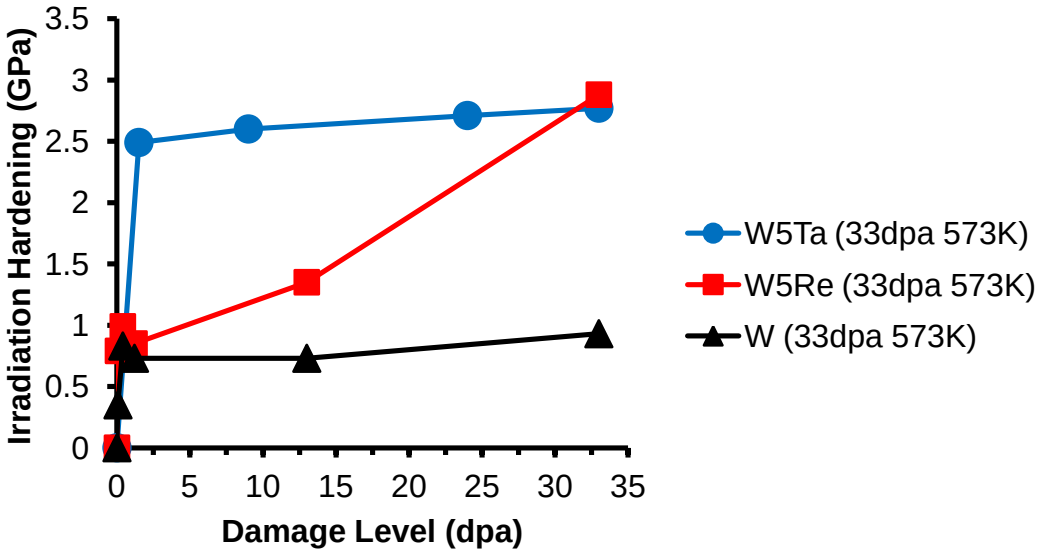

Figure 1.6.2 W, W-5Re and W-5Ta alloy irradiated at doses from 0 to 33dpa at 573K. Plot of irradiation hardening measured against damage level [11, 107, 108].

For neutron irradiated W-Re alloys studied in the temperature range 811 – 1073 K, there appears to be a critical dose below which precipitation doesn't occur and radiation damage is suppressed by Re presence [69, 77, 78]. This critical dose is at ~0.4 dpa and is illustrated Figure 1.6.3 which plots irradiation hardening against Re content. There are six irradiation conditions plotted which are divided into three groups of two, with each group having similar doses assigned the same colour. The black coloured lines represent 0.15 dpa at 873 and 1073K irradiation condition. The hardenings of all W-Re alloys are consistently at 0.7-0.8GPa more than twofolds smaller than the hardening of pure W. The smaller irradiation hardening in W-WRe alloys is due to the suppressing effect of Re on void and dislocation formation mentioned earlier in §1.4.1-1.4.2. As the dose increase to 0.37-0.40dpa for 873 and 1073K, the hardening difference between W and W-Re alloys is narrowed to deviate by at most ~1GPa from hardening of pure tungsten. Above this dose at 0.96 and 1.54dpa (same temperature range), the hardening in the W-Re alloys becomes

significantly larger. The hardening is linear with bulk Re content with the highest value being 9.31GPa for W-25Re at 0.96 dpa, 811 K as compared to 3.60GPa for W. The strong hardening is attributed to the presence of precipitates which has been postulated to have an embrittling effect. But there is no direct evidence of this.

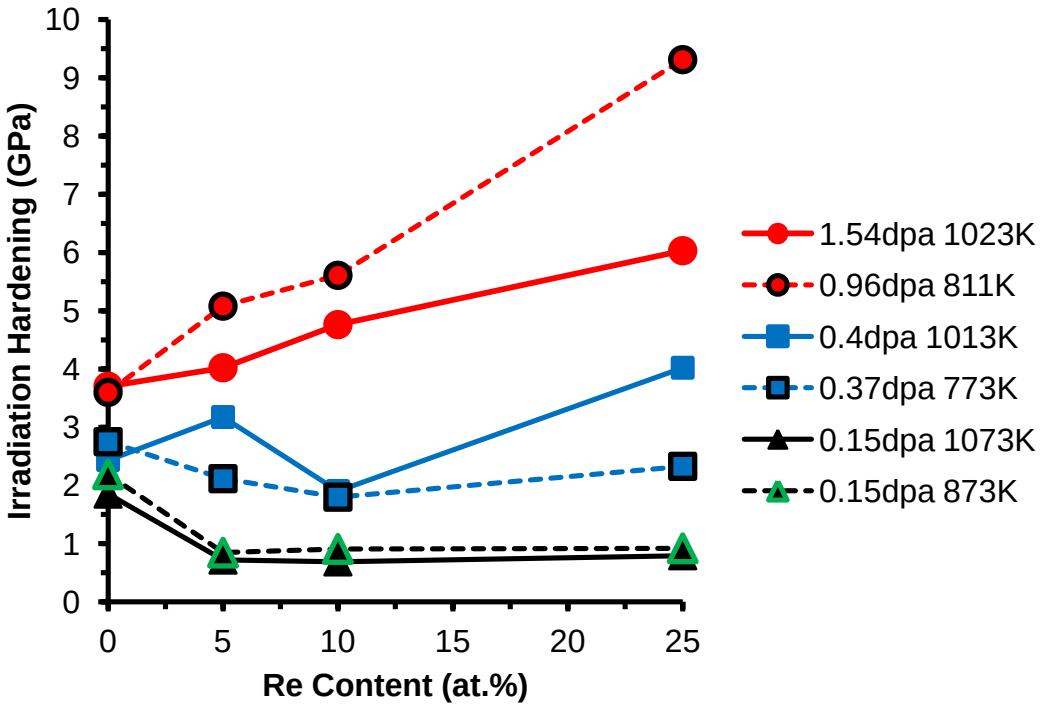

Figure 1.6.3 Irradiation hardening (Irradiatied hardness minus unirradiated hardness) plotted against Re content for various neutron irradiation conditions [69, 77, 78].

Irradiation of W-Os and W-Re-Os alloys does not show the initial damage resistance phase observed for the W-Re alloys; they harden rapidly and to large values [46, 77]. This is illustrated in Figure 1.6.4 which plots irradiation hardening of W-3Os and W-5Os alloys under four different irradiation conditions. For W-3Os alloy irradiated to 0.17dpa and 673K, the irradiation hardening is 6.56GPa, three times higher than that of W and six times higher than that of W-Re alloy. At 1.5dpa 1023K, the irradiation hardening reaches even higher values of 7.94GPa.

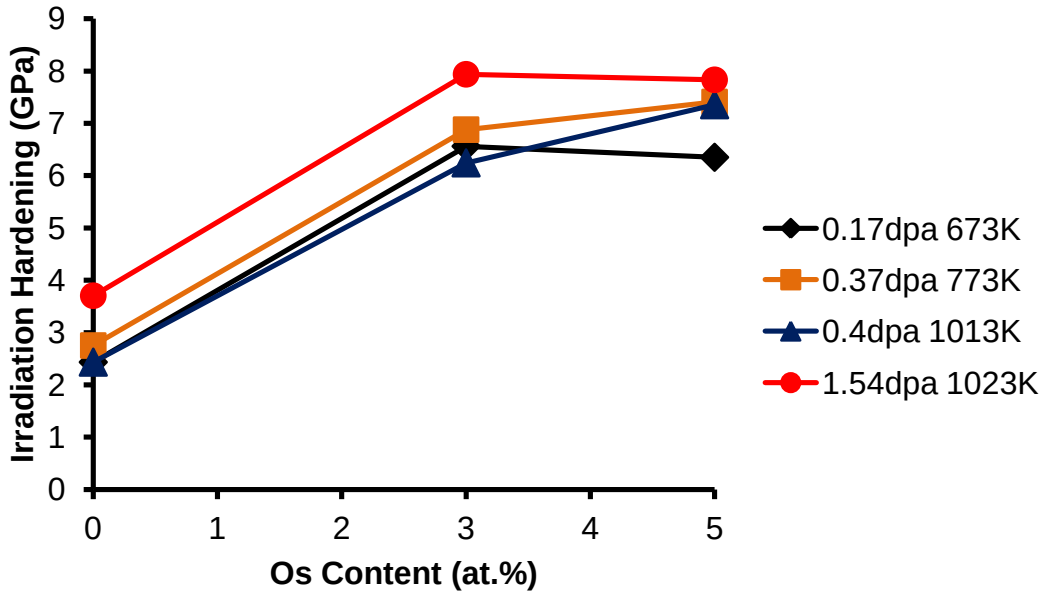

Figure 1.6.4 Irradiation hardening (Irradiatied hardness minus unirradiated hardness) plotted against Os content for various neutron irradiation conditions [69, 77, 78].

1.7 Summary

The choice of tungsten as fusion PFC material is one of few instances where tungsten is applied for structural application or radiation environments. As a result, studies available on tungsten and its alloys in an unirradiated and irradiated state are quite limited. Nonetheless, this literature survey was able to highlight many key data and trends.

- Tungsten has exceptional physical properties such as high melting point, high thermal conductivity and low diffusivity suitable for PFC. Its corrosion and oxidation resistance can be good provided the temperature is low and no oxygen is present. Tungsten is very stiff and hard though its high DBTT makes it very brittle at room temperature.
- Computer models predict the W-Re-Os-Ta transmutation alloy expected after years of operation in ITER and DEMO. For the solute contents after 5 years of operation in either reactor, the phase diagram predicts complete solubility under thermo-equilibrium conditions. It is only at much higher solute contents > 30at.% (Re, Os, Ta) that brittle sigma and chi phases form.
- The Kinchin-Pease model is the most widely used to predict displacements cascades caused by radiation damage. However, it oversimplifies interaction of solutes with defects, lattice effects and displacement spikes.
- Voids, dislocations, clusters and precipitates form in irradiated tungsten and tungsten alloys. Their size and number density increases with dose and temperature and is matched by increased hardening of the tungsten alloys. Higher nominal Re content increases the cluster number density further and the same effect is seen where Os is present.

1.8 Purpose of Thesis

Having reviewed the literature, the analysis conducted on irradiation induced precipitates to date is predominantly on a macro level, being very inconsistent in irradiation conditions as well as lacking in extensive physical and chemical data. Whilst it lay a good foundation for a rather unexplored area there are many questions yet to be addressed. Thus, further research is needed to better understand the early stages of precipitate formation: clustering and the effect of Os and Ta solutes on clustering which are also forming in significant quantities in DEMO reactor operation. Also the roles of interstitials and vacancies on cluster formation have yet to be explored, along with the effect of material structure and alloy content. This work reported here is focused on such topics to broaden our understanding. We aim to use mostly nano-scale techniques APT, TEM and Nanoindentation to achieve a physical, chemical and mechanical analysis of the clusters/precipitates in question.

2. Experimental Methodology

2.1 Materials, Experimental Conditions and Equipment

2.1.1 Materials

2.1.1.1 Reason Behind Alloy Choices

Manufacturer: Sample Diameter: Sample Type: Impurity Content: Grain Size	Oxford (lab-made) ~10mm Plate <500 1-3mm	Goodfellows (commercial) ~0.25-1.00mm Wire <220ppm 0.5-1µm	Plansee (commercial) ~10mm Plate <300ppm 4-10µm	Ames Lab (lab-made) ~10mm Plate <500 1-3mm
W	X	X	X	
W-2Re	X			
W-3Re		X		
W-5Re	X	X	X	
W-10Re	X			
W-25Re	X	X		
W-5Ta	X			
W-1Re-1Os				X
W-2Re-1Ta	X			

Table 2.1.1 Matrix of materials used in this thesis

In Table 2.1.1, a total of 8 materials are listed; pure tungsten metal, 5 W-Re alloys, 1 W-Ta alloy and 2 ternary alloys. The tungsten was chosen to serve as a reference point for irradiation behaviour in the absence of clustering while the other alloys simulate compositions anticipated as a result of neutron transmutation. The W-Re alloys compositions can be divided into two groups. The 2, 3 and 5 at.% Re alloys represent Re compositions after 3 – 5 years of DEMO operation, while the 10 at.% Re stands for 10 years of operation [18, 19]. The 25 at.% Re is not expected in DEMO, but is an extreme scenario included to examine possible limits of behaviour; it just falls within the W-Re solubility limit (27 at.%) [109]. The W-5Ta alloy is not composition expected in DEMO but, it is useful for determining whether Ta clusters

under irradiation. Further, secondary and tertiary elements; Os and Ta form alongside Re as tungsten undergoes neutron exposure in DEMO [18, 19]. The ternary compositions: W-1Re-1Os and W-2Re-1Ta approach compositions expected after 3-5 years [18, 19]. With W-2Re alloy as a control sample, the ternary alloys illustrate effect of Os and Ta on cluster behaviour.

The compositions of all samples in Table 2.1.1 were verified with a combination of Atom Probe, EPMA and XRF techniques. The measured compositions varied by no more than 0.5at.% from the expected composition. As well, the measured impurity level is at a consistent level across all the samples being in the range of 200-300ppm.

2.1.1.2 Commercially Procured Materials

Table 2.1.1 features two commercial sources: Goodfellows and Plansee ltd, which have only W-Re alloys available. They were procured in wire and plate forms for tungsten, W-3Re, W-5Re and W-25Re alloys. The Goodfellow ltd wire samples are 0.25-1mm in diameter. Being heavily drawn, they have elongated grains with <110> texture along the wire direction as shown in Figure 2.1.1a). The grain sizes of these wire samples had been previously measured by Humphry-Baker [53]. A wire sample was polished along its length and the grain size was measured cross-sectionally, perpendicular to length direction via optical microscopy imaging. Table 2.1.1 reports the grain diameter to be 0.5-1 [12, 30, 53]. Plate samples from Plansee pty ltd are 1mm thick and 10 by 10mm in area. The cold rolling process had given them pancake shaped grains shown in Figure 2.1.1b) and <100> orientation normal to sample surface [11, 30, 96]. Armstrong et al measured the grain diameter of these

samples via optical microscopy to be 4-10μm (Table 2.1.1) [11].The differences in grain size and shape for plate and wire samples can be used to evaluate the effectiveness of grain boundary and dislocations as defect sinks.

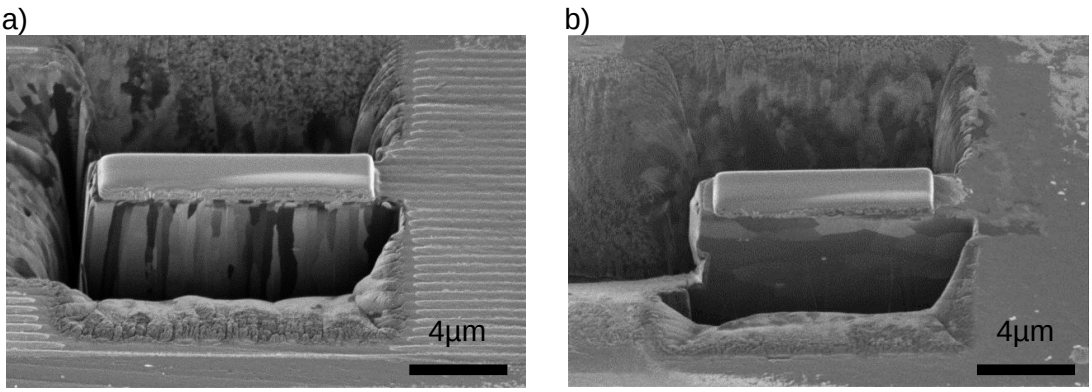

Figure 2.1.1 SEM image of half-made cantilevers in annealed (a) W-5Re wire and (b) W-5Re plate samples. Images are taken at 54^{o} tilt and 30kV in Nvision FIB-SEM.

2.1.1.3 Laboratory Manufactured Materials

The alloys: W-2Re, W-10Re, W-1Re-1Os and W-2Re-1Ta are unavailable commercially due largely to brittleness and/or toxicity [104-106, 110, 111], so, they were custom made at Oxford and Cambridge by Dr Christian Beck. Powders of W, Re, Ta and Os of >99.99at.% purity were purchased by Dr Beck from Sigma Aldrich and Alpha Aesar ltd. Dr Beck blended and compacted prior to being vacuum arc melted into hemi-ellipsoidal ingots, 10 – 15 mm in diameter. Following cooling to room temperature, they were wax mounted and a diamond slow saw cut them into 1mm thick slices.

The resulting plate samples have large grain size typically 1–3mm in diameter as ascertained via optical microscopy measurements (Table 2.1.1). These lab-made samples contrast commercial samples in form; they have no texture and possess very large grain size (Figure 2.1.2) and low dislocation density. To maintain a good

degree of reliability in this thesis, the lab-made and commercially procured samples were studied in parallel with each other. Thus, W, W-5Re and W-25Re materials (commercially available compositions) were also lab-made and included in Table 2.1.1.

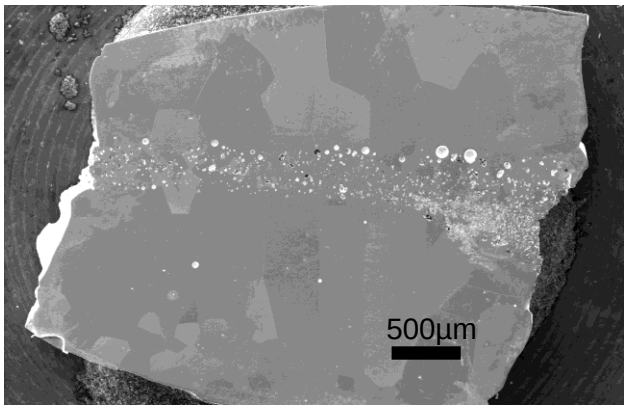

Figure 2.1.2 SEM image of as polished W-2Re alloy. Imaged at 30KV using Nvision FIB-SEM.

2.1.2 Pre-Irradiation Sample Preparation

2.1.2.1 Heat Treatment

The purpose of annealing is to reduce the dislocation density without altering grain size or texture. Based on previous studies [30], some of the tungsten and tungsten alloys were annealed at 1373K for 24 hours. An argon filled vacuum tube furnace is used for such heat treatment to avoid oxide formation. Others were deliberately left in an unannealed state to determine effect of dislocation density on clustering.

2.1.2.2 Electropolishing needle samples

To make atom probe needles for implantation, the 0.25mm diameter Goodfellow wires were cut to lengths of 10mm and electropolished in a 5wt% NaOH solution.

The schematic is illustrated in Figure 2.1.3a). The NaOH solution was retained in a 250mL beaker, suspended as a ~8 mm thick layer above a dense, inert fluorocarbon solution: Galden®. The wire was held by a tweezer and suspended vertically within the layer of NaOH solution. A gold metal piece is also immersed in this solution to complete the electrical circuit. Following literature guidelines [112], 5-8V was applied causing the wire to be etched into an hourglass figure, becoming progressively thinner until it fractures. At the point of fracture, the current was immediately stopped and the two sharpened wire needles were carefully extracted. The needles were cleaned in distilled water and then crimped into a 2mm diameter copper tube, prior to storage in vacuum desiccator. Approximately, 5-10 samples were made of each alloy for each irradiation experiment.

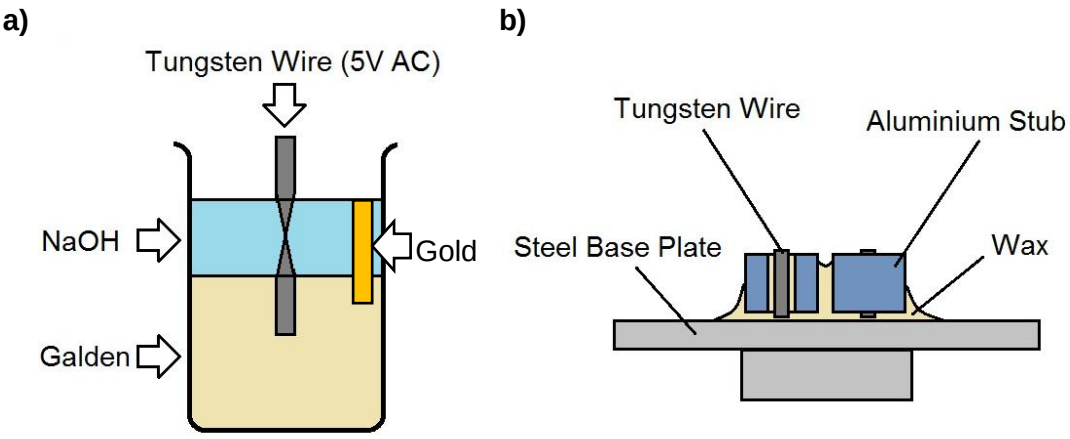

Figure 2.1.3 (a) Electropolishing setup for 0.25mm diameter wire (b) Schematic setup for grinding and polishing 1mm diameter tungsten alloy wire.

2.1.2.3 Grinding and Polishing of Bulk Samples

To prepare plate materials for irradiation, grinding and polishing techniques were used. Samples were hot wax mounted onto a circular stainless steel base plate and spaced equally apart along the periphery. During the grinding stage, the sample thickness was reduced from 1mm to 0.5mm using SiC grit paper of grades P100-P4800. The exact time spent at each stage varied with the quantity of samples; optical microscopy was used to check for bevelling and scratches prior to continuation to next step. The subsequent polishing stages involved 3μm and 1μm diamond pastes, with a minimum of 3 hours spent at each polishing stage. A final 5 hours, 45nm grit colloidal silica polishing was applied to achieve a high quality surface free from damage.

For the 0.75-1.00mm diameter wire samples, a special mounting setup shown schematically in Figure 2.1.3b) was used, to polish the wires in cross-section. Wire samples, 10mm in length, were inserted and wax mounted into pre-drilled 10mm high aluminium stubs. The same grinding and polishing stages were applied as for the plate samples; the softer aluminium stabiliser introduces minimal scratches on the tungsten alloy surface. This new method of preparing wire samples proved very effective. The surface finish achieved was the same as that of the plate samples. Given the expensive cost of purchasing W-Re samples, this reduced the quantity of samples required for irradiation whilst still providing more than enough analysis area for post-irradiation nano-scale analysis.

2.1.3 Ion Implantation

2.1.3.1 Self-Ion Irradiation Experiments

Fluence (W^+/cm^2)	Dose (dpa)	Temp (K)	Alloys
$1.00x10^{14}$	1.2	773	(W, W2Re, W5Re, W10Re, W25Re)
$1.00x10^{14}$	1.2	573	(W, W3Re, W5Re, W25Re)
$3.00x10^{14}$	3.9	773	(W, W2Re, W5Re, W10Re, W25Re)
$2.50x10^{15}$	33.0	573	(W2Re, W5Re, W10Re, W25Re, W1Re1Os, W2Re1Ta)
$2.50x10^{15}$	33.0	773	(W2Re, W5Re, W10Re, W25Re, W1Re1Os, W2Re1Ta)

Table 2.1.2 Irradiation conditions and materials studied in this thesis.

W^+ ion irradiation was used to simulate the displacement damage effects of neutron irradiation. The Tandem Ion Accelerator at the National Ion Beam Centre, University of Surrey was used to irradiate all materials studied here. All irradiation experiments involved 2MeV W^+ ion implantation at a flux: ~$3.06x10^{10}W^+$ ion/cm^2s^{-1} and under vacuum: 10^{-6}mPa. Only the fluence and temperature were varied and a total of 5 different irradiation experiments were conducted. They are listed in Table 2.1.2 along with the materials irradiated. The two irradiation temperatures: 573 and 773K were chosen to lie on either side of the critical temperature of vacancy activated migration in W: 743K [113]. Hypothetically, either a self-interstitial (573K) or vacancy (773K) dominated cluster effect was favoured for each temperature.

2.1.3.2 SRIM Prediction of Radiation Damage

SRIM software [51, 52] was used to predict the damage profile from ion irradiation in a tungsten sample using a W^+ ion energy 2MeV and displacement energy 68eV. Full-damage cascade model was selected which predicts all displacements within a collision cascade. The choice of 68eV displacement energy was obtained through averaging across all crystallographic directions for tungsten [11, 53, 59, 114].

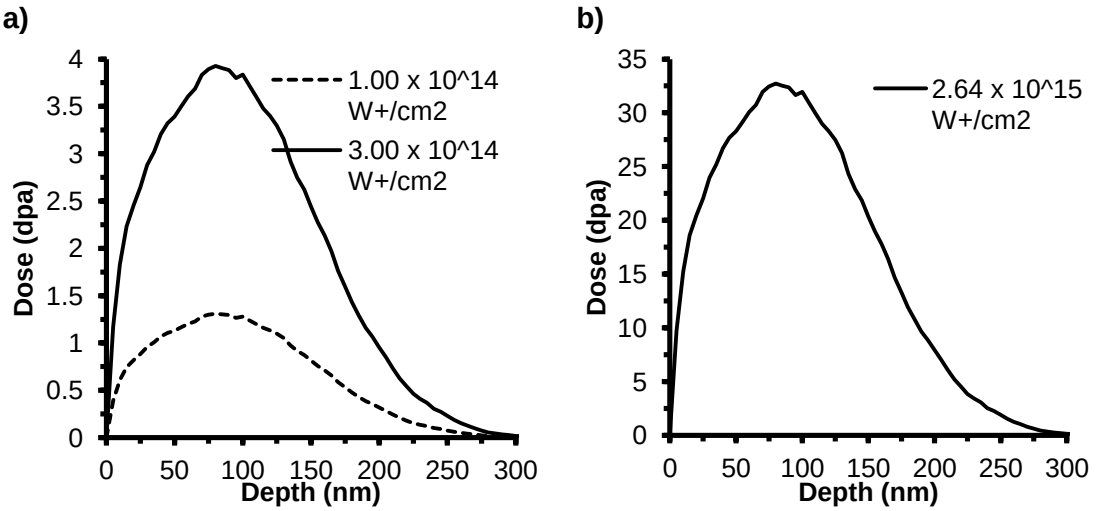

Figure 2.1.4 SRIM prediction of damage profile in tungsten for fluence a) 1.00×10^{14} (dotted) and 3.00×10^{14} (undotted) and b) 2.50×10^{14} W^+/cm^2.

To estimate the dose measured in displacements per atom (dpa), SRIM outputs vacancy per ion values as a function of depth, which, along with the atomic density and flux were substituted into the equation in §1.4.3 to calculate the displacements per atom (dpa). The damage profile (in dpa) for the fluences listed in Table 2.1.2 are shown in Figure 2.1.4a-b). The damage extends for 300nm and peaks at 125nm. The representative dose was taken as the peak of each profile.

It is difficult to apply SRIM predictions to needles because they possess a rounded, tapered surface at an angle to the ions which reduce the degree of damage. Needle samples have a large surface area which potentially acts as defect sinks as well. The clustering induced in needle samples will be compared against bulk samples to evaluate their effectiveness.

2.1.4 Lift-Out Method for Atom Probe Analysis

Whilst post irradiated needles were immediately ready for atom probe analysis, the lift-out method was applied to bulk samples to make atom probe needles. A Zeiss Nvision Dual Beam FIB at Oxford was used. Firstly, a 2 by 10μm, ~1μm thick carbon layer was deposited onto the sample surface using Ga+ ions. The deposition process introduces Ga+ ion damage within the sample which SRIM predicts the penetration to be ~15nm. This damage depth is relatively small in comparison to the W+ ion damage depth: 300nm. To account for this, the cluster analysis is excludes this Ga+ ion damage region. The deposited carbon layer marked the material surface and protected against further Ga^+ ion damage. As shown in Figure 2.1.3a), the area surrounding the carbon marker was then milled out to ~8 μm deep trench forming a rectangular slice. Progressively finer milling currents (6.0-1.2nA) were used to minimise the degree of tapering on all sides. A 45^o undercut at 6μm was then made to leave only one side of the slice attached to the bulk. Then, a micromanipulator needle was inserted and attached to the free end of the cantilever via tungsten gas deposition. The fixed end of the cantiliever was milled away to free it from the material surface and lifted out above the sample as shown in Figure 2.1.5b).

The cantilever was transferred to a silicon microcoupon (CAMECA), composed of 6 by 6 array of flat top micron sized silicon posts [112]. As shown in Figure 2.1.5c), the cantilever was carefully positioned to lie directly above a particular silicon post leaving an overhang of triangular shape cross-sectional area. Tungsten deposition was then used to attach the sample to the silicon post, before it was cut from the main cantilever. This series of steps were repeated on adjacent empty silicon posts.

a) **b)**

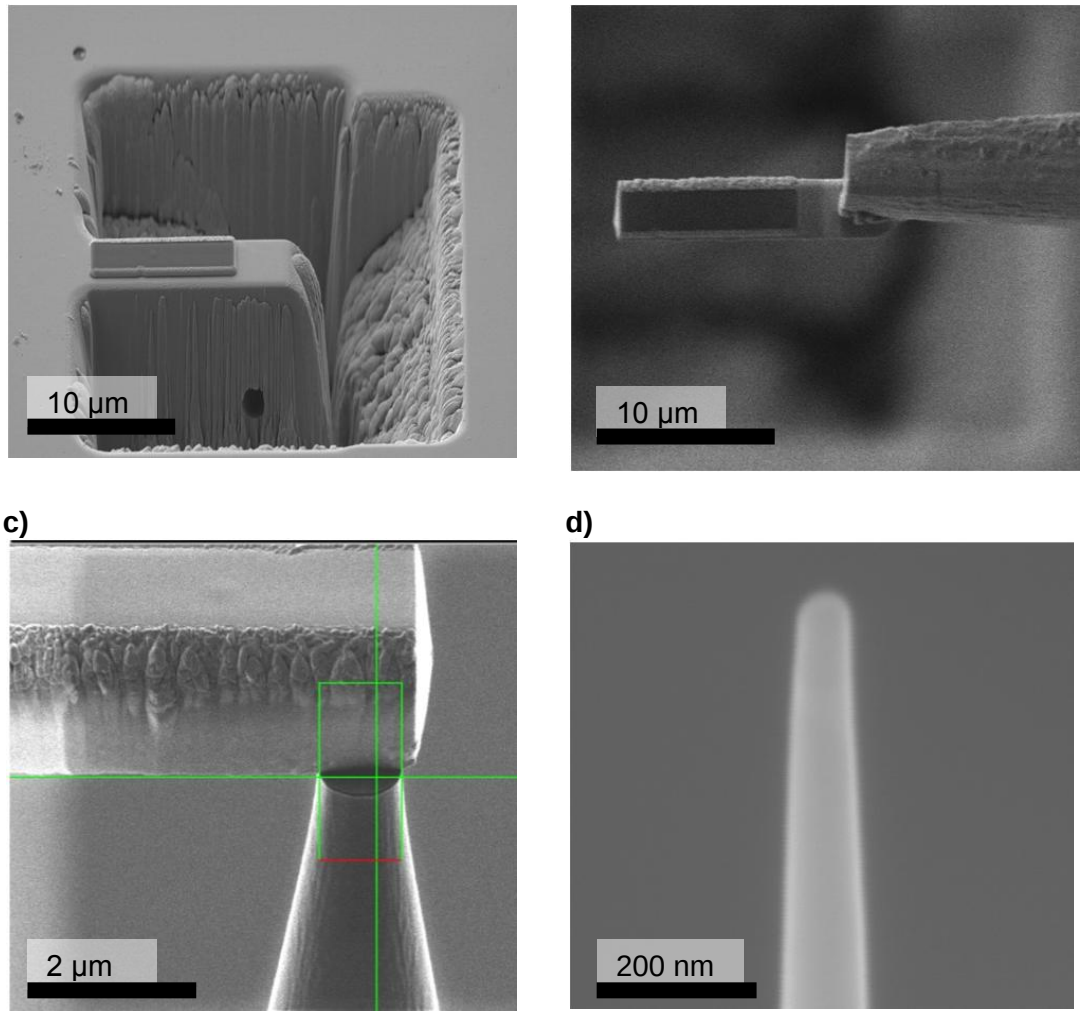

Figure 2.1.5 a) Carbon protection layer on tungsten surface in process of being milled into a cantilever. b) Final cantilever after being lifted out of the sample via micromanipulator. c) Cantilever touching silicon flat top post, green rectangle indicates area for imminent tungsten deposition. d) Final atom probe tip after several milling stages.

The final stage was shaping the mounted samples into needle shapes of less than 100nm end diameter. The annular milling tool available in the FIB software was used to progressively reduce the diameter of the sample to the desired value and shape, as illustrated in Figure 2.1.5d). A final low energy 2kV clean was used to ensure that no more than 20nm of carbon was left on the needle tip. This process of

manufacturing proved very effective, as 3-4 successful atom probe runs of more than 200nm depth were achieved from ~6 needle samples for each sample analysed.

2.1.5 Transmission Electron Microscopy

The samples for TEM analysis were also made in NVision FIB-SEM via a similar lift-out technique. Once the cantilever was made and extracted in Figure 2.1.3b), it was tungsten gas deposition mounted onto the side of a 3mm diameter copper half grid. The free-hanging cantilever was thinned progressively down to electron transparency (50-100nm thickness) by milling from either side. The TEM sample manufacturing procedure was in accordance with a guideline designed to limit Ga^+ ion damage [115].

TEM samples were imaged at 200kV under bright field conditions in the JEOL 2100 TEM using a Gatan Orius CCD camera. The lift-out sample was 8μm deep, so it features regions of radiation damage and unimplanted substrate. TEM analyses undertaken in this thesis are mostly presented at a qualitative level, as the dislocation density following 1.2-33dpa doses were saturated, making quantitative measurements of dislocation loops excessively difficult [11, 74, 96]. Re has very similar electron scattering factor to W, hindering imaging of the (coherent) clusters formed [86].

2.1.6 Nanoindentation

A Nanoindenter XP at Oxford was used, operated by Dr Dave Armstrong and Dr Christian Beck. A Berkovich diamond tip, calibrated against fused silica, was used to make indents over a minimum of 3 grains as 4 x 4 array, to a depth of 0.5-1.0μm. The Continuous Stiffness Method (CSM) was used, which gives hardness data as a function of depth.

To find a representative hardness in the irradiated material it was necessary to use data from a depth range where the effect of tip imperfections and where interference from the substrate were minimised. Oliver et al. and Armstrong et al. [11, 95] found the optimal range for measuring hardness to be 50-200nm beneath the irradiated surface. In the materials tested, a peak in irradiation hardness was found to fall within this depth range at 125nm, so the irradiation hardness at 125nm depth was thus taken as the representative hardness of the samples. The hardness results will inevitably contain size and substrate effects but it's the minimal level possible and I am being consistent in selecting hardness at 125nm.

2.2 Calibrating Analysis Parameters in Atom Probe Tomography

2.2.1 LEAP 3000 SI vs LEAP 3000 HR

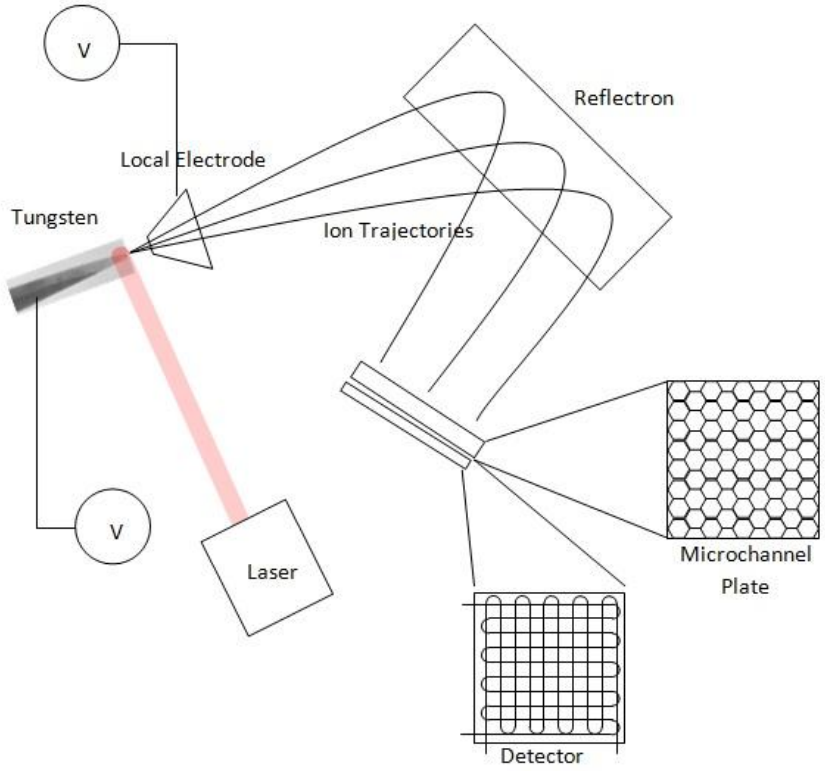

Figure 2.2.1 Schematic setup of the operation of the LEAP 3000X HR.

Two different atom probe machines were used: LEAP 3000X HR and LEAP 3000X SI (hereafter referred to as 'HR' and 'SI' respectively). The HR model has a component called a reflectron which plays a critical role in enhancing the mass resolution. It acts as an electrostatic lens minimising any kinetic energy differences among co-evaporated ions having the same mass-charge ratio (Figure 2.2.1). As tungsten ions of both low and high kinetic energy enter the reflectron, the higher kinetic energy ion travels through a greater distance, leading to the same arrival time at the detector as an ion evaporated at the same instant but with lower kinetic energy. Without the reflectron, the higher kinetic energy ion is detected earlier than the low energy one, resulting in a mass spectrum with broader, less-well resolved

peaks. However, the reflectron contributes to the low 37% detection efficiency of the HR model. The design of the SI model offers a higher detection efficiency of 67% [112, 116, 117], although the absence of a reflectron compromises data quality.

a)

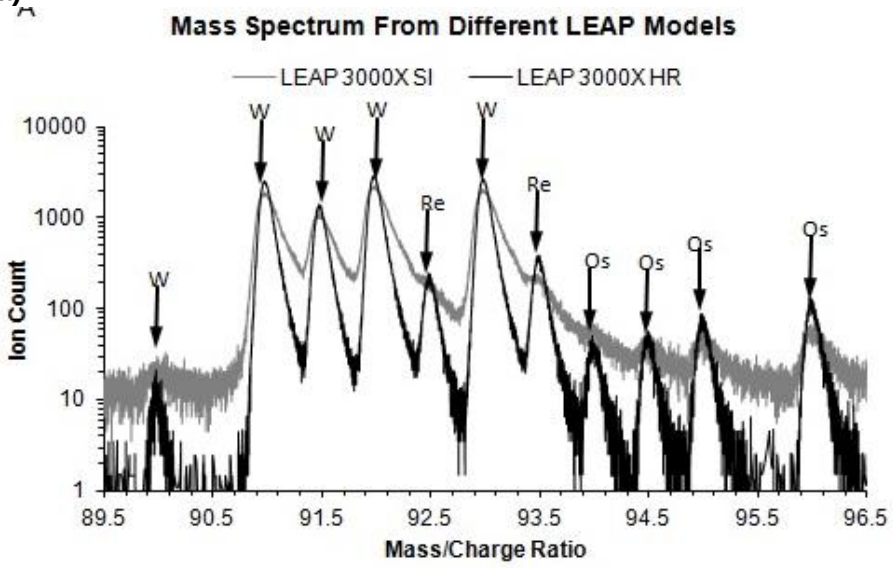

b)

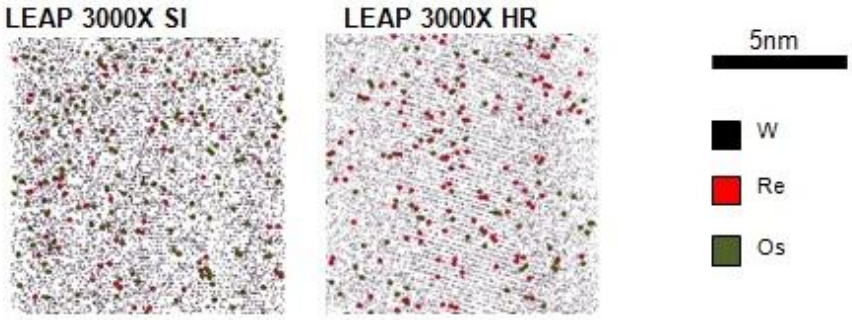

Figure 2.2.2 (a) Atom probe mass spectra of W-1Re-1Os in LEAP 3000X SI and LEAP 3000X HR. (b) 3nm thick slices through APT maps for the respective SI and HR models showing the W, Re and Os atoms.

To determine the most suitable machine for cluster analysis, a control W-1Re-1Os sample was analysed. Needle samples were made as per §2.1.4, and subsequently examined in both LEAP systems. To minimise the effect of other variables, the following operating parameters were kept constant: pulse energy (0.8nJ),

temperature (50K) and specimen radii (80nm). As shown in Figure 2.2.2 a), the mass spectra for 2+ charge ion peaks show a large difference in mass resolution between SI and HR. The Full Width Half Maximum (FWHM) peak resolution ($M/\Delta M$) for the ^{184}W 2+ ion was found to be 1224 for HR and 554 for SI, a twofold difference. Even though the SI can detects more solute atoms (as shown in the atom maps of Figure 3.2.2 b), the composition of W-Re sample will be less accurate due to peak overlaps from W and Re isotopes having very similar mass-to-charge ratios. The need to accurately measure cluster composition was judged to be a more important criterion than detection efficiency in the current study, therefore all subsequent analyses were carried out using the HR model.

2.2.2 Voltage Mode vs Laser Mode Analysis

The next stage is deciding whether to use laser or voltage mode for specimen analysis. The two modes evaporate ions from the needle tip by different means. The laser mode heats the tip, lowering the field required for atoms to ionize and evaporate. Because the sample cools within 1ps it does not interfere with the arrival of the next pulse, which is every 4µs (pulse frequency of 250000kHz) [112]. Voltage mode induces evaporation by locally increasing the field at the tip using a voltage pulse to above the threshold evaporation value. Laser mode has been recognised as being a more gentle approach to analysing samples because it avoids the cyclic stresses induced from voltage pulses [112, 118], thus minimising the probability of sample fracture. It is therefore especially suited for this work since the majority of our samples are bulk lift-out tungsten needles which are particularly brittle (due to the Si post and material itself), especially following irradiation treatments.

2.2.3 Calibrating Analysis Parameters

Calibration experiments for four APT analysis parameters: laser pulse energy, evaporation rate, stage temperature and pulse frequency were undertaken to find the optimal values. First, it is necessary to define and explain their ranges and units. The LEAP 3000X HR uses a green, 400nm wavelength laser that is focused on the tip as a ~1μm sized dot. The laser energy is pulsed at regular intervals and the energy of each pulse is in the range 0.1-5nJ. In one second, the number of laser pulses that hits the needle is called the “pulse frequency” expressed in kHz. As the atoms evaporate from the surface, the probability an atom will be evaporated per pulse (evaporation rate) falls within the range: 0.1–1.0%.This is directly controlled by the rate of increase of the specimen standing voltage. Finally, the “stage temperature” is the temperature at which the sample is cryogenically maintained at, typically 15-70K.

2.2.3.1 Laser Pulse Energy

Calibration tests were carried out on a single W-5Re electropolished wire sample analysed at constant evaporation rate, specimen temperature and pulse frequency of 0.5%, 50K and 200kHz respectively. This particular study examined the effect of laser energy on the ion charge distribution and lattice resolution. Both factors are linked to the evaporation field on the specimen surface as well as specimen temperature during evaporation. The purpose of this calibration study was to find the highest laser energy that can be used without compromising data integrity.

Half a million ions was collected at 11 different laser energies from 0.5 to 1.5nJ inclusive. 11 sets of mass spectra were generated from which the peak resolution and charge distribution were calculated. In all 11 data sets, the Full Width Half

Maximum (FWHM) for the $^{184}W\ 3^+$ ions remained constant at a value of 1226. The lack of degradation with increasing energy suggests the heat from laser pulse was quickly transferred away, preventing interference with subsequent pulses.

The percentage of 2^+, 3^+ and 4^+ charged tungsten ions are plotted in Figure 2.2.3e) across the specified energy range. With increasing pulse energy, the 3^+ charge was maintained at a constant value of 95% until 0.9nJ, whereupon it began to decrease and approach a new plateau of 50%. These charge abundances are a reflection of the critical evaporation field at the tip surface. A 50% abundance of W 3^+ charges indicates the field is low, an undesirable state linked with reduced spatial resolution [119, 120]. As shown in Figure 2.2.3 a-d), the resolution of poles in the density maps is considerably blurred beyond 0.8nJ [53]. On the other hand, a 0.5nJ pulse energy averts this issue since the critical evaporation field is much higher, although a much higher standing voltage was needed to induce evaporation which increases probability of fracture [119, 120]. Taking these two factors into consideration, one can then infer 0.7-0.8nJ would be the optimum pulse energy for analysing clusters.

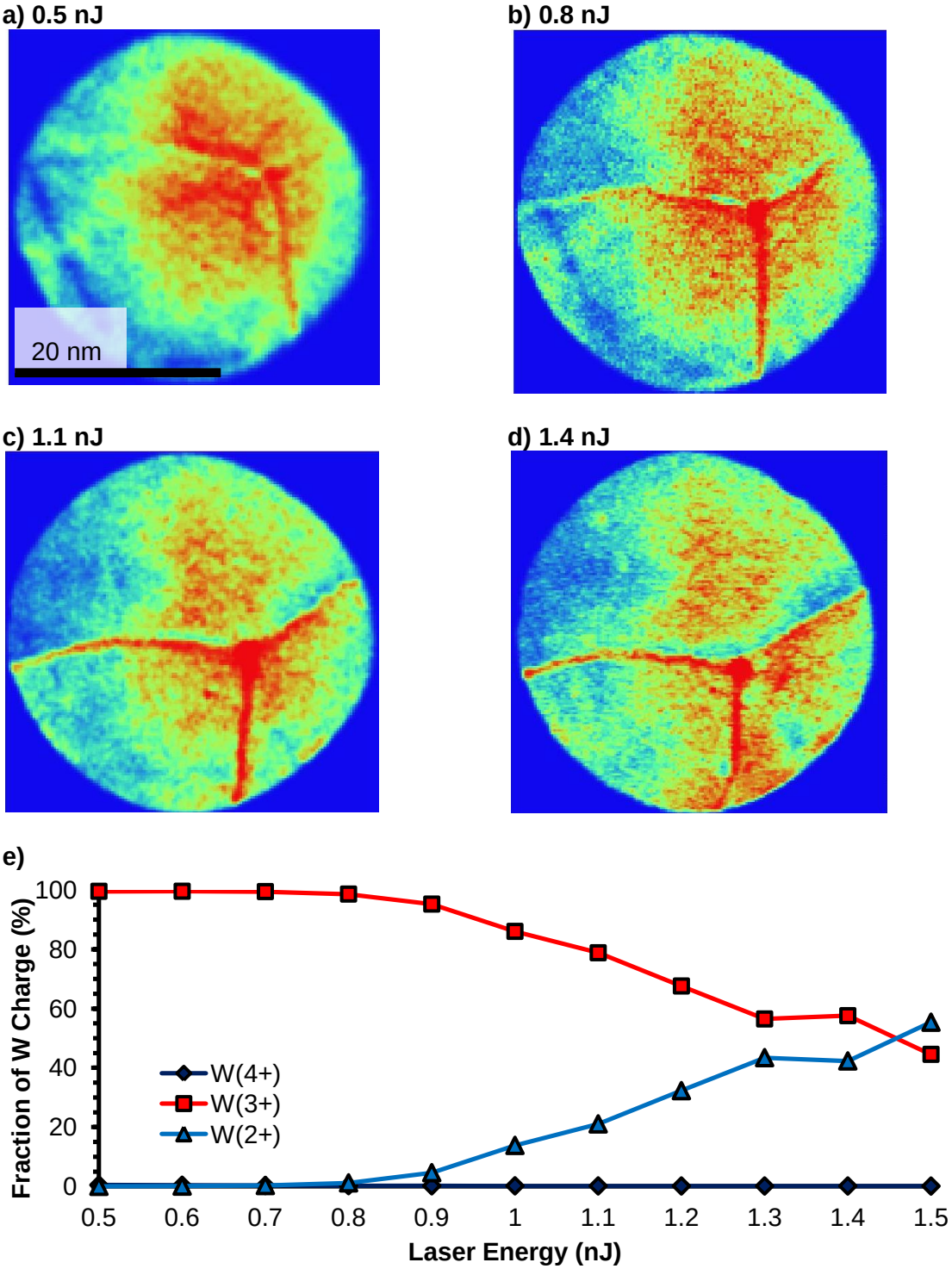

Figure 2.2.3 Cluster number density contour map for pulse energy a) 0.5; b) 0.8; c) 1.1 and d) 1.4 nJ. e) Charge states of W in a pure tungsten at different laser energies.

2.2.3.2 Evaporation Rate

The effect of the evaporation rate on data quality was examined in a separate calibration experiment, with half a million ions recorded at each target evaporation rate (0.2% to 1.0%) on a pure tungsten needle at constant laser pulse energy of 0.7nJ, pulse frequency 200kHz and specimen temperature 50K. In setting different evaporation rates, the LEAP system controls the rate of voltage increase on the sample accordingly. A total of 9 data sets were collected. No trends could be observed for peak resolution or charge states with changing evaporation rate, but a large effect on the extent of background noise in the mass spectrum present was noted. Figure 2.2.4 plots the background noise (all non-ranged hits detected) as a function of evaporation rate. The graph shows an exponential increase in noise as the evaporation rate decreases towards 0.2%. The noise level is very high between 0.2-0.4%, only beginning to level off at evaporation rates greater than 0.5% towards a more acceptable noise background level of 20%. While increasing the evaporation rate increases the probability of specimen fracture, this is also balanced by the demand to minimise background noise and optimise the rate of ion collection. This calibration study showed 0.5% is a good compromise evaporation rate for laser energies above 0.7nJ, which is therefore set for all samples subsequently analysed.

2.2.3.3 Stage Temperature

Half a million ions were collected at temperatures of 30, 40, 50 and 60K from the same W-5Re alloy electropolished needle. All other parameters were kept constant, at 0.8nJ laser energy, 0.5% evaporation rate and 200kHz pulse rate. According to the literature [112, 121, 122] a lower temperature should enhance the lattice resolution of the sample thereby increasing the spatial accuracy of the data and any

identified clusters. This trend is apparent if we compare qualitatively the <110> pole lattice images at the four temperatures, as shown in Figure 2.2.5. These figures are 5nm thick slices extracted from the original reconstructions, with tungsten and rhenium both given black pixels to visualise lattice planes clearly. The resolution does drop as temperature increases from 30 to 60K but it is accompanied by a reduced chance of specimen fracture [112]. To balance these opposing factors, an analysis temperature of 50K was selected for all samples analysed.

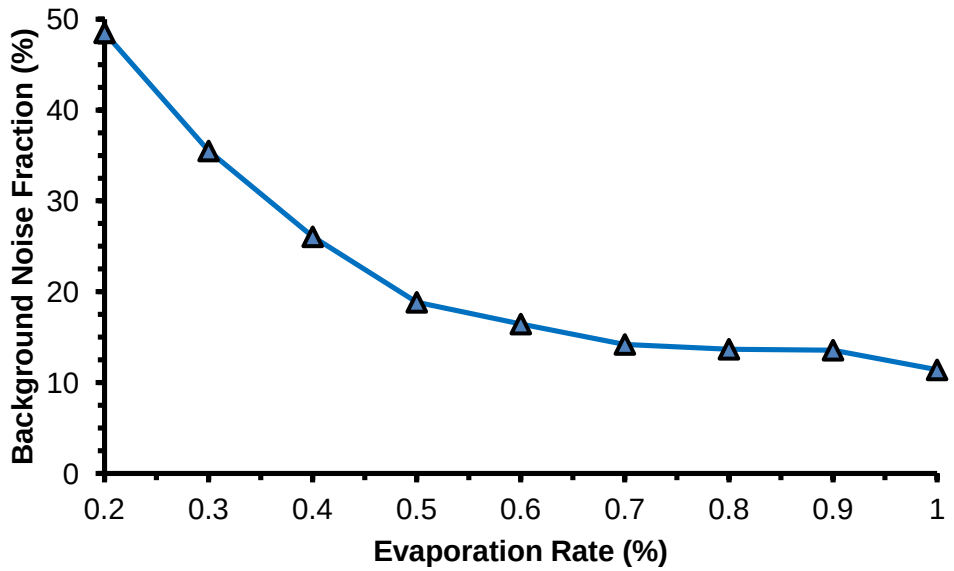

Figure 2.2.4 Effect of evaporation rate on background noise at 0.7nJ laser energies

2.2.3.4 Pulse Frequency

Half a million ions were collected at frequencies of 50kHz, 100kHz, 160kHz, 200kHz and 250kHz on a W-5Re alloy. The pulse energy, temperature and evaporation rate were kept constant at 0.8nJ, 50K and 0.5% respectively. Figure 2.2.6 shows that no trends in measured Re content with pulse frequency were discernible. Using a smaller pulse frequency would limit the rate of ions detected in the LEAP, but too high a pulse frequency increases the probability of specimen fracture. A pulse frequency of 200kHz was used, as the best compromise between these two factors.

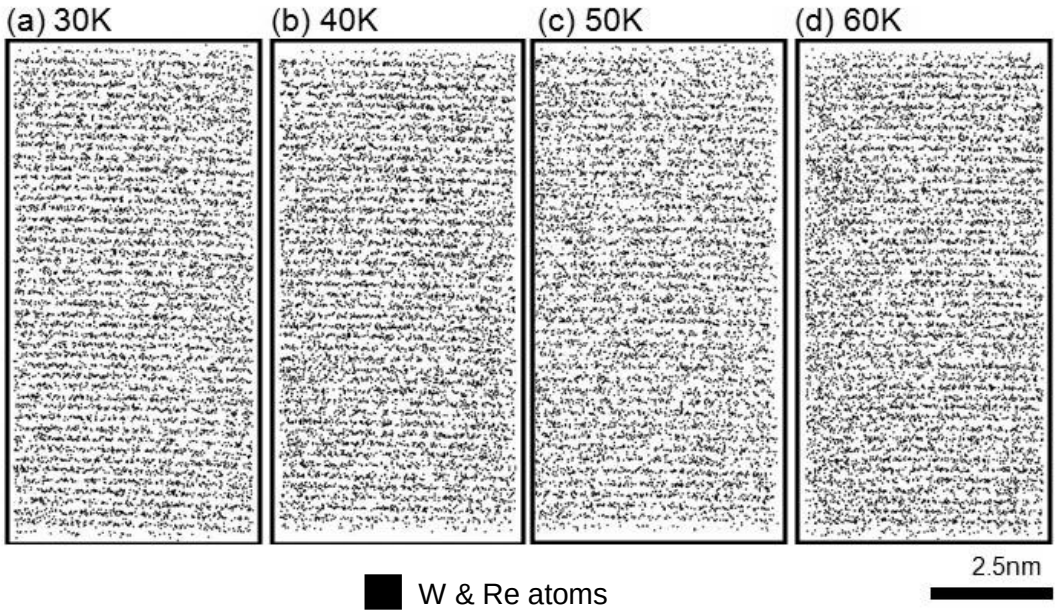

Figure 2.2.5 Slices of 5nm thickness of tungsten atoms taken from reconstructions analysed at temperatures (a) 30K; (b) 40K; (c) 50K; (d) 60K. It was found Re has a uniform distribution across all four temperatures. To highlight the lattice planes more clearly, the W and Re atoms are prescribed the same colour.

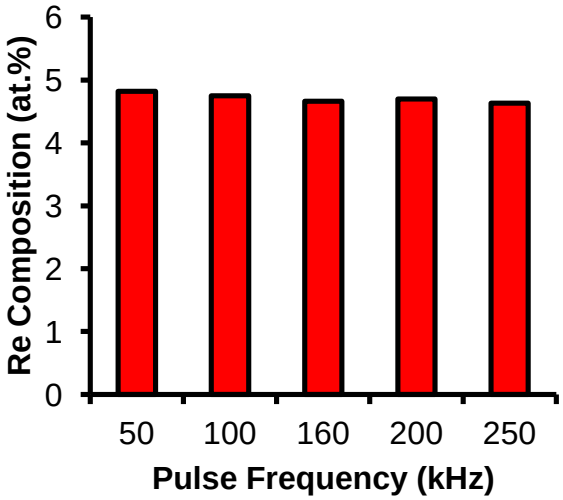

Figure 2.2.6 Effect of varying laser pulse frequency on a W-5at.%Re sample on measured Re composition.

2.3 Cluster Analysis

2.3.1 Maximum Separation Method

The maximum separation method [112, 123] is a widely used method for cluster identification, suitable for a range of cluster states: faint to distinct and small to large [85, 124, 125]. Five different parameters are required for this method: d-max, Nmin, order, L and e. The d-max value is a critical distance for determining whether solute atoms are potentially part of a cluster or not. In performing cluster analysis, the distance between a solute and the nth nearest neighbour solute is measured and compared against the d-max value. The nth value is called the order which, along with the d-max criterion, groups together solutes satisfying the criteria, producing a list of potential clusters. A filter is then applied to this list where clusters having total solutes less than a cut-off value, Nmin are discarded. The parameters envelope (L) and erosion (e) are used to refine the boundary between the cluster and matrix. The envelope value places a sphere of distance L around each solute atom belonging to a cluster and assigns all the atoms within this sphere as also belonging to cluster. The erosion value e removes a shell of atoms of thickness e from cluster surface.

2.3.2 Quantifying cluster characteristics

Having fixed all the necessary cluster parameters, cluster analysis can then be used to identify all the clusters within a reconstruction. The raw output from cluster analysis is a list of clusters tabulated along with their total atom count, spatial position, dimensions (measured along Cartesian co-ordinates), volume and composition. This batch of raw data can then be refined to calculate cluster

characteristics: average composition, average diameter, volume fraction and number density.

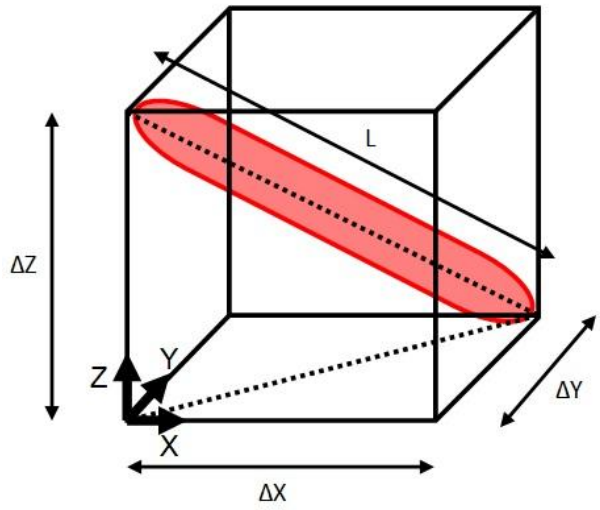

$$L = \sqrt{(\Delta Z)^2 + ((\Delta X)^2 + (\Delta Y)^2)}$$

Figure 2.3.1. How a cluster is measured in Cartesian co-ordinates using the cluster analysis tool in IVAS 3.6.6. The cluster length "L" can be calculated by Pythagoras theorem with the equation stated above.

The calculation of cluster composition is self-explanatory but, the latter three values involve some extra calculation steps. There were two cluster shapes found: spherical and rod shaped. Cluster shape was decided by analysing their aspect ratios. We use the Nabarro definition [126] to classify clusters having an aspect ratio below 2 as spherical. Where clusters are spherical in shape the dimensions along the z-axis is sufficient to represent cluster diameter, especially since the lattice plane spacing had been calibrated along this axis. Rod shaped clusters however, are generally at an angle to the Cartesian axis set; here the Pythagorean formula shown schematically in Figure 2.3.1 uses the Cartesian measurements to calculate the cluster length. This calculation is based on the underlying assumption that all rod

clusters are perfectly straight which is correct in ~95% of cases. Cluster volume fraction is calculated by dividing the total number of atoms forming part of a cluster by the total number of atoms in the reconstruction (both cluster and matrix). The number density is the total number of clusters detected divided by the reconstruction volume. The reconstruction volume is measured as a tapered cylinder.

2.3.2 Calibrating Cluster Identification Parameters

The “solute analysis” function in standard atom probe data reconstruction software: IVAS 3.6.6 was used to identify clusters. Following the IVAS 3.6.6 manual and atom probe texts [112], d-max is determined first, then Nmin and Order, followed the L and e values. As it is the intention of this study to quantify these clusters, the calibration procedure here is geared towards achieving highest level of data confidence. In the process, some real data might be lost but, it is a necessary sacrifice, especially since we are only seeing 37 % of the original data.

2.3.2.1 d-max

The cluster count distribution analysis plots the number of clusters found over a range of d-max values. Figure 2.3.2 shows such an analysis of data from a W-2Re alloy irradiated to 33dpa and 773K. The red coloured plot shows results for a data set where the chemical identities of all atoms have been “randomised” (using a script within IVAS 3.6.6) to represent an unclustered data set, while the blue plot is the “Experiment” data set that is clustered. The solid black line shows the unrandomised values minus the randomised values, taken as the “True” cluster count. The dotted black line shows the “Confidence level” which is the values in

"True" values divided by the "Experiment" values. The "Confidence level" concept was introduced by Williams et al [125] and give an indication of the fraction of clusters found in the experimental data likely to be due to the random distribution of solute atoms.

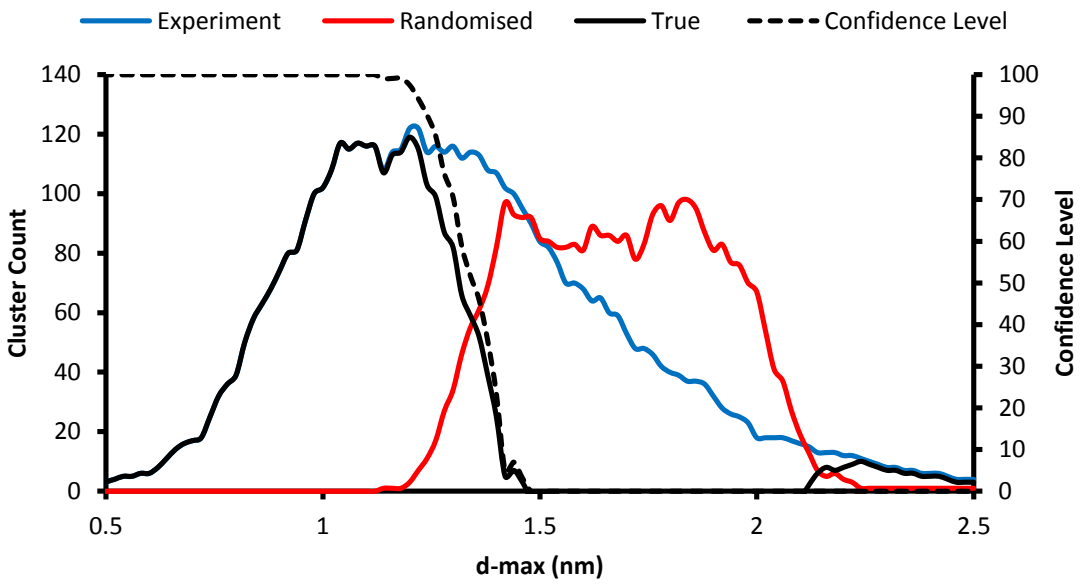

Figure 2.3.2 Cluster count distribution versus d-max for unrandomised sample (blue line) with clusters and randomised sample (red line) absent of clusters. The true clusters (black line) is found by subtracting the randomised from experiment count. The confidence level is the true clusters divided by the unrandomised values.

In the distribution plot for "Experiment", the cluster count peaks in the d-max range 0.8-1.4nm. Figure 2.3.3a) shows the averaged cluster composition and Figure 2.3.3b) the number density determined at 0.04nm intervals of d-max. The cluster number density plateaus in the d-max = 1.00-1.20nm range indicating the choice of d-max has no effect within this region. Further, the measured Re composition of the clusters reach a slower decrease above a d-max value of 1.12nm. Based on these two plots, the optimal value for d-max is 1.12nm, which lies in the middle of the plateau region of the cluster count distribution. Also, the "Confidence level" at

1.12nm is 98%. In selecting d-max for other irradiated samples, the d-max value will be selected for each dataset based on this approach.

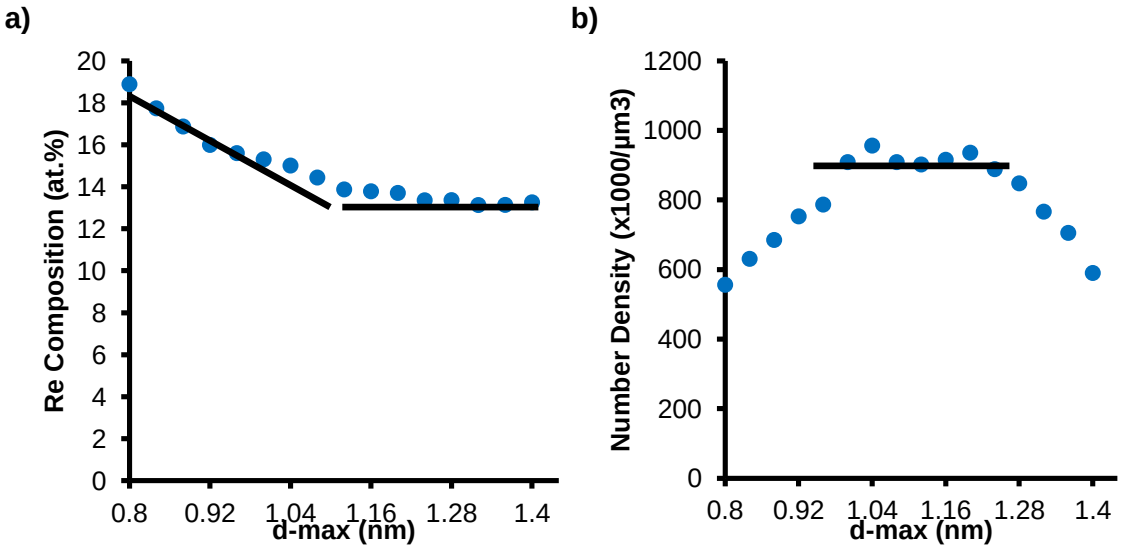

Figure 2.3.3 (a) Cluster Re composition calculated at different d-max values. (b) Cluster number density calculated at different d-max values.

2.3.2.2 Order

To determine the appropriate order parameter, the cluster Re composition, diameter, number density and volume fraction was calculated at various order values (in the range 2-30); these are plotted in Figure 2.3.4a-b). The d-max value used to achieve this analysis is taken at the peak of the “Experiment” plot as described in §2.3.2.1. Across all four plots, the cluster composition and number density plateaus becoming independent of order at values of 17–23. For cluster diameter and volume fraction, the curve slope becomes much shallower beyond this order value range. Thus, it appears small order values under-predict cluster size and misinterpret a large cluster as being composed of smaller clusters; larger order values by-passes smaller cluster so over predicts cluster size and volume fraction. Here, the median value of the range: 20 is selected for cluster analysis.

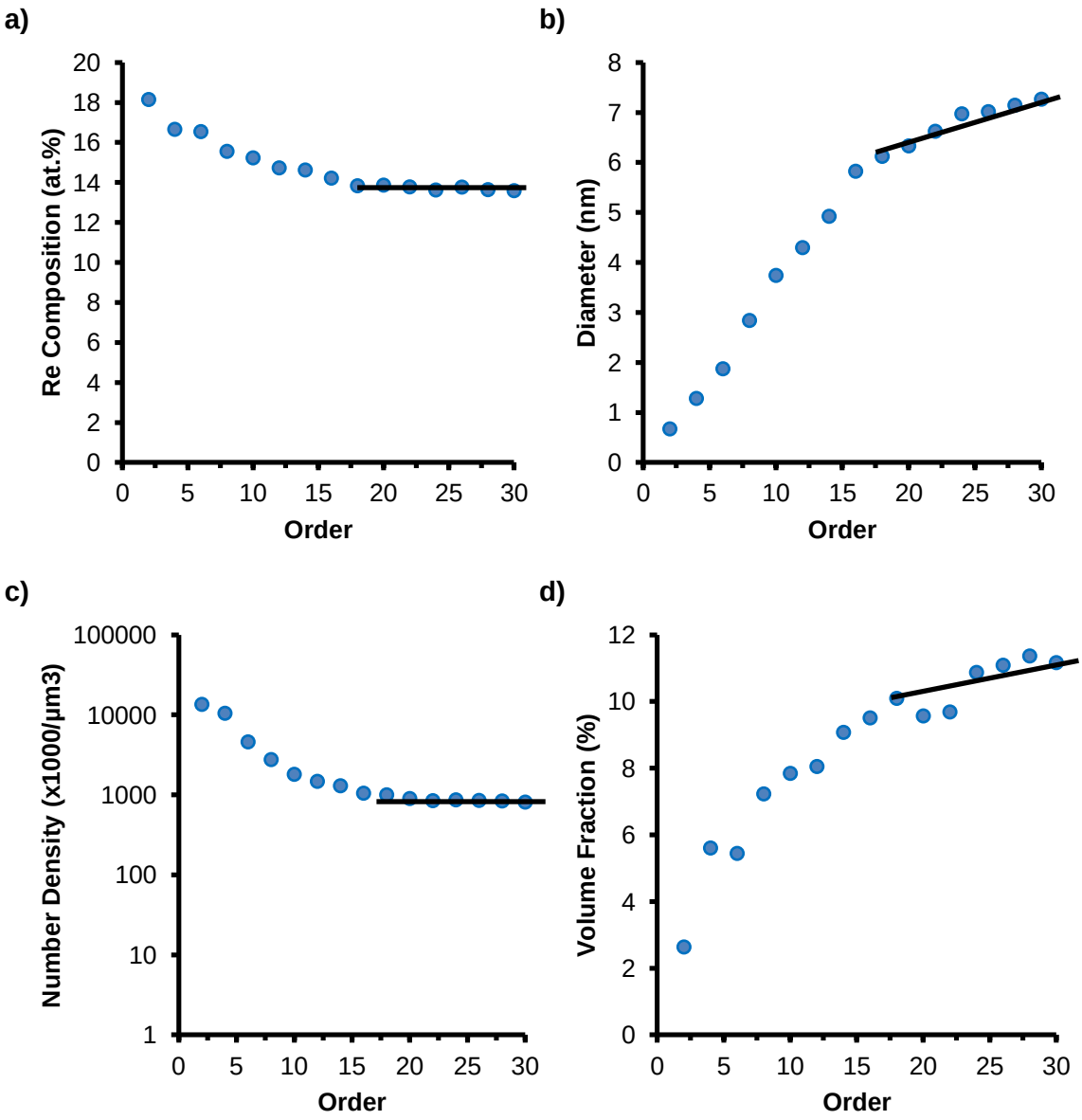

Figure 2.3.4 averaged cluster (a) Re composition; (b) Diameter; (c) Number Density and (d) Volume Fraction plotted against various order values.

3.3.2.3 Nmin

To find Nmin, cluster size analyses are performed for values of Nmin in the range 20-2000 for d-max=1.12nm and order=20. This analysis categorises the cluster sizes (measured in number of solute atoms) into different size ranges. Such distributions are plotted in Figure 2.3.5 for the “Experiment”, data set (blue) and a

compositionally “Randomised” dataset (red). The “Randomised” plot has a negligible cluster count dropping to values of 0 at Nmin of 20 – 22 which makes 20 the optimal value for Nmin.

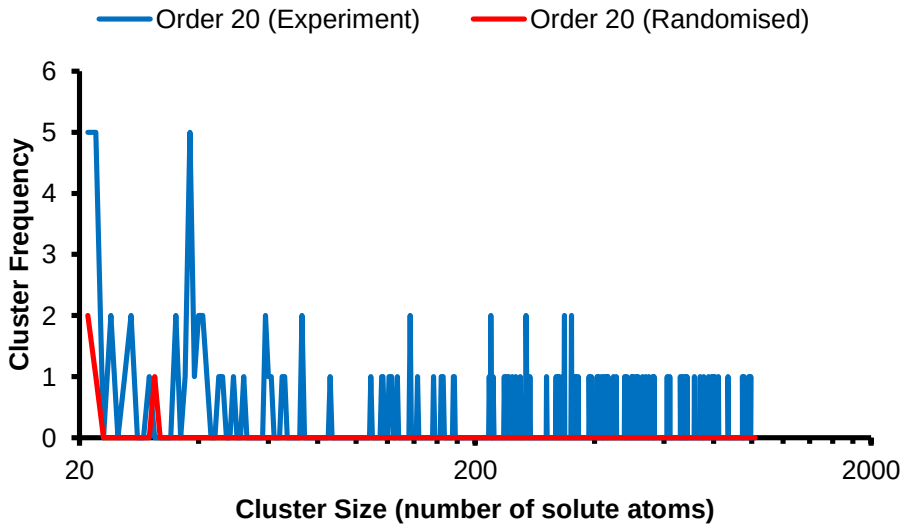

Figure 2.3.5 Cluster size distribution for W-2Re alloy at 33dpa 773K showing a “Experiment” and “Randomised” data set.

2.3.2.4 Selecting L and e Values

Following determination of the d-max, Nmin and Order values, the final two parameters requiring calibration are the L and e values. In this calibration test, the L and e values were changed systematically while the d-max, order and Nmin were kept constant at 1.12nm, 20 and 20 respectively. Table 2.3.1 shows calculated cluster compositions for various L and e values, with L expressed as a percentage of the d-max (“d”) while the e is a percentage of the L value. This simplification is done in order to generalise the values to be applicable to other alloys. Both L and e values control the degree of inclusion of matrix atoms in the clusters. They have an effect on the calculated cluster composition but have no effect on the number of clusters detected.

The composition plateaus for e values of 0.50L- 0.75L are highlighted in yellow. The transition point into a plateau occurs at L value of 0.50d, which indicates the inclusion of matrix atoms is just balanced by the degree of erosion. Thus, the most appropriate L and e values to use are 0.50d and 0.50–0.75L respectively.

L \ e	1.00L	0.75L	0.50L	0.25L	0.00L
1.00d	25.47	16.40	11.18	7.85	7.19
0.80d	23.71	16.04	11.26	8.51	8.05
0.60d	24.63	16.65	11.87	9.64	9.41
0.50d	28.89	18.12	12.84	10.88	10.70
0.40d	40.02	23.45	16.14	13.93	13.77
0.20d	58.89	45.96	41.22	40.29	40.17

Table 2.3.1 Array of averaged cluster composition measured for different "L" and "e" values.

2.4.2 Artefact Correction

The non-uniform evaporation field across the surface of the tip introduces local variations in evaporation field of the material. Whilst IVAS 3.6.6 attempts to account for the non-linear ion trajectories through "bowl correction", large deviations occur on <100> pole and cannot be entirely corrected [112]. Note the bowl correction is a complex mathematical correction which predicts the trajectory of all ions as following a parabolic path rather than a linear one. More details can be found in [112, 119]. The result of this is non uniform detection intensity in the reconstructed atom maps.

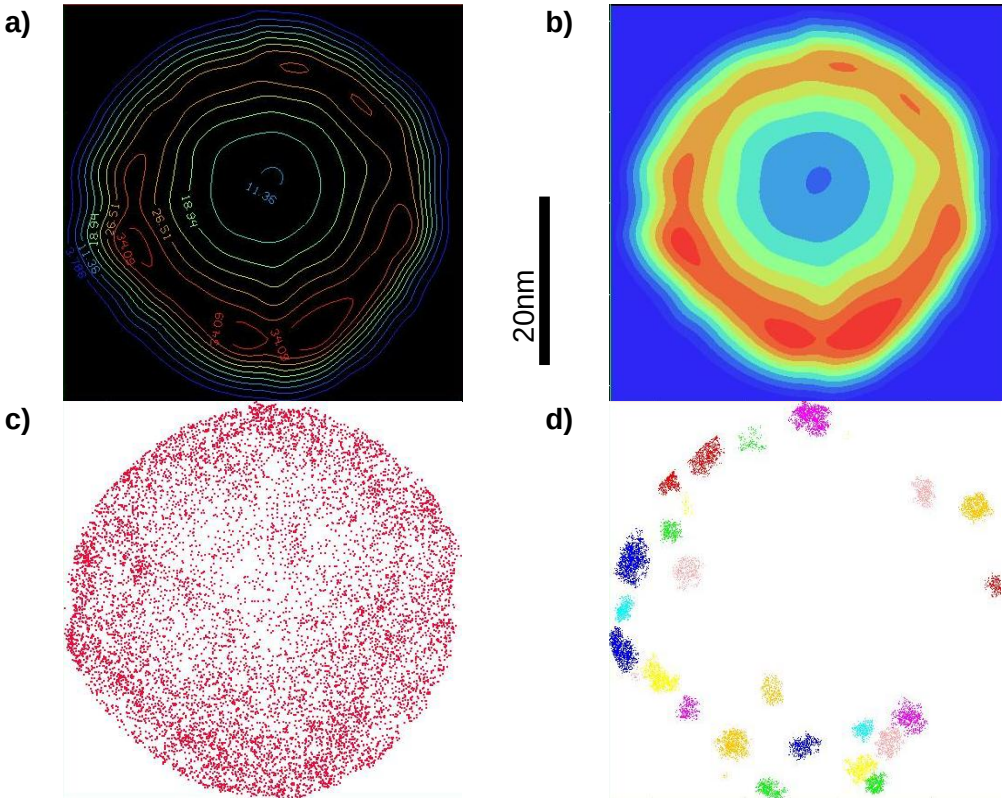

Figure 2.3.6 33dpa 573K W5Re plate sample, 5nm slice of the atom map reconstruction (a) Iso-density contour lines with values in units of atoms/nm3 (b) contour map with blue being the lowest density and red the highest density (c) Re atom map showing 100% of Re atoms (d) Clusters as identified with the cluster identification method.

The correction method described here was applied to W-5Re plate form alloy irradiated to 33dpa 573K, which has a <100> texture normal to the sample surface. This pole orientation results in a region of low density (large ion path deviations) at the centre of reconstruction. Other samples studied here have <110> texture whose pole produces a high density region in the resulting reconstruction which doesn't require such correction. Figure 2.3.6a-b) shows density contour plots imaged from the top and clearly illustrates the low density surrounding the <100> pole. The densities vary from 34 atoms/nm^3 at periphery of reconstruction to 11 atoms/nm^3 at

the centre; a threefold difference. To remedy this artefact, the reconstruction was partitioned into high and low density regions along the density iso-contour value of ~22 atoms/nm^3 (the median of the maximal and minimum density values) shown in Figure 2.4.7a-d). As a result, clusters within the higher density regions appear more distinct and can be identified with a smaller d-max value (1.00 nm) compared to much fainter clusters at the core which can be identified with a larger d-max value (1.20 nm). This approaches issues of overestimating or underestimating clusters cluster size when using a single d-max for the whole reconstruction.

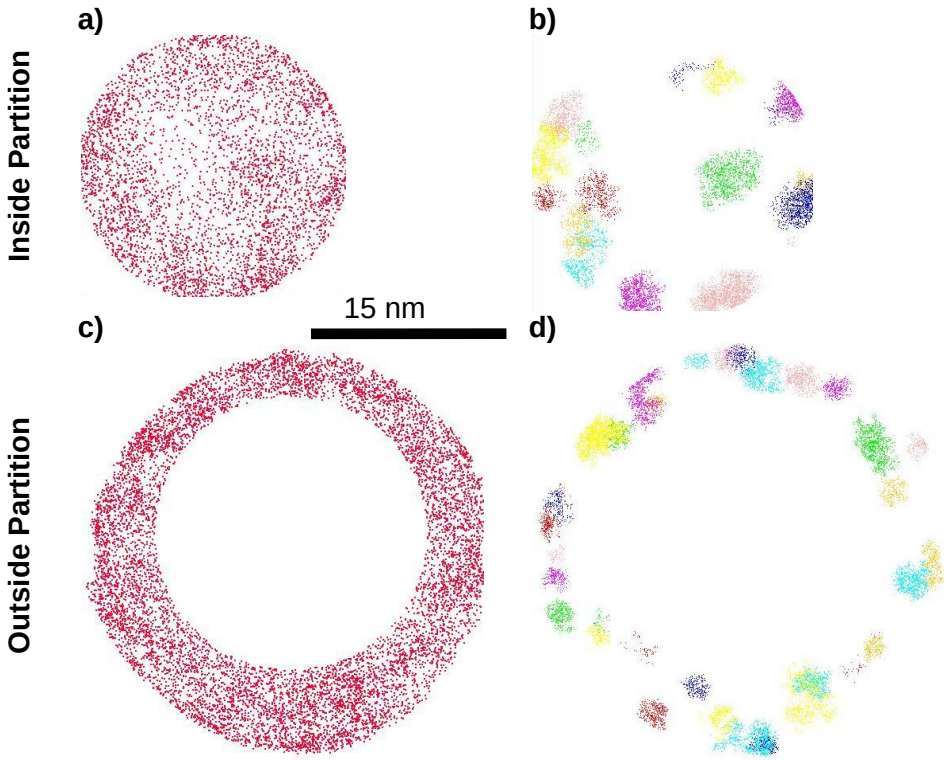

Figure 2.3.7 33dpa and 573K W5Re sample partitioned into two volumes of low and high density. A 10nm slice of the reconstructions is presented here. (a) and (b) show the Re atom map and clusters identified respectively in the low density partition. (c) and (d) show the Re atom map and clusters identified respectively in the high density partition.

3. Irradiation-induced cluster evolution in W-Re alloys

3.1 Introduction

This chapter focuses on irradiation induced Re clustering. There is limited literature data surrounding the chemistry and physical properties of clusters in W-Re alloys. They have only been identified as a precursor to precipitates [12] and are noted to be responsible for introducing an additional amount of hardening where otherwise hardening plateau would be observed in irradiated pure tungsten [11]. Comparable data on neutron irradiation induced precipitates exist on W-5Re and W-10Re samples exposed to neutron dose of 1.54dpa at 1023K [46]. The precipitate data, as quantified in the TEM, suggest increasing bulk Re composition decreases precipitate length and increases their number density.

APT is used here to characterise 3D chemical and physical properties of clusters. Around 3-4 samples are analysed per irradiated sample to account for variations within the material. This sample analysis frequency is also applied to analysis of other samples subsequent chapters. The effect of the cluster presence on mechanical properties will be discussed using data provided by Armstrong and Beck (personal communications). The hardness of the samples was measured by Armstrong and Beck using the Nanoindenter (§ 2.1.6) taken at 125nm depth which corresponds to the peak dose level.

The experiments conducted here involve lab-made W-Re alloys supplied by Christian Beck. Tungsten 2, 5, 10 and 25 at.% Re alloys were self-ion irradiated under doses of 1.2, 3.6 and 33 dpa at 773K (See §2.1.1). These samples are 1mm thick 10mm diameter plates ground and polished according to §2.1.2 prior to irradiation. The grain size of all the lab-made samples are 1-3mm in diameter,

measured via optical microscopy detailed in (§2.1.1). To identify and characterise the irradiation induced clusters, the maximum separation method detailed in §2.3.2 was used.

3.2 Cluster Evolution With Re Alloy Composition and Dose

3.2.1 Evaluating Clustering Variation with Depth

a)

b)

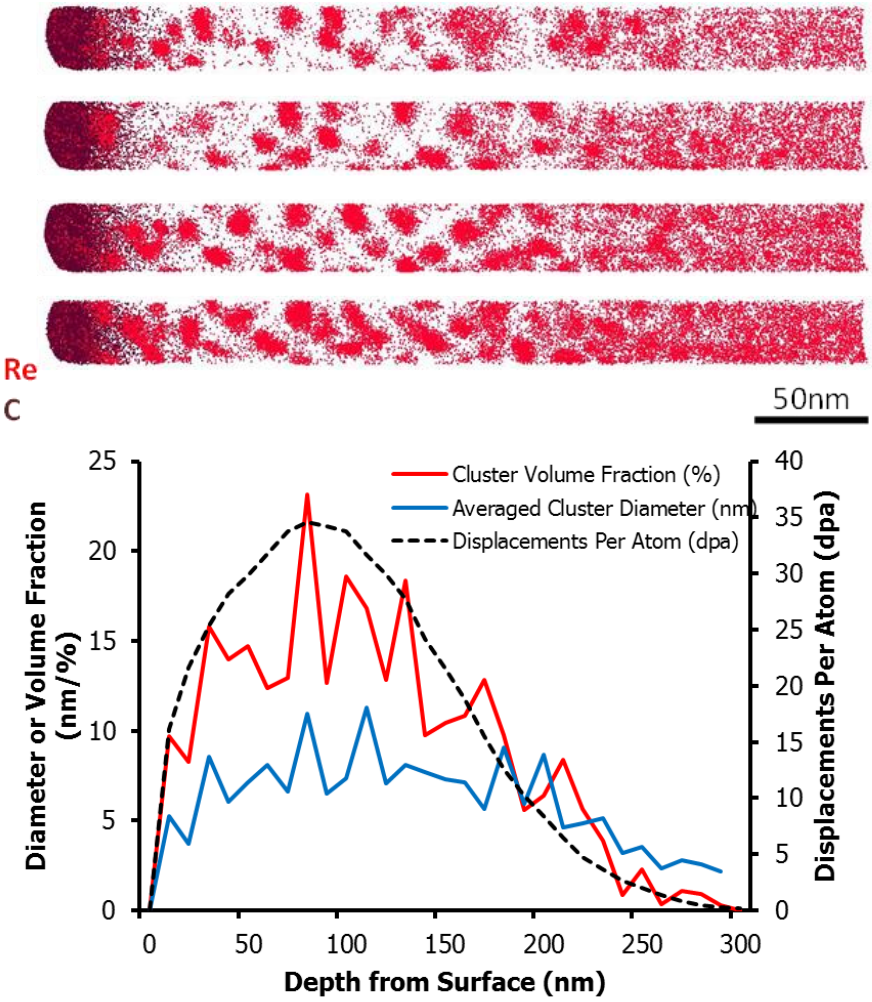

Figure 3.2.1 (a) 4nm thick slices through atom map of a W-2Re sample following 33dpa irradiation at 773K. Re (red) and C (brown) atoms only shown, showing Re clustering throughout first 200nm. (b) Variation of the cluster diameter and cluster volume fraction measured at regular 10nm slices from the reconstruction. The corresponding dpa level at different depths as predicted by SRIM is also shown.

To evaluate the variation of clustering with depth, W-2Re sample irradiated to 33dpa and 773K was selected. This sample has the largest clusters and strongest matrix Re depletion making it easiest to visualise. Figure 3.2.1a) shows 4nm thick sections through an atom map of the W-2Re sample following 33dpa irradiation at 773K. The outer surface of the alloy is marked by the carbon layer visible on the left hand side of the map, below which a region of approximately 200nm has prominent clustering of Re atoms. At greater depths, the structure returns to being a homogeneous solid solution. Figure 3.2.1b) shows the calculated average cluster diameter and volume fraction determined within 10nm thick bins of the dataset. The cluster volume fraction profile strongly correlates with the damage profile from the SRIM calculation for tungsten at 33dpa.

3.2.2 Effect of Dose and Nominal Re Content on Cluster Formation

Atom maps of irradiated tungsten 2, 5, 10 and 25at.% Re alloys after being exposed to doses: 1.2, 3.9 or 33dpa are shown in Figure 3.2.2. These atom maps show only Re atoms and are sliced at different thicknesses: 4, 2, 1 and 0.5nm, to illustrate the differing segregation extents (clustering) more clearly. To quantify cluster characteristics, Re composition, size, number density and volume fraction were averaged and are tabulated in Table 1a-c). Two different methods of measuring cluster size were used. The W-25Re alloy at 33dpa featured spherical and rod shaped clusters (§3.2.3). The length of rod shaped clusters is measured via a Pythagorean relation detailed §2.3.2. The same method is also used to measure the spherical clusters, which along with rod clusters are all reported as length in Table1c). Clusters in all other alloys and irradiation conditions were approximately

spherical (justified in §3.2.2) and their diameters were measured along the z-axis, which was accurately calibrated to match the <110> lattice spacing.

The cluster presence appears to increase with dose between 1.2-33dpa for all W-Re alloys considered here. At 1.2dpa, the clusters across all alloys are faintly visible; they have very small diameters (within 1-4nm range) and appear rather sparse. As the dose was increased to 3.9dpa, the cluster volume fraction increased slightly. Table 3.2.1a-b) shows the volume fraction of W-25Re sample measured 0.55% at 3.9dpa, a small increase compared to 0.41% for its 1.2dpa condition. Also, there is minimal change in cluster composition for the alloys between the two doses.

At the highest dose: 33dpa, the cluster presence is significantly greater than at lower doses of 1.2 and 3.9dpa. In Figure 3.2.2, the clusters in W-Re alloys at 33dpa are large, averaged at ~6nm diameter/length and maximal diameter/length ~15nm. There is also a greater volume fraction of clusters at 33dpa ranging from 6-11%, compared to the 0.6-7% volume fraction range for 3.9dpa dose. The higher dose also brought about a higher degree of Re enrichment. Across all alloys at 33dpa, the cluster composition consistently increased by 6-8at.% Re relative to 3.9dpa condition. It is also associated with strong depletion of Re within the matrix as evident visually and in Table 3.2.1c). Despite the strong Re segregation oberserved at 33dpa at 773K, the bulk composition within the irradiated region remains unchanged as shown in Table 3.2.1c).

Another factor affecting cluster behaviour is the bulk Re content. At 1.2 and 3.9dpa, both cluster diameter and volume fraction progressively decrease for increased bulk Re contents. The trend is most evident when comparing between the lowest and highest Re content alloys. In W-2Re alloy irradiated to 3.9dpa, the average cluster

diameter is 5.5nm, 5 times greater than the cluster diameter in the W-25Re alloy (1.6nm). Also at 3.9dpa, there is an order of magnitude difference in cluster volume fraction between W-2Re; 7.23% compared to W-25Re; 0.55%.

However, the cluster Re composition, if considered as a ratio of the bulk composition remained relatively consistent as bulk content increased. The W-2Re, W-5Re, W-10Re and W-25Re samples irradiated to 1.2-3.9dpa have cluster composition in the ranges: 5.2-5.7, 13.3-15.1, 21.0-21.8 and 41.6-46.0at.% Re respectively. Relative to respective bulk Re contents, this gives an enrichment factor that is in the range of 2-3. Thus bulk Re content has minimal effect on cluster enrichment at 1.2 and 3.9dpa.

At 33dpa, many of these lower-dose trends regarding effect of bulk composition change. As Table 3.2.1 shows, the cluster number density at 33dpa progressively increases with Re composition. The W-25Re had the highest density ($2.94x10^{6}$clusters/μm^{3}) 3.5 times increase compared to W-2Re sample ($8.12x10^{5}$clusters/μm^{3}). The degree of Re enrichment at 33dpa decreases with bulk Re content. For the W-2Re alloy, the cluster composition is 6 times the bulk composition. It is much higher than for clusters in W-25Re whose composition is 2 times the bulk.

a)

Averages Grain Size	1.2 dpa 773K W2Re 1-3mm	1.2 dpa 773K W5Re 1-3mm	1.2 dpa 773K W10Re 1-3mm	1.2 dpa 773K W25Re 1-3mm
Re (at. %)	5.2 ± 1.5	13.3 ± 2.1	21.8 ± 3.2	46.0 ± 5.2
Diameter (nm)	4.2 ± 1.7	2.3 ± 0.8	1.7 ± 0.5	1.6 ± 0.7
Number Density (x1000 μm^{-3})	907 ± 56	545 ± 39	523 ± 49	663 ± 46
Volume Fraction (%)	4 ± 0.24	0.7 ± 0.05	0.33 ± 0.03	0.41 ± 0.03

b)

Averages Grain Size	3.9 dpa 773K W2Re 1-3mm	3.9 dpa 773K W5Re 1-3mm	3.9 dpa 773K W10Re 1-3mm	3.9 dpa 773K W25Re 1-3mm
Re (at. %)	5.7 ± 1.4	15.1 ± 2.3	21.0 ± 3.1	41.6 ± 5.9
Diameter (nm)	5.5 ± 2.5	2.6 ± 1.1	2.1 ± 0.8	1.6 ± 0.5
Number Density (x1000 μm^{-3})	817 ± 61	816 ± 66	944 ± 61	598 ± 51
Volume Fraction (%)	7.23 ± 0.54	1.18 ± 0.10	0.85 ± 0.06	0.55 ± 0.05

c)

Averages Grain Size	33 dpa 773 K W2Re 1-3mm	33 dpa 773 K W5Re 1-3mm	33 dpa 773 K W10Re 1-3mm	33 dpa 773 K W25Re 1-3mm
Cluster Re (at.%)	12.8 ± 2.9	19.1 ± 4.0	28.4 ± 5.1	53.4 ± 5.3
Matrix Re (at.%)	1.2 ± 0.1	3.2 ± 0.5	8.6 ± 1.3	22.9 ± 0.5
Bulk Re (at.%)	2.3 ± 2.9	4.9 ± 4.0	9.8 ± 5.1	25.0 ± 5.3
Diameter/Length (nm)	6.6 ± 3.8	5.3 ± 3.4	5.0 ± 4.3	5.1 ± 3.6
Number Density (x1000 μm^{-3})	812 ± 54	1010 ± 51	1892 ± 105	2942 ± 121
Volume Fraction (%)	11.21 ± 0.74	10.43 ± 0.53	5.95 ± 0.33	6.82 ± 0.28

Table 3.2.1 Averaged cluster Re content, diameter, number density and volume fraction for W 2, 5, 10 and 25at.% Re alloys at a) 1.2, b) 3.9 and c) 33.0dpa.

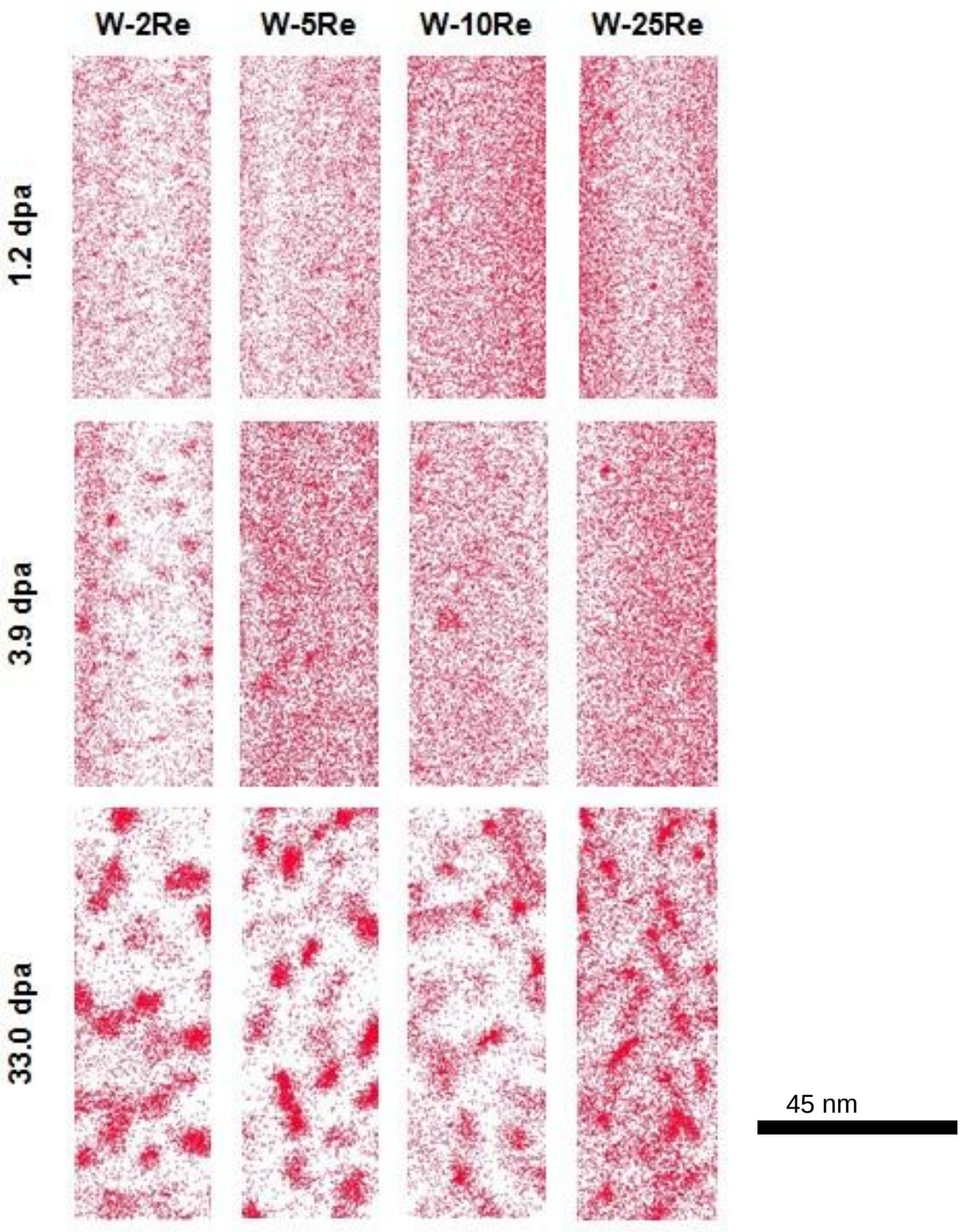

Figure 3.2.2 Atom map slices showing only Re atoms taken from reconstructions of tungsten 2, 5, 10 and 25 at.% Re alloys irradiated to a dose of 1.2, 3.9 and 33.0dpa all

at constant irradiation temperature of 773K. Slices range in thickness between a range of 4-0.5nm with increasing Re contents in order to show cluster presence clearly.

3.2.3 Structural Analysis of Clusters: W-2Re, W-5Re and W-10Re

Typical clusters within 33dpa 773K, W-2Re, W-5Re, W-10Re and W-25Re alloys imaged along the <110> pole are presented in Figure 4.2.2a-d). The atom maps show a 4nm thick slice and the red, Re atoms are given a larger pixel radius to stand out from the black, W matrix atoms. The clusters in all figures are aligned with the <110> plane suggesting them to be coherent. Sigma and Chi precipitates have complex incoherent structures (§ 1.3.4) and would not be aligned with the <110> plane. This lattice analysis technique has been previously used to identify coherency and lattice segregations in alternate material systems [127-129]. The studies found precipitate coherency can be imaged where solute and matrix elements have similar evaporation fields just like W and Re atoms.

a)

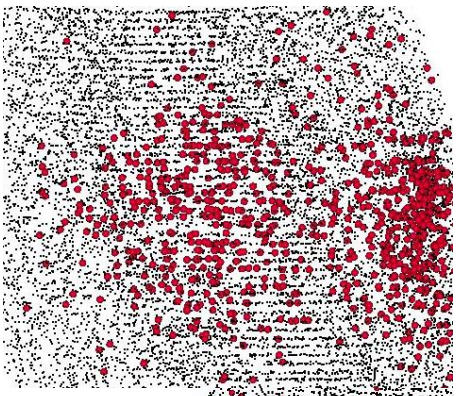

b)

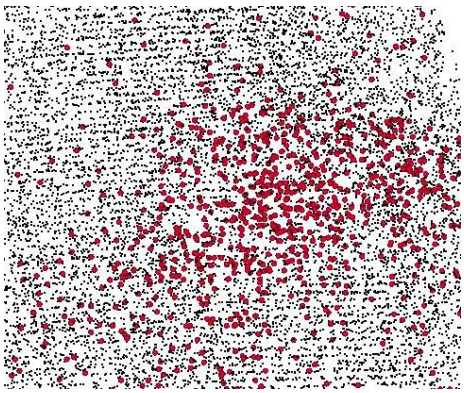

c)

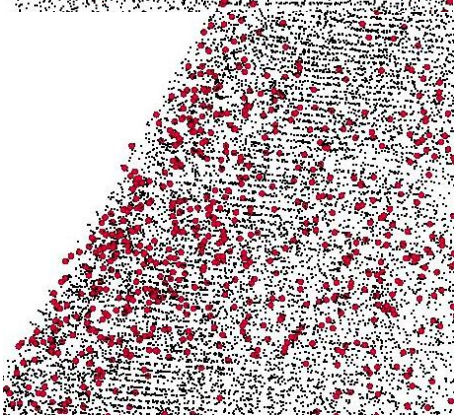

Figure 3.2.3 Atom maps, 2 nm thick, of Re (red) cluster in W (black) matrix imaged on the <110> pole for a) W-2Re, b) W-5Re and c) W-10Re alloys.

Figure 3.2.4 shows the aspect ratios of clusters in W-2Re, W-5Re and W-10Re irradiated at 33dpa at 773K. Each plot is representative of all clusters within a single reconstruction at 0-150nm depth (150-350 clusters in each case). The aspect ratios are calculated using the “precipitate analysis” algorithm in IVAS 3.6.6 approximates clusters as ellipsoids. Aspect ratio is taken as (major axis length) / (minor axis length). Nabarro et al [126] suggested that clusters having a aspect ratio greater than 2 should be classified as rod shapes. Based on this definition, 90% of clusters in Figure 3.2.4 lie below this critical value and can be classified as spheres. It is thus reasonable to approximate all clusters as spheres in measuring their diameter.

The clusters at 33dpa have strongest presence and are most likely to adopt particular shapes or lattice structures compared to 1.2 and 3.9 dpa. However, I found them to be coherent and spherical. As a result, analysis of the clusters formed at the lower doses was not undertaken.

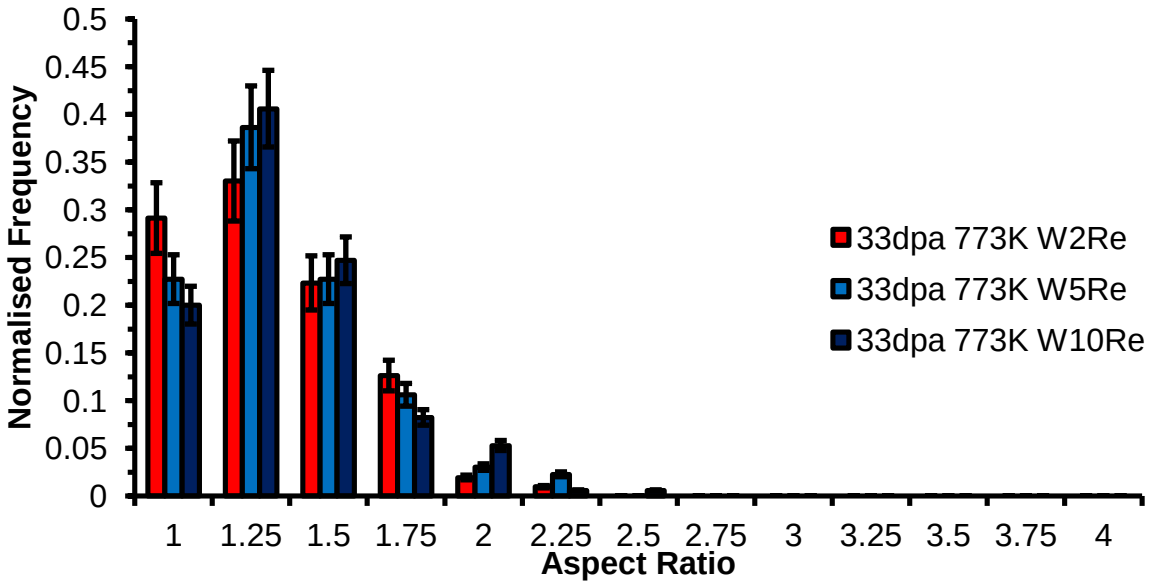

Figure 3.2.4 Normalised cluster aspect ratio distribution plot for W-2Re, W-5Re and W-10Re alloy irradiated to 33dpa at 773K.

3.2.4 Structural Analysis of Clusters: W-25Re

Clusters in W-25Re irradiated to 33dpa are imaged along the <110> pole in Figure 3.2.5a-c). Figure 3.2.5a) show W (black) and Re (red) atoms sliced at 4nm from the reconstruction. The higher Re solute content in the W-25Re alloy makes it difficult to see clusters so, an atom map containing just the Re atoms is shown in Figure 3.2.5b). Re concentration contour plot is displayed in Figure 3.2.5c). There are spherical and rod shaped clusters present according to the 50at.% Re enrichment regions in Figure 3.2.5c). The corresponding atom maps show all atoms within both clusters appear aligned with the lattice planes. Therefore, clusters within W-25Re alloy irradiated to the highest dose, 33dpa are most likely coherent.

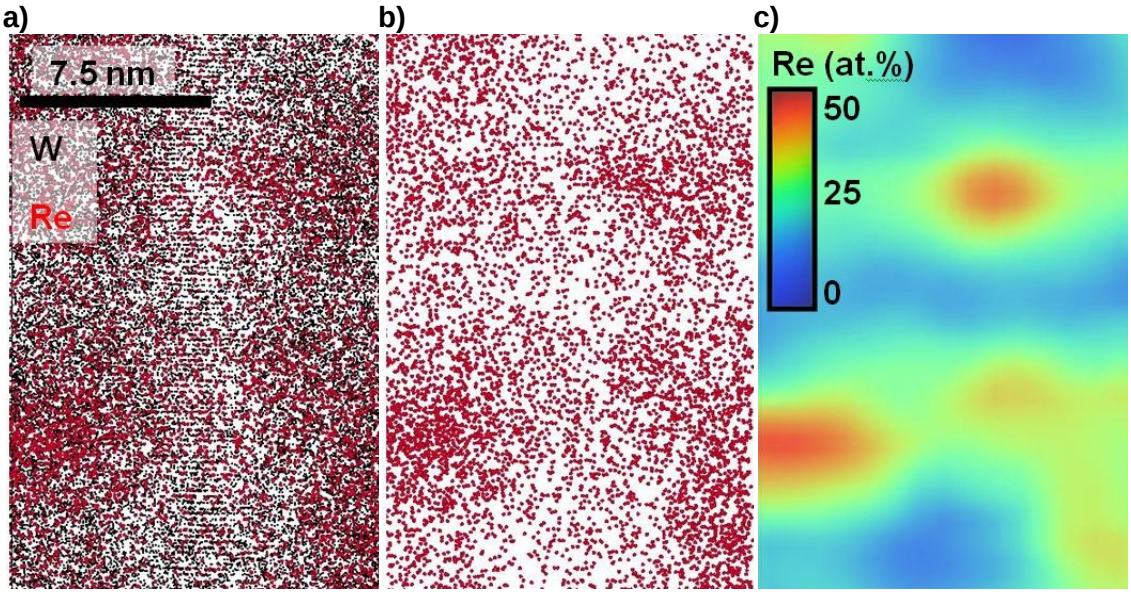

Figure 3.2.5 W-25Re sample irradiated to 33dpa 773K: a) Atom map showing W and Re samples. b) The same atom map showing only Re atoms a) Concentration contour plot of Re concentration.

Normalised aspect ratio distribution of clusters in W-25Re alloy at 33dpa 773K is plotted in Figure 3.2.6a). The distribution profile for W-2Re at 33dpa 773K (Figure 3.2.4) is included for comparison. Unlike the W-2Re alloy, the cluster distribution of the W-25Re is shifted strongly to the right. Approximately ~ 50% of clusters have an aspect ratio greater than 2 which defines them as being rod shaped [126] while the rest are spherical.

Figure 3.2.6b) plots the cluster aspect ratio against their length. A linear relation was assumed and there is a correlation present. The data suggests spherical clusters are associated with small lengths <4nm while above 4nm, rod shaped clusters occur. The composition of clusters is plotted against their length in Figure 3.2.6c). The measured composition appear not to be correlated with cluster size as it is consistently at 53at.% Re.

The rod clusters in 25at.% Re alloy are analysed for orientation dependency. Figure 3.2.7a-b) show such clusters as identified with 35at.% iso-surfaces. The iso-surface composition is chosen to be the average of measured cluster composition and matrix composition. At this iso-surface value, the number of clusters identified and their length approaches the values as determined via d-max method in Table 3.2.1. In figure 3.2.7a), the rod clusters are viewed from the top as 10mm thick slices through the atom maps and also from the side as 20nm thick slices. The orientation of the clusters is compared with the crystallographic orientations derived from the atomic density plot shown in the same figure [112]. All rod clusters appear to be aligned with the <110> direction. This is further verified by a 90^{o} rotation in Figure 3.2.7b), where all the rod clusters still appear aligned with <110>.

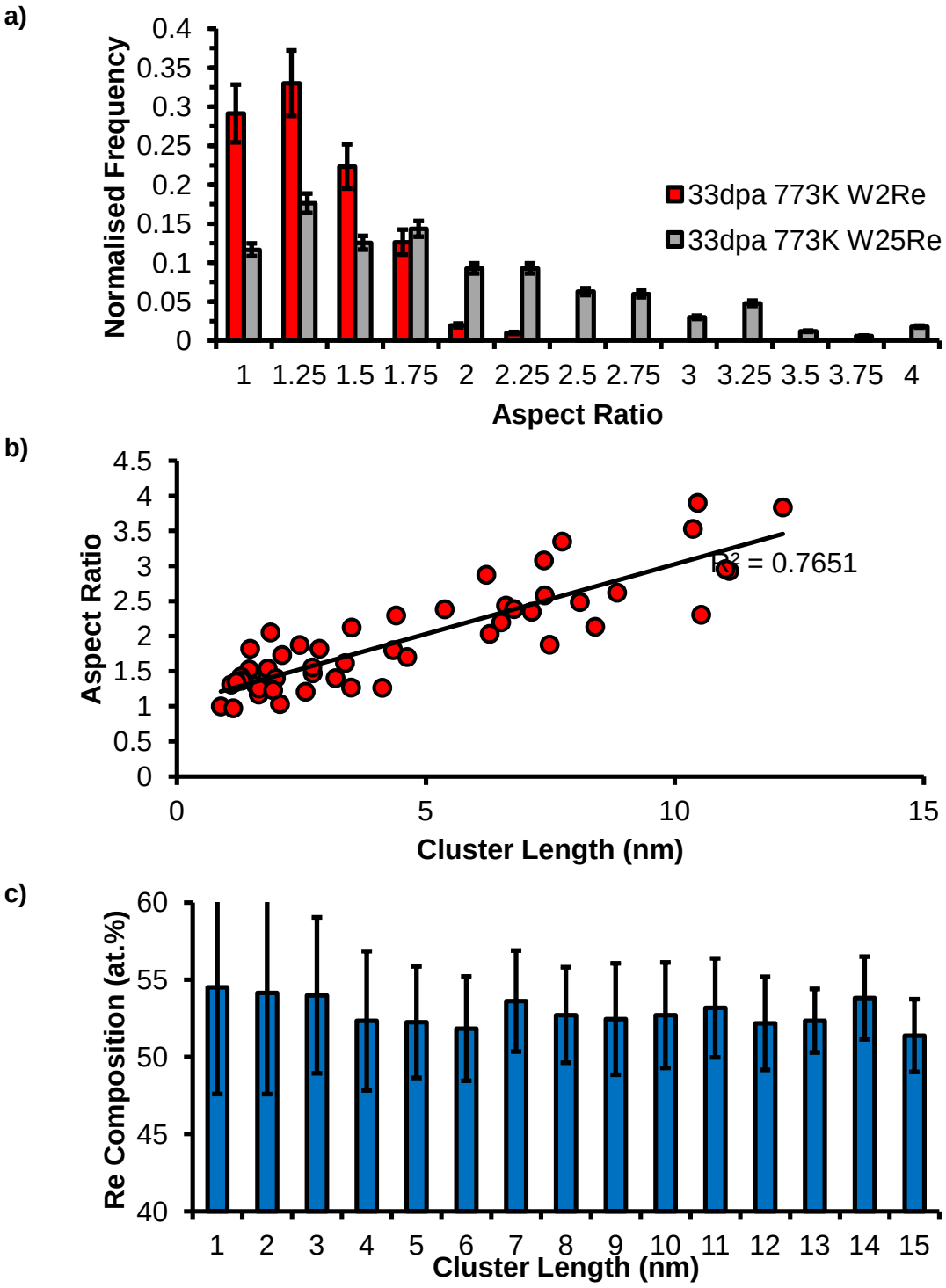

Figure 3.2.6 a) Aspect ratio distribution plot for clusters in W-25Re irradiated to 33dpa 773K. The distribution plot for W-2Re at same irradiation condition is shown for comparison. Cluster length in W-25Re 33dpa 773K plotted against b) aspect ratio and c) Re composition (at.%).

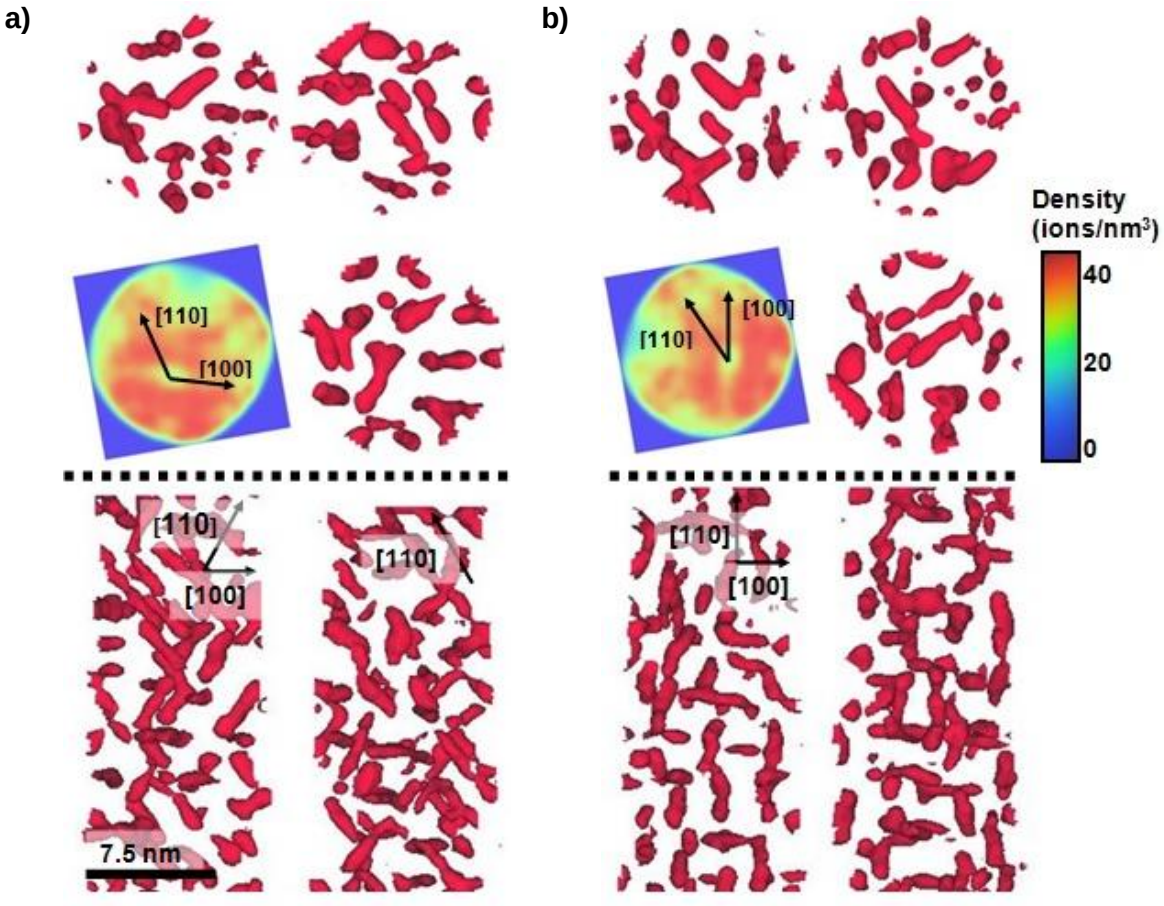

Figure 3.2.7 W-25Re irradiated to 33dpa 773K: a) Re iso-surfaces and atomic density contour taken at 35at.% Re. The cluster images after a 90^{o} rotation is shown on the right side of the black line separating the two. b) The same cluster iso-surface after a 90^{o} rotation.

3.2.5 Nucleation and Growth: Cluster Size Distribution

Cluster size distribution plots are generated from the cluster diameters and they offer detailed analysis of cluster nucleation and growth mechanics. All the cluster diameters for a sample are accumulated together and a normalised size distribution is created from the data set. The diameters are categorised into 0.5nm intervals for 0-15nm range. The values in normalised size distribution plot are all multiplied by

the cluster number density to obtain the cluster size distribution expected within a hypothetical volume. The margin of error at each point is estimated by multiplying the value by confidence level at 99% which is 1.29 divided by square root of total clusters counted.

In Figure 3.2.8a-b) and Figure 3.2.9a-b), the cluster size distribution for each alloy is plotted at doses 1.2, 3.9 and 33.0dpa at 773K. The plots show cluster number densities at different diameters within 1 μm^3 volume. All plots feature a sharp drop in cluster count at 1.5nm diameter/length brought about by the Nmin cut off value of 20 used for cluster analysis (§2.3).

It is important to note the 33dpa W-25Re distribution profile is the only plot where the cluster sizes are reported in length rather than diameter. However, in §3.2.3, it is apparent rod shaped clusters are in co-existence with spherical clusters for this dose and sample. It is still accurate to report the spherical clusters as length because they measure the same regardless of whether the Pythagorean relation or Z-axis extent method is used (detailed in §2.3.2).

Between 1.2 and 3.9dpa, the distribution shape for all alloys remains broadly similar with the exception of the W-2Re alloy. In Figure 3.2.8b) and 3.2.9c-d), the peak shapes are all narrow, only the peak height increase by 20-50%. The opposite trend is apparent for the 2at.% Re alloy. At 3.9dpa, the distribution profile has broadened, the FWHM is 3.5nm higher than the 1.2dpa condition, 2.3nm. Also, the peak height dropped twofold between 1.2 and 3.9dpa, from $1.8x10^5$ to $9x10^4$clusters/μm^3.

At 33 dpa, there is a divergence in the size distribution profiles between 2-5 and 10-25at.% Re samples. The W-2Re and W-5Re alloys feature bimodal distribution having a broad peak at 7.5nm diameter and a narrow peak at 2.5nm. Compared to

their 1.2dpa distribution profiles, the range in cluster size of both increased twofold from 7.5nm to 15nm. As well the peak height has dropped by more than 50% for both samples.

On the other hand, the W-10Re and W-25Re size distribution profiles presented in Figure 3.2.9a-b) feature only a singular peak positioned at 2.5nm. The tailing of the profile at 33dpa has broadened to 15nm from 7.5nm diameter. Also, the peak height has increased by 100% for either alloy relative to the 1.2dpa condition.

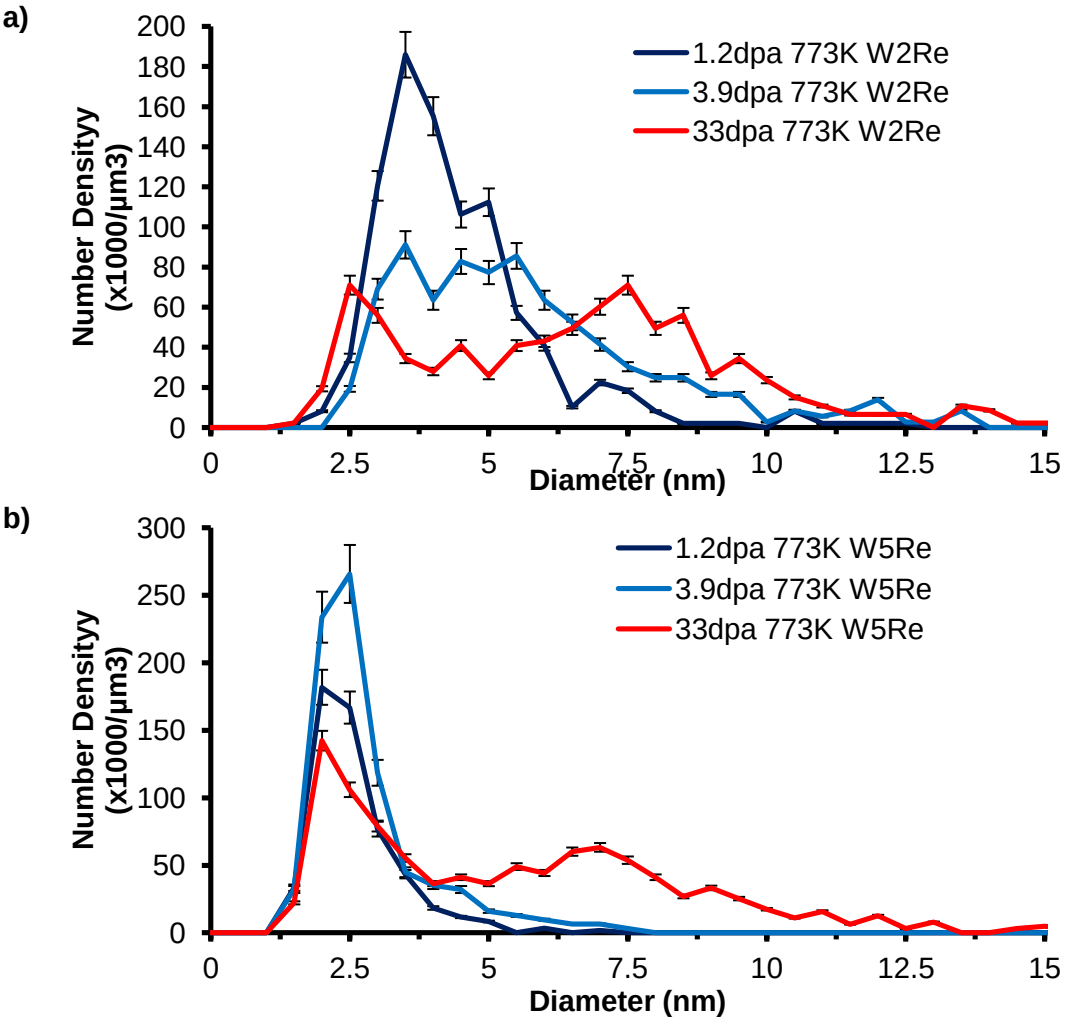

Figure 3.2.8 Number density normalised cluster size distributions under 1.2, 3.9 and 33dpa self-ion irradiation at 773K for a) W-2Re and b) W-5Re alloys.

a)

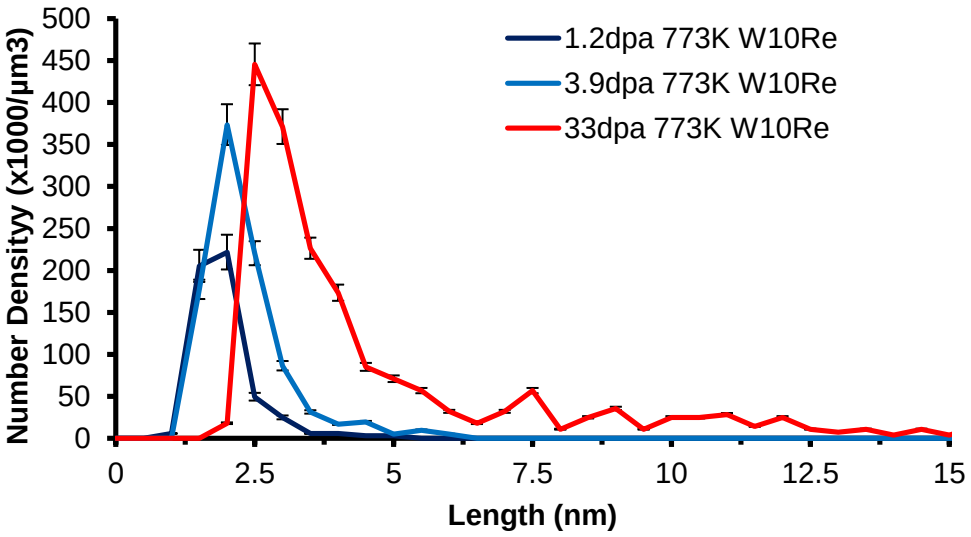

b)

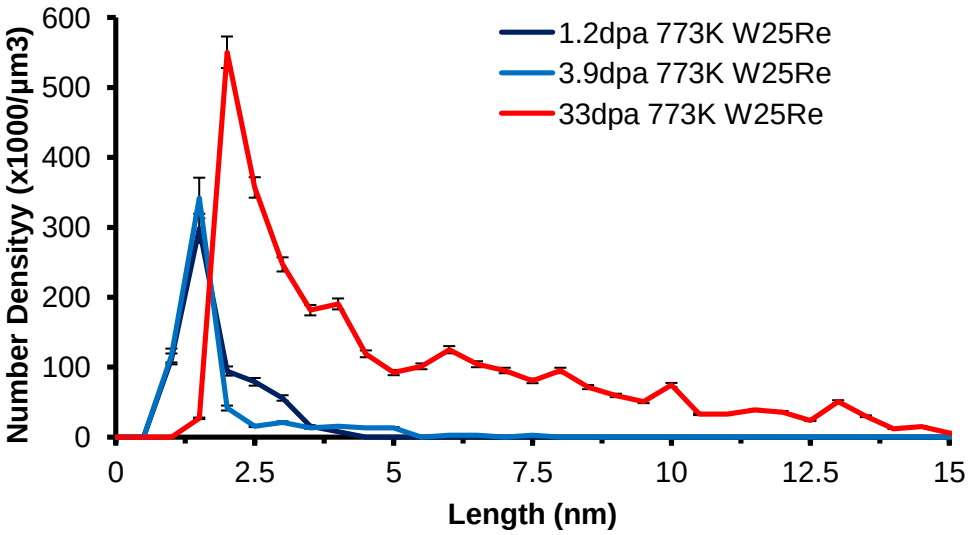

Figure 3.2.9 Number density normalised cluster size distributions under 1.2, 3.9 and 33dpa self-ion irradiation at 773K for a) W-10Re and b) W-25Re alloys.

3.3 Discussion of Cluster Evolution With Dose

3.3.1 Effect of Dose of Cluster Formation

The size distribution profiles in Figure 3.2.8a-b) and 3.2.9a-b) show cluster growth occurs as dose increases but it is also accompanied by continuous nucleation of smaller sized clusters. For the W-2Re and W-5Re alloys, this is demonstrated by the change in the shape of the size distributions, where a single peak is observed at 1.2 and 3.9dpa but two peaks are seen at 33dpa. The large peak represents clusters that have grown in size while the small narrow peak positioned at 1-2nm represent small clusters newly formed. For the W-10Re and W-25Re alloys, the peak height at 33dpa increased two fold by $2.5x10^5$clusters/μm^3 compared to 1.2dpa condition. The position of the peaks didn't change remaining at the same range of 1-2nm diameters although the tail of the size distributions increased twofold from 7 to 15nm.

The trends observed here suggest there is an underlying mechanism involved. It is likely a result of some clusters being dissolved by irradiation and the solute atoms then re-nucleating as clusters. The mechanism of radiation-induced dissolution of precipitates and the re-precipitation of fine sub-particles has been studied analytically, for example by Frost and Russell [130] and later by Heinig et al. [131], who also used Kinetic Monte Carlo Methods. This mechanism is predicted to lead to a double peak in the particle size distribution under certain conditions. Experimentally, duplex distributions of coarse and fine precipitates have been observed previously, for example by Heinig et. al. during the ion irradiation of gold particles in silica [131], and by Monnet et al. in ion irradiated oxide dispersion strengthened ferritic steels [132].

3.3.2 A Hypothesis for Cluster Evolution

In this study, the evolution of clusters was observed, transforming from faint, small, round clusters into large and distinct clusters either sphere or rod-like in shape. Combined with available tungsten experimental and modelling data in literature, we can now present a hypothesis on how Re segregates under irradiation.

I believe that clusters nucleate via segregation of Re solutes to vacancy clusters created in the aftermath of radiation damage. It is possible there are other interstitial based nucleation paths but we concern ourselves with only a vacancy driven one. This is because the irradiation temperature: 773K, is one where monovacancies are mobile [113].

There are three pieces of supporting literature. Firstly, the existence of vacancy clusters also known as nano-voids has been detected by Field Ion Microscopy in ion-irradiated tungsten by Seidman et al [81], and also indirectly proven via Positron Annihilation Spectroscopy [133-135]. However, where Re is present, nano-void formation is severely reduced. This was noted in TEM analysis of neutron irradiated W-Re alloys by Tanno et al. [46, 80, 136]. At 1.54dpa 1023K, the void volume fraction in W-10Re is 0.0066 %, two orders of magnitude smaller than that in W, 0.65%. Re suppresses void formation, a notion supported further Kong et al [60]. Through DFT modelling, Re was found to have a positive binding energy with vacancies at 0.2eV, indicating Re has an affinity for vacancies. The mechanism seems to be that vacancy clusters created during irradiation have a tendency to develop into voids but their development is hindered by Re solutes which are attracted to the vacancies / vacancy clusters.

In the atom probe data presented here, this hypothesis is further reinforced by the trends regarding effect of bulk Re content on cluster behaviour. At 33dpa 773K, the cluster number density has increased fourfold between 2 and 25at.% Re alloys ($8.12x10^5$ to $2.94x10^6$clusters/μm^3), a trend also observed in literature data [46, 80]. If Re segregates to vacancy clusters, then the abundance of Re in the W-25Re alloy leads to a higher probability for each vacancy cluster formed to nucleate a solute cluster as compared to the W-2Re alloy.

Also, size distribution plots in Figure 3.2.8a-b) and 3.2.9a-b) consistently feature a peak at 2.5nm representative of newly formed clusters. This value matches measurements of nano-voids in tungsten. For tungsten neutron irradiated to 0.96dpa at 811K (similar temperatures), the average void diameter are 2.1nm [80]. Atomic resolution imaging of voids by Seidman et al measured 2.4nm diameter for ion-irradiated tungsten [82]. The similarity in size supports the notion of voids being a nucleation point for clusters. Previously, I stated cluster sizes smaller than 1.5nm diameter were discarded. The cut-off value is below the peak position, so the peaks are valid and not an artefact.

Still, more experimental work is needed to support this idea of clusters nucleating from voids. Further DFT and Monte Carlo simulations is required to justify it from a large-scale thermodynamic stand point. Field Ion Microscopy analysis offers a 100 % resolution of all atoms within a cluster and can be another avenue for future investigation.

3.3.3 Formation of Sphere and Rod shaped clusters.

Through measuring the aspect ratios of clusters formed in W-2Re, W-5Re and W-10Re alloys at 33dpa, at least 90% of clusters formed are spherical [126]. In the W-25Re alloy, two cluster shapes exist: spherical and rod shaped clusters. The aspect ratio distribution in Figure 3.2.6a) show these two cluster shapes occur in equal amounts. The spherical clusters are small while the rod clusters are large, although, there is no composition correlation with the aspect ratio.

The rod shaped Re clusters within the W-25Re alloy seen in atom maps in Figure 3.2.1 closely resemble the needle precipitates observed by Tanno et al [46]. Their shapes are similar and both clusters and precipitates orient along <110> direction. It is a possibility that the rod clusters develop from the spherical shaped clusters. The transition from spheres to rods is unknown and further investigation is needed.

3.3.4 Nanoindentation Measurements And Links With Clustering

Hardness data of the irradiated alloys was obtained by Dave Armstrong and Christian Beck and plotted in Figure 3.3.1. Between 0 and 1.2dpa, the hardness increases by 0.5-1GPa across all alloys. But, between 1.2 and 3.9dpa, the irradiation hardening is indiscernible as the error bars strongly overlap each other. It is difficult to say whether it has increased or plateaued. Between 3.9 and 33dpa, the largest increase in hardness is observed with dose, increasing by ~2-3GPa consistently for all alloys.

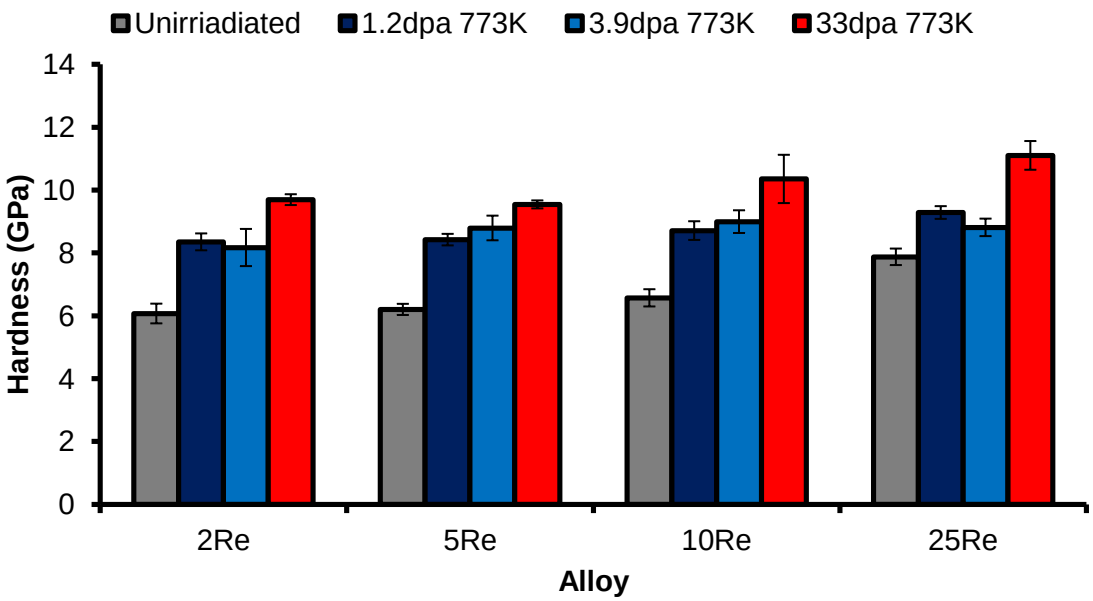

Figure 3.3.1 Hardness of W-2Re, W-5Re, W-10Re and W-25Re samples measured in unirradiated and after irradiation to 1.2, 3.9 and 33 dpa at 773 K. Data provided courtesy of Dave Armstrong and Christian Beck (Private Communications).

It is possible W-Re alloys go through two phases of hardening: dislocation formation followed, by clustering. Dislocation hardening occurs between 0 and 3.9dpa for all alloys studied here. In Figure 3.3.1, there is a sharp rise in hardness between 0 and 1.2dpa. From 1.2 to 3.9dpa either negligible or no hardening takes place despite a further dose of 2.7dpa and increase in cluster diameter and volume fraction reported in Table 3.2.1. In the literature, TEM quantification of dislocation loops in W-5Re alloy irradiated to 3.6dpa 773K (similar conditions), noted a saturation of loop density [74, 75]. The hardening behaviour matches the dislocation loop formation rather than clustering behaviour. So whilst both dislocations and clustering have a hardening effect, dislocation hardening is more dominant at doses to 3.9dpa.

Beyond 3.9dpa, cluster hardening takes place. All W-Re samples measured a hardening of ~2GPa at 33dpa which is correlated with a significant increase in

cluster volume fraction. A typical example would be the W-25Re sample, whose cluster Re volume fraction of 0.55% at 3.9dpa increased by an order of magnitude by 33dpa to 6.82 %. It is unlikely dislocations contribute to this hardness increase as W-25Re alloy dislocation density has saturated by 3.9dpa. In fact, a pure tungsten self-ion irradiated to 33dpa 573K, which is absent of clusters, exhibits a hardening plateau beyond 1.2dpa [11]. Thus, cluster hardening overtakes the dislocation hardening at 3.9dpa and becomes dominant by 33 dpa.

3.4 Summary

Through comparing the atom probe results exploring the effects of dose and Re content on the irradiation response along with experimental and modelling data in the literature, we are able to arrive at the following conclusions:

- Re clusters evolve under increasing damage range, becoming more enriched and greater in volume fraction. However, the nominal Re content has a huge effect on how clusters develop. In the W-2Re alloy, the clusters are spherical and have a significantly smaller number density than the W-25Re alloy whose clusters are mix of spherical and rod shapes.
- The rod shaped clusters present in the W–25Re alloy are found to be preferentially oriented along the <110> direction, closely mirroring needle shaped precipitates seen in neutron irradiation studies. Also the rod shaped clusters are in coexistence with spherical shaped clusters.
- I suggest based on our data that Re clusters nucleate from vacancy clusters created in the aftermath of a displacement cascade. This hypothesis is derived from literature findings involving experimental and computer modelling results and is fully consistent with the atom probe trends as reported in this thesis.
- The measured irradiation hardness of the W-Re alloys demonstrated two stages of hardening with each stage having much stronger hardening effect the former. The two stages are dislocation and cluster hardening.

4. Effect of Os and Ta on clustering behaviour in W-Re

4.1 Introduction

This chapter focuses on the effect of the secondary and tertiary transmutation species Os and Ta on cluster behaviour and alloy mechanical properties. Transmutation species are studied as ternary alloys using W-1Re-1Os and W-2Re-1Ta (at.%) and compared against a control W-2Re alloy sample. All samples were lab-manufactured 10mm diameter plates of 1mm thickness (provided by Christian Beck). They were cut and polished in accordance with §2.1.2. The samples were W-ion irradiated at the highest dose in this study: 33 dpa and at two irradiation temperatures: 573 and 773K.

Hardness data presented here for all irradiated and unirradiated samples were measured on the nanoindenter by Dave Armstrong and Christian Beck. They are reproduced in §4.2.5.5 with their permission.

4.2 W-1Re-1Os alloy: Atom Probe Analysis

4.2.1 Clustering in Irradiated W-1Re-1Os Alloys

To compare the effects of different irradiation conditions/alloy compositions on the microstructures, Figure 4.2.1a) and 4.2.1b) show 4nm thick atom maps slices from the W-1Re-1Os sample irradiated to 33dpa at 573 and 773K respectively. Also shown is the reference W-2Re sample irradiated to same conditions in Figure 4.2.1c) and 4.2.1d). For all samples, the analyses are confined to a depth range of

50-200nm below the implanted surface, where the peak dose would correspond to 33dpa (SRIM).

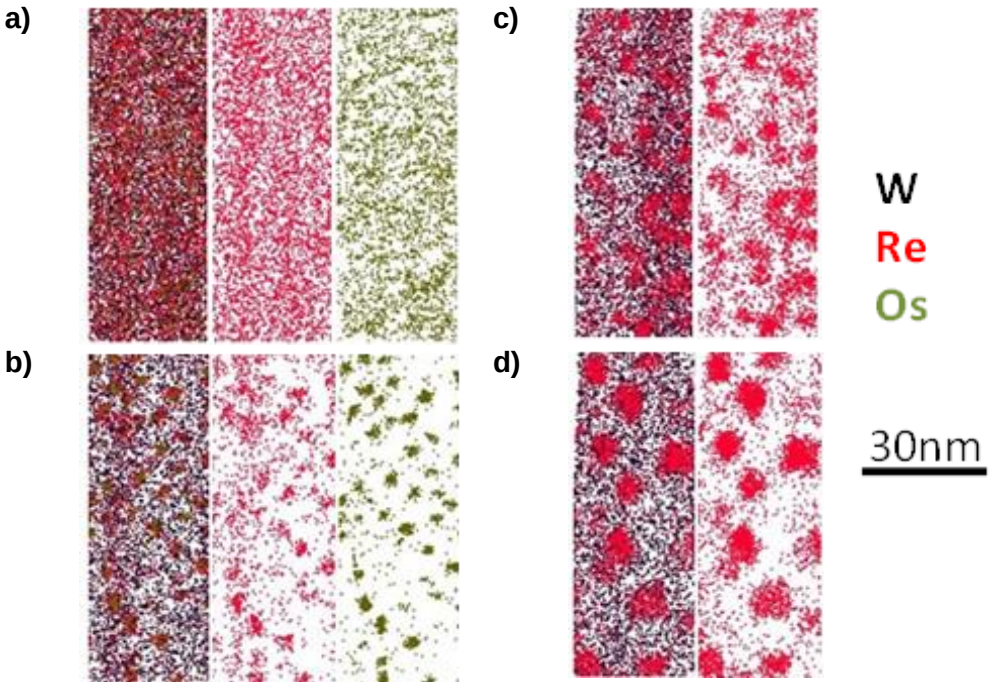

Figure 4.2.1 4nm thick sections from atom maps following 33dpa W-ion irradiation in: a) W-1Re-1Os at 573K, b) W-1Re-1Os at 773K, c) W-2Re at 573K, d) W-2Re at 773K. W, Re and Os atoms are shown in black, red and green respectively.

Visually, Os has significantly altered the clustering behaviour in comparison to the W-2Re binary alloy. At 573K, only slight clustering of Os and Re is evident for the W-1Re-1Os alloy (Figure 4.2.1a), unlike the W-2Re alloy at this condition which features a significant volume fraction of Re-rich clusters ~5 nm in diameter (Figure 4.2.1c). The contrasting clustering between the binary and ternary thus suggests Os is suppressing cluster formation at 573K. However, following the 773K irradiation, a high number density of very small (<4nm dia.) clusters is formed in the W-1Re-1Os alloy, enriched in both Re and Os (Figure 4.2.1b). For the W-2Re sample, the increased temperature yielded a relatively lower number density but larger cluster size, up to 15 nm in diameter (Figure 4.2.1d).

4.2.3 Quantifying W-1Re-1Os Cluster Physical Properties

To quantify the size, chemical composition, density and volume fraction of clusters observed the maximum separation method algorithm (§2.3.1) [112] was used to identify and separate any clusters present in the 50-200nm depth range of each dataset. The reader is asked to refer to §2.3.2 for detailed description of how the identification parameters are found. The mean values for clusters in the W-1Re-1Os alloy are summarised in Table 4.2.1 alongside the corresponding values for the W-2Re alloy. The matrix solute contents are also reported which combined with the cluster composition measures a bulk solute value matching the expected values.

Cluster Feature	573K 33dpa	573K 33dpa	773K 33dpa	773K 33dpa
	W-1Re-1Os	W-2Re	W-1Re-1Os	W-2Re
Cluster Re (at.%)	1.3 ± 0.4	8.0 ± 1.4	1.9 ± 0.9	12.8 ± 2.9
Cluster Os (at.%)	4.1 ± 0.7	n/a	6.9 ± 1.6	n/a
Matrix Re (at.%)	1.1 ± 0.1	1.4 ± 0.1	0.9 ± 0.1	1.2 ± 0.1
Matrix Os (at.%)	0.9 ± 0.1	n/a	0.4 ± 0.2	n/a
Bulk Re (at.%)	1.1 ± 0.4	2.0 ± 1.4	1.0 ± 0.9	2.3 ± 2.9
Bulk Os (at.%)	1.1 ± 0.7	n/a	1.0 ± 1.6	n/a
Radius (nm)	2.8 ± 1.4	2.4 ± 1.0	1.9 ± 0.8	3.3 ± 1.9
Number Density ($10^3/\mu m^3$)	1095 ± 56	1717 ± 72	2467 ± 112	812 ± 54
Volume Fraction (%)	7.3 ± 0..4	9.0 ± 0.4	9.6 ± 0.4	11.2 ± 0.7

Table 4.2.1 Cluster characteristics for both alloys at each irradiation condition used.

At 573K in the ternary alloy, there is no segregation of Re in the clusters; the error bars at 1.3 at.% overlap the bulk value of 1at.%. However Os is enriched four times in excess of the bulk. When Os is absent in the binary alloy, strong segregation of Re into the clusters is apparent; a mean of 8at.%Re compared to a bulk value of 2at.%Re. On raising the irradiation temperature to 773K, the ternary alloy still features relatively little Re segregation to the clusters, while the level of Os rises to

nearly 7at.%. In contrast to the 573K implantation, in the binary alloy implanted at 773K, the Re content is nearly 13at.%. In all cases, solute enrichment is accompanied by a slight depletion of the solutes within the matrix, increasing with temperature as cluster formation becomes more marked, as evident visually in Figure 4.2.1a-d).

There are also differences in the cluster size distributions with irradiation temperature. At 573K, both alloys show similar mean cluster radii, but the number densities and volume fractions are higher in the W-2Re alloy. At 773K, significant changes in the cluster characteristics for both alloys are apparent. In the ternary alloy the size distribution is broader at 773K than at 573K and the number density of the clusters is ~2.5 greater at 773 than at 573K. In W-2Re, the mean size increases to 3.3nm on raising the temperature, while the number density halves compared to 573K. For both alloys, the cluster volume fractions increase slightly with irradiation temperature, with the ternary alloy again displaying a slightly lower volume fraction.

4.2.4 Cluster Development and Enrichment in W-1Re-1Os

Fig. 4.2.2a-b) shows cluster distribution plots for the irradiated W-1Re-1Os and W-2Re alloys, with both irradiation temperatures plotted for each. These figures were each generated from a sample size of at least 500 clusters (in accordance with §3.2.5). The plots show the cluster number density at different radii normalised to a 1 μm^3 volume.

Figure 4.2.2 shows that increasing irradiation temperature broadens the cluster size range for both W-1Re-1Os and W-2Re. However, the distribution profiles are distinctly different in the two alloy types. At 573K (Figure 4.2.2a), the cluster size

distribution in the W-1Re-1Os alloy has a maximum density for clusters at ~2.0nm in radius, corresponding to $1.6x10^5$clusters/μm^3 (calculated by multiplying the total cluster number density (Table 4.2.1) by the cluster frequency fraction for 2.0nm radius). This number density increases threefold when the irradiation temperature is increased to 773K for the ternary alloy, and the peak density occurs for a similar cluster size. For W-2Re, raising the irradiation temperature to 773K appears to produce a bimodal distribution, along with a decrease of peak distribution height by more than a factor of 2 compared to the 573K irradiation.

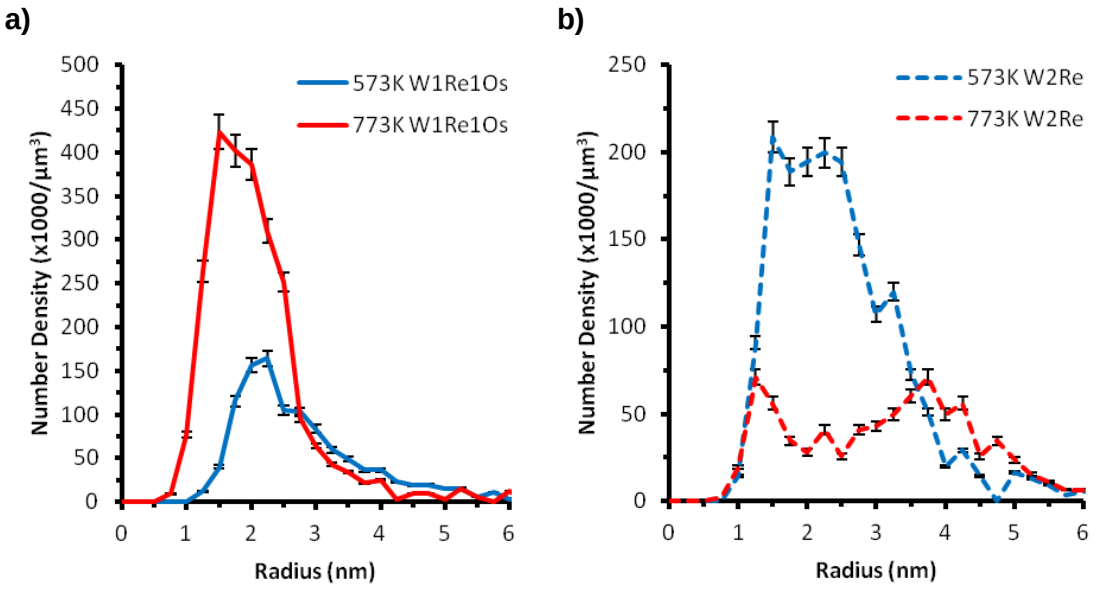

Figure 4.2.2 Cluster size distributions in a) W-1Re-1Os and b) W-2Re following ion irradiation at 33dpa for 573/773K

Proxigram analyses were used to explore the internal chemistry of the clusters as a function of distance from the cores. For each composition and irradiation condition, 10 similarly-sized clusters were isolated using iso-concentration surfaces (set at half the measured cluster compositions reported in the analysis of Table 4.2.1). The Re iso-concentration was used for identifying clusters in the binary alloy whilst the Os Iso-concentration was used for ternary alloy. Averaged proxigrams (from 10

clusters) were then generated for the individual cluster elements, and are shown in Fig. 4.2.3a-b). The “0nm” distance was shifted in the figures to be located at the cluster core. These show clearly that the Os content of the clusters is significantly higher in the cores than near the shells in W-1Re-1Os alloy, particularly so for the alloys irradiated at 773K. The level of Re in the ternary alloy is low as shown in Figure 4.2.3c) and is consistent within errors across the full cluster profile. Likewise in the W-2Re alloy, the cluster chemistry is non-uniform compared to W-1Re-1Os (Os), Re is strongly enriched in the centre of the clusters, most strikingly at 773K.

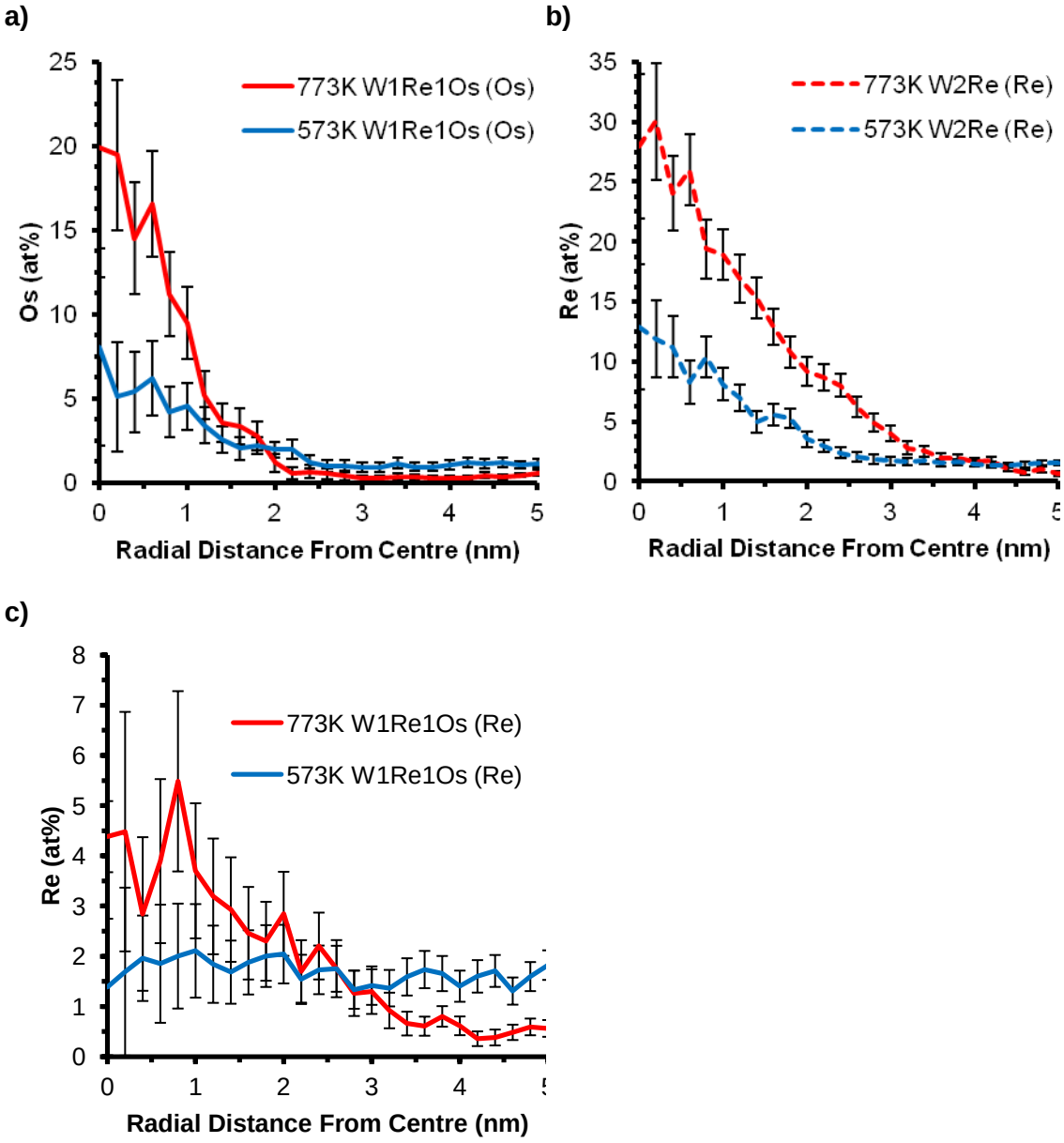

Figure 4.2.3 Proximity histograms through clusters identified in a) W-1Re-1Os and b) W-2Re following ion irradiation at 33dpa for 573/773K.

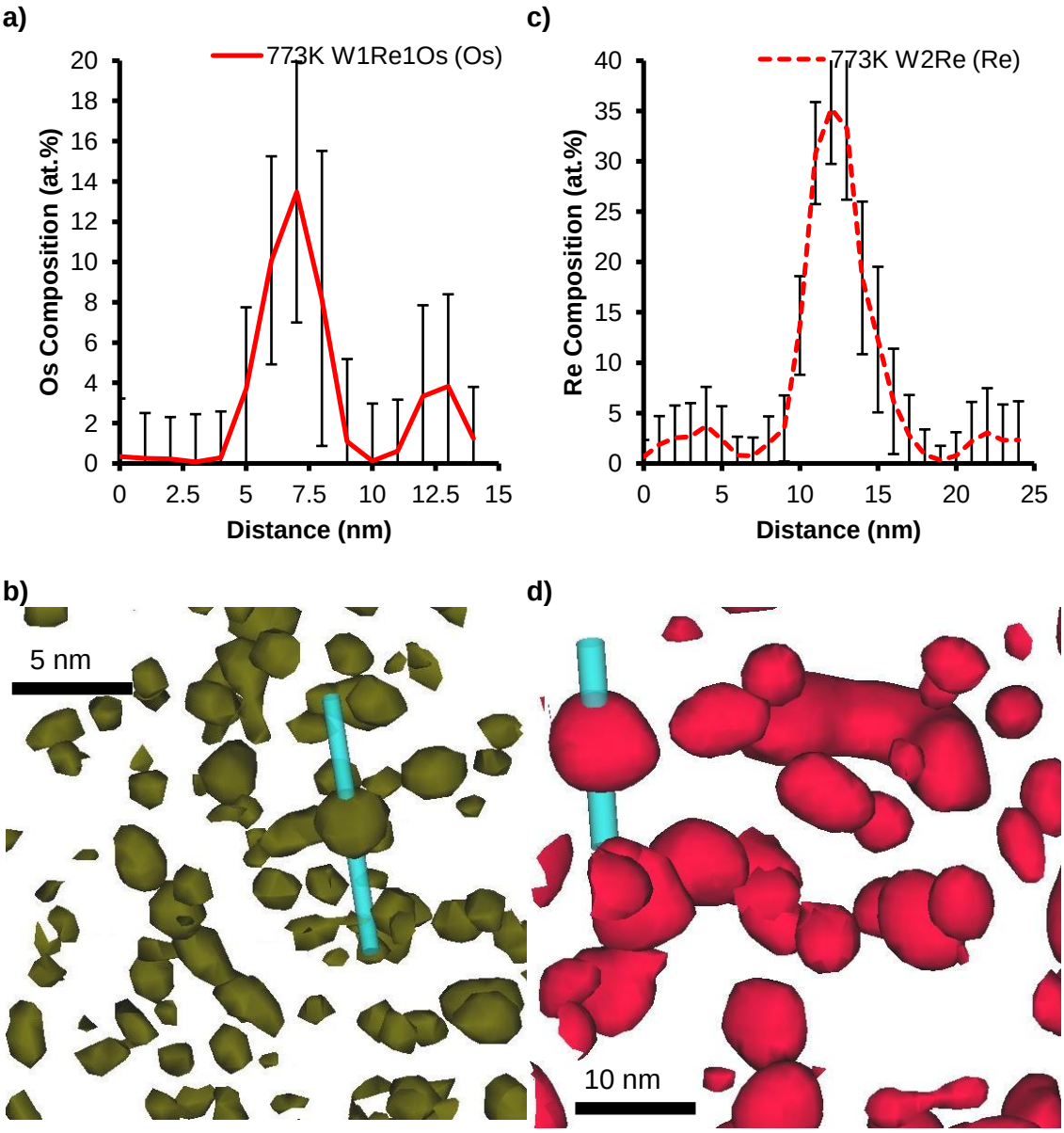

Figure 4.2.4 (a) 1D concentration profile of a typical Os cluster in W-1Re-1Os at 33dpa 773K and corresponding iso-surface map (b) at 4at.% Os. (c) 1D concentration profile of a typical Re cluster in W-2Re at 33dpa 773K and corresponding iso-surface map (d) at 8at.% Re.

The solute composition in the cores of the clusters is much higher than the mean cluster compositions shown in Table 4.2.1, For example, for W-1Re-1Os alloy at 33dpa/773K, the core composition is 30at.%, 2.5 times the mean value of 13at.%. To confirm the highly inhomogeneous solute distributions within the clusters and to verify the maximum enrichment at the very cores, 1D concentration profile analyses were performed on clusters within the W-1Re-1Os (Figure 4.2.4b) and W-2Re alloys (Figure 4.2.4d) at 773K. The iso-surface concentration used was 4 and 8at.% respectively and is the average between the measured cluster composition and bulk composition. As stated in §3.2.4, the choice of the iso-surface values depends on the correspondence with cluster number density and size as reported in Table 4.2.1. In both resulting concentration profiles (Figure 4.2.4a&c), the composition measured at the cluster core matches that of the proxigram measurements.

4.2.5 Discussion: Irradiation of W-1Re-1Os alloy

4.2.5.1 Effect of Os on Cluster Behaviour

Through analysing the chemistry of the clusters, Os preferentially segregates over Re at both irradiation temperatures. Table 4.2.1 shows the Re content of clusters within the W-1Re-1Os sample is between 1.3-2 times that of the bulk value at 573 and 773K. It is unlike the Os content in the clusters which is 4-7 times the bulk value. The Re content within the clusters is definitely reduced as a result of Os, the extent of which can be assessed by comparison with the W-2Re sample. In the W-2Re alloy, the mean Re cluster composition is 8.0at.% Re at 573K and 12.8at.% Re at 773K, significantly higher than seen in the ternary alloy.

Furthermore, Os appears to possess different cluster nucleation and growth rates. At 573K, both W-1Re-1Os and W-2Re samples experienced the same irradiation dose and treatment temperature, but the number density and volume fraction of clusters nucleating in the W-1Re-1Os sample appears significantly lower. At 773K, the clustering behaviour of W-1Re-1Os and W-2Re diverges further. The size distribution plots in Figure 4.2.2a) (W-1Re-1Os alloy) show that the peak height of distribution plots increased threefold with temperature while the breadth of the distributions remained the same. The opposite takes place in the W-2Re alloy; the peak cluster number density decreases twofold between 573 and 773K, while the breadth of the distribution at 773K is also two times greater. Thus, at 573 and 773K, Os clusters have restricted growth and enhanced nucleation instead.

4.2.5.3 Diffusion Interpretation of Os clustering

To explore the kinetics of the clustering in the two alloys, the diffusion coefficients for Os and Re in W have been calculated using the Arrhenius equation with D_0 and activation energies values from [39], which provides values from methods such as the activity of radioactive isotopic solutes diffusing in single crystal tungsten [137]. For Os in W, D_0=0.64 x $10^{-4}m^2s^{-1}$ and E_a=5.58eV; for Re in W, D_0 =4.00 x $10^{-4}m^2s^{-1}$ and E_a=6.18eV [39]. These yield D values of 2.0x$10^{-44}m^2s^{-1}$ (Re) and 2.7x$10^{-41}m^2s^{-1}$ (Os) at 773K. These values indicate that diffusion of either solute would be extremely slow if driven by temperature alone.

The tungsten ion implantation enhances diffusion by the large number of vacancies produced and it could be the reason for the clustering behaviour seen here [38, 56, 138, 139]. The methodology of Lescoat et al. [139] is thus used to calculate the radiation enhanced diffusion coefficient at 33dpa and 773K. It assumes that the

clusters behave as perfect sinks for point defects and uses Arrhenius type mathematical models to calculate the diffusion coefficient. For W-2Re (Re) at 773K it is 4.99 x $10^{-26}m^2s^{-1}$ and 3.69 x $10^{-23}m^2s^{-1}$ for W-1Re-1Os (Os) at 773K, both are 18 orders of magnitude greater than for thermal vacancy mediated diffusion. In addition to the enhancement, note that in both cases Os segregation is favourable from a kinetic standpoint.

4.2.5.4 DFT modelling Interpretation of clustering

DFT modelling offers another perspective on the preferential Os segregation observed. Becquart and Domain [62] used density functional theory to calculate the Re-vacancy and Os-vacancy binding energies as 0.2 and 0.35eV respectively, indicating that vacancies are more attractive to Os. A possible mechanism therefore is that for the binary alloy, Re atoms bind to vacancies and nucleate clusters. This diffusion is likely to be enhanced by local thermal spikes from cascades and the large vacancy population present in both irradiated alloys. In the ternary alloy, Os has a stronger binding energy to vacancies than Re, therefore Os-rich clusters form, while Re cluster formation is competitively suppressed.

Thus far, clustering is considered at 773K where vacancies are mobile [113], whereas at 573K interstitials should largely drive cluster formation in irradiated material, (being below the critical temperature for vacancy activated migration 743K [113]). In the W-2Re alloy, the mechanism of segregation of interstitials has been suggested by Cottrell to involve formation of W-2Re dumbbells. These dumbbells are immobile once formed but attract nearby Re interstitials [65, 66]. This hypothesis was derived by applying DFT calculations to understand platelets seen in FIM studies of a neutron irradiated W-10Re alloy [63]. Such interpretation offers a

possible explanation of Re clustering at 573K but, there is no work on W-Os dumbbells or Os-Re interactions. Further DFT and Monte Carlo work is needed to understand the underlying mechanisms.

4.2.5.5 Irradiation Hardening of W-1Re-1Os

Nanoindentation hardness measurements (taken by Armstrong and Beck) at an indenter penetration of 125nm are reproduced in Figure 4.2.5. At 573K, the W-1Re-1Os and W-2Re alloys increase in hardness by 3.22 and 3.27GPa respectively. Whilst the irradiation hardening of both alloys are similar, the clusters in the W-1Re-1Os alloys were present at a lower number density, 57% lower compared to the W-2Re alloy. This suggests that the Os has a stronger relative hardening effect. Following irradiation at 773K, the hardening response in W-1Re-1Os is greater, with the irradiation causing an increase of 5.39GPa compared with 3.84GPa in W-2Re. The dramatic rise in the cluster number density seen in W-1Re-1Os following 773K irradiation is therefore also mirrored in the most pronounced hardness increase for this alloy.

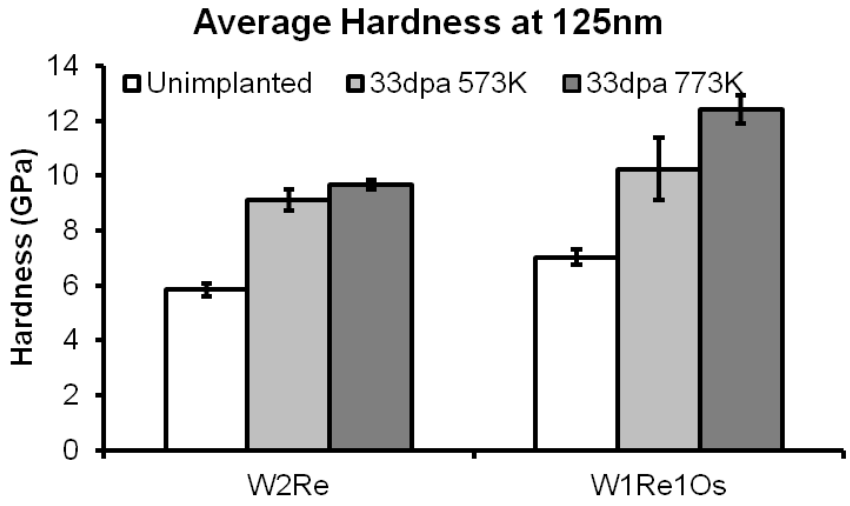

Figure 4.2.5 Nano-hardness measured at 125nm indenter penetration depth for W-2Re and W-1Re-1Os at 573 and 773K (courtesy of Armstrong and Beck)

The Friedel Relation is typically used to test for coherency in clusters within underaged materials [140]. To assess the strength of the clusters in impeding dislocation motion, an Friedel-type hardening mechanism is assumed in which clusters harden the material by acting as local obstacles to dislocations with a strength characterised by a critical breakaway angle ϕ_c [141]. This angle is calculated using the following equation:

$$\Delta\tau_y = \frac{Gb}{\lambda}[\cos(\phi_c)]^{\frac{2}{3}}$$

Where *G* is the shear modulus (161GPa), and *b* is the Burgers vector (0.223nm) [30]. λ is the mean distance between clusters minus their diameter, calculated as $[(\rho)^{-\frac{1}{3}} - d]$, where *ρ* is cluster number density and *d* the mean cluster diameter, both of which are taken from Table 4.2.1. $\Delta\sigma_y$ is the change in uniaxial yield stress, assumed equivalent to one third of the determined hardness values according to reference [142]. The factor 1.73 converts from tensile yield stress to shear yield stress $\Delta\tau_y$ via the Von Mises yield criterion according to reference [142].

	ΔH @ 125nm (GPa)	Δτ [ΔH/5] (GPa)	λ (nm))	$\Phi_{critical}$ (˚)
W-1Re-1Os 773K	5.38	0.90	3.6	78.5
W-1Re-1Os 573K	3.22	0.54	4.2	80.9
W-2Re 773K	3.84	0.64	4.1	79.9
W-2Re 573K	3.26	0.54	3.6	81.7

Table 4.2.2 Calculation of the critical angle dislocations must subtend in order to pass through clusters. (Hardness data courtesy of Armstrong and Beck)

The critical breakaway angle is found to be ~80^o in all alloys in Table 4.2.2. This high value indicates dislocations bend by 10^o in cutting through individual clusters. Such small angles indicate the clusters offer weaker resistance to dislocation motion

compared to incoherent particles whose breakaway angles are below ~50^{o} [143]. Therefore the clusters studied here are weak obstacles to dislocation motion; the considerable hardening observed is a result of their high density and size (and thus small spacing, λ).It appears the critical angle (strength of individual cluster) doesn't change appreciably with cluster size but, having more of them, closely spaced is more effective at hardening.

4.2.5.6 Comparison with Literature Data

There have been no previous reported results for the irradiation response of dilute binary W-2Re or ternary W-1Re-1Os alloys to such damage levels. However Tanno et al. have reported the effect of neutron irradiation to 1.54dpa at 673K and 1024K in W-5Re and W-5Re-3Os alloys, which have comparable Re contents [144, 145]. Although the irradiation conditions were different from the current study, they observed similar precipitate densities (7.3x10^{5}/μm^{3} in W-5Re and 6.7x10^{6}/μm^{3} in W-5Re-3Os) to those observed here. Under neutron irradiation, the presence of Os also appears to promote a greater nucleation rate than in the W-5Re alloy. Additionally, the needle shaped precipitates in the W-5Re-3Os alloy measured 6.8nm length compared to 14nm length for the W-5Re alloy. Os therefore appears to stunt the growth of precipitates in a similar manner to how it stunts the growth of clusters at 773K. Regarding their irradiation hardening the W-5Re-3Os alloy measured an irradiation hardening of 6.67GPa twofold higher than the W-5Re alloy at 3.73GPa. Thus, although this study is based on neutron irradiation and needle-shaped precipitates of needle shape form, the repeatability of the trends are similar to the effect of Os reported here.

4.2.6 Summary

In this chapter, APT and nanohardness measurements have offered fresh insights into the phenomenon of irradiation induced precipitation in W-2Re and W-1Re-1Os alloys. The following major conclusions can be drawn:

- Os has a profound effect on the alloy clustering characteristics, almost completely suppressing the formation of rhenium clusters after irradiation to 33dpa. This is most likely due to Os atoms being more strongly bound than Re atoms to vacancies.
- The higher irradiation temperature, 773K, features a higher cluster number density and composition compared to the lower irradiation temperature 573K for both alloys. The effect is particularly pronounced for the W-1Re-1Os alloy.
- Individual nanoscale clusters produced are relatively weak obstacles to dislocation motion. Their significant contribution to the hardening in both binary and ternary alloys is due to the large volume fraction present.
- The presence of Os in the ternary W-1Re-1Os alloy hardens the material significantly after ion irradiation, compared to the binary W-2Re alloy due to the higher cluster number density. When predicting the mechanical behaviour of tungsten after transmutation in a fusion neutron spectrum all transmutation products must be accounted for. Using binary W-2Re alloys as a reference will substantially underestimate the likely irradiation hardening.

4.3 W-1Re-1Ta alloy: Atom Probe and Nanoindentation Analysis

4.3.1 Comparison with SRIM Predictions

Figure 4.3.1a) shows atom maps from the analysed volume of a W-2Re-1Ta alloy irradiated to 33dpa at 773K. The top atom map shows W only while the middle and bottom atom maps show Re and Ta. The carbon cap deposited during the FIB preparation process (brown atoms) is present in all three atom maps and marks the original material surface (§2.1.4). To improve clarity, 2% of the total W atoms are shown while 50% of the total solute Re and Ta atoms are displayed. Of the three elements, only Re exhibits clustering, peaking at 200nm depth and becomes a more homogenous solution by ~300nm depth. Figure 4.3.1b) shows the corresponding cluster diameter and volume fraction frequency distributions, with data points measured at 10nm intervals. For the first ~150nm below the sample surface, the cluster diameter stays relatively consistent. Below 150nm, the cluster size decreases and the volume fraction peaking at 20% also drops and disappears by 300nm. These trends correlate well with the predicted SRIM damage profile also shown in Figure 4.3.1b). Thus the clusters within the first 150nm depth are taken as representative of the material so cluster analysis is based exclusively on this region.

a)

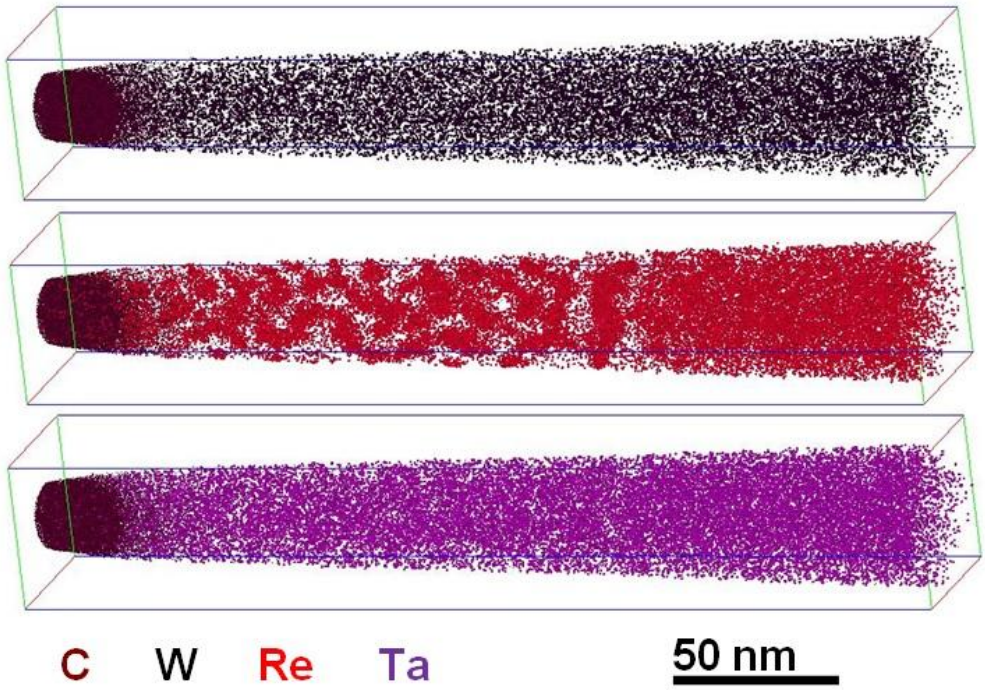

b)

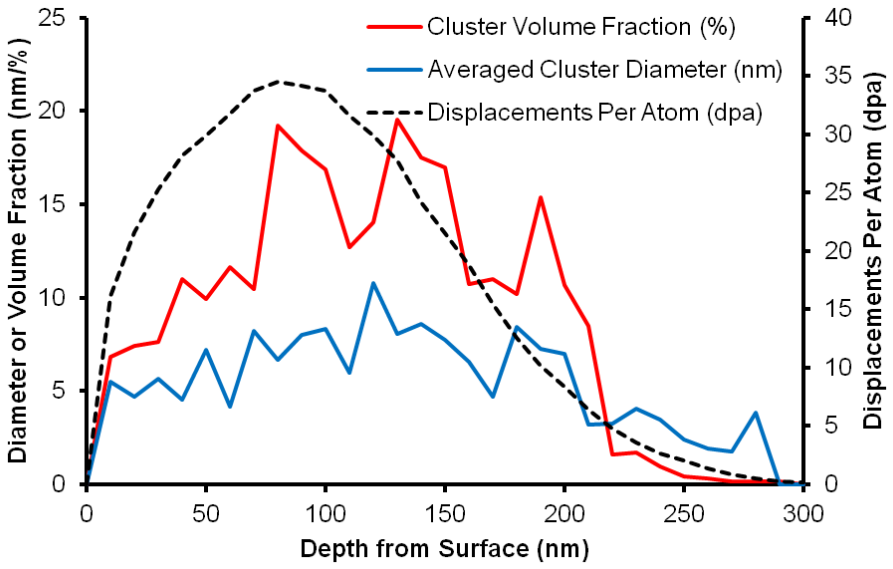

Figure 4.3.1. a) Complete 3D atom maps reconstructions of W-2Re-1Ta irradiated to 33dpa 773K, showing one element per atom map: Tungsten (top), Re (middle) and Ta (bottom) along with brown carbon cap. b) Plots of ion damage (SRIM) as well as cluster volume and diameter against reconstruction depth.

4.3.2 Effect of Ta on Re Clustering

Figure 4.3.2a-d) shows the atomic distribution within 4nm thick reconstruction slices of the subsurface damage regions (depth less than 150nm) in W-2Re-1Ta and W-2Re specimens irradiated to 33dpa at 573 and at 773K. The corresponding data on the averaged cluster composition, radii, volume fractions and number densities are reported in Table 4.3.1. It is apparent that the presence of Ta in the W-2Re-1Ta alloy hinders Re cluster development at both irradiation temperatures. After irradiation at 573K, the Re clusters are less visible in the ternary alloy (Figure 4.3.2a) compared to the binary alloy (Figure 4.3.2b). The calculated cluster volume fraction is a factor of three lower in the W-2Re-1Ta alloy compared to the W-2Re alloy. The cluster radii and Re content are however similar in the two alloys.

	573K 33dpa W2Re	773K 33dpa W2Re	573K 33dpa W2Re1Ta	773K 33dpa W2Re1Ta
Cluster Re (at.%)	8.0 ± 1.4	12.8 ± 2.9	6.2 ± 1.1	13.6 ± 2.4
Cluster Ta (at.%)	n/a	n/a	0.8 ± 0.4	0.2 ± 0.1
Matrix Re (at.%)	1.4 ± 0.1	1.2 ± 0.1	1.8 ± 0.1	0.9 ± 0.1
Matrix Ta (at.%)	n/a	n/a	0.9 ± 0.1	0.9 ± 0.1
Bulk Re (at.%)	2.0 ± 1.4	2.3 ± 2.9	1.9 ± 1.1	1.8 ± 2.4
Bulk Ta (at.%)	n/a	n/a	0.9 ± 0.4	0.9 ± 0.1
Radius (nm)	2.4 ± 1.0	3.3 ± 1.9	2.1 ± 0.8	3.4 ± 1.3
Volume Fraction (%)	9.01 ± 0.38	11.21 ± 0.74	3.15 ± 0.21	7.11 ± 0.5
Number Density (x1000 μm^{-3})	1716.5 ± 72.0	811.6 ± 53.6	1065.8 ± 70.0	499.2 ± 37.8

Table 4.3.1 Averaged cluster characteristics for W-2Re and W-2Re-1Ta at the two irradiation conditions.

After irradiation at 773K, in both alloys the cluster volumes, radii and Re content are higher and the number densities lower than for the 573K irradiation. The clusters in the W-2Re-1Ta and W-2Re alloy irradiated at 773K have similar radii and Re

concentrations of 3.3-3.4nm and ~13% respectively, greater than at 573K. Further, the cluster number density and volume fraction in the irradiated ternary alloy are significantly lower than in the binary alloy.

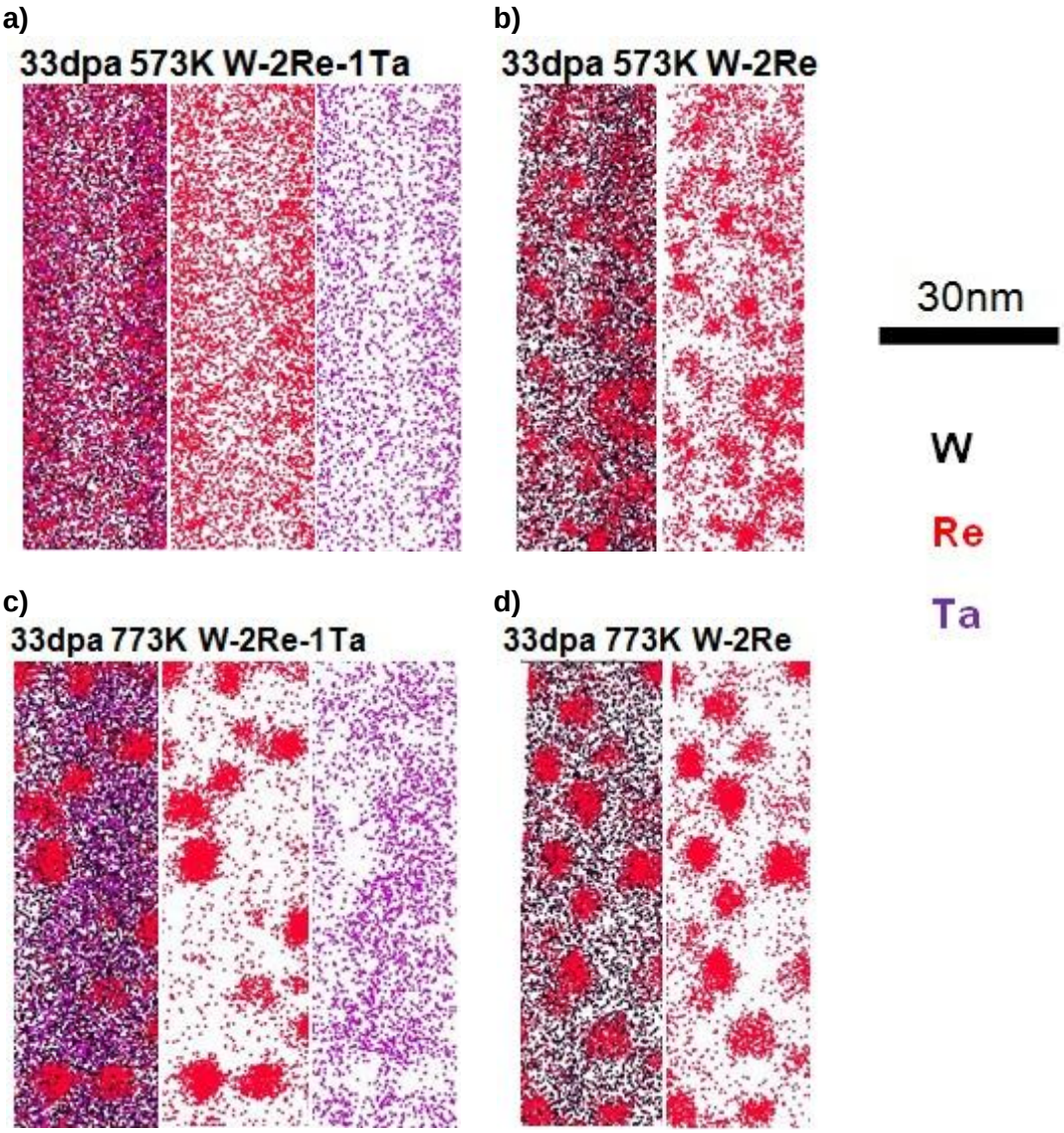

Figure 4.3.2. 4nm thick Sections from atom maps showing distribution of atomic species distribution following W-ion irradiation in: a) W−2Re−1Ta and b) W−2Re at 573K; c) W−2Re−1Ta and d) W−2Re at 773K. W, Re and Ta atoms are shown in black, red and purple respectively. The atom maps are extracted from 0-150nm depth range where clustering is most consistent.

4.3.3 Cluster Structure

Proxigram analyses in Figure 4.3.3a-b) show the radial Re composition, measured at 0.2nm intervals and averaged for 10 median radii clusters (identified with an iso-surface value at 60% of the mean cluster composition). The proxigrams for the W-2Re alloy are reproduced from Figure 4.2.3b). At both irradiation temperatures, the Re composition profiles for W-2Re-1Ta and W-2Re alloys are similar. They both feature a smooth decrease in Re concentration with radial distance. The compositions at the cluster core for 573 and 773K irradiation temperatures are 12 and 27at.% Re respectively, well below the sigma phase composition of 50at.% Re [47, 146].

The corresponding Ta radial composition for clusters in W-2Re-1Ta alloy is shown in Figure 4.3.3c) for both irradiation temperatures. At 573K, the Ta profile shows a slight decrease in composition towards the cluster core, further confirmed in Table 4.3.1 where 0.8at.% Ta is the measured mean composition for clusters in the W-2Re-1Ta alloy. The depletion of Ta within the cluster becomes more significant at 773K; the Ta composition drops to zero towards the cluster core; having an mean Ta composition of 0.2at.% (Table 4.3.1). Thus, Ta depletion within the clusters in the W-2Re-1Ta alloy is apparent at both temperatures, confirmed by the 1D profile(s).

Further, a cluster in the W-2Re-1Ta alloy at 773K is imaged along the <110> pole of the reconstruction in Figure 4.3.3d). In this 3 nm thick atom map, the Re atoms (red) are strongly aligned with the (110) planes of the tungsten matrix (black atoms). It shows the clusters are at least semi-coherent, unlike for irradiation induced precipitates such as sigma and chi which are completely incoherent with the BCC matrix [46, 47].

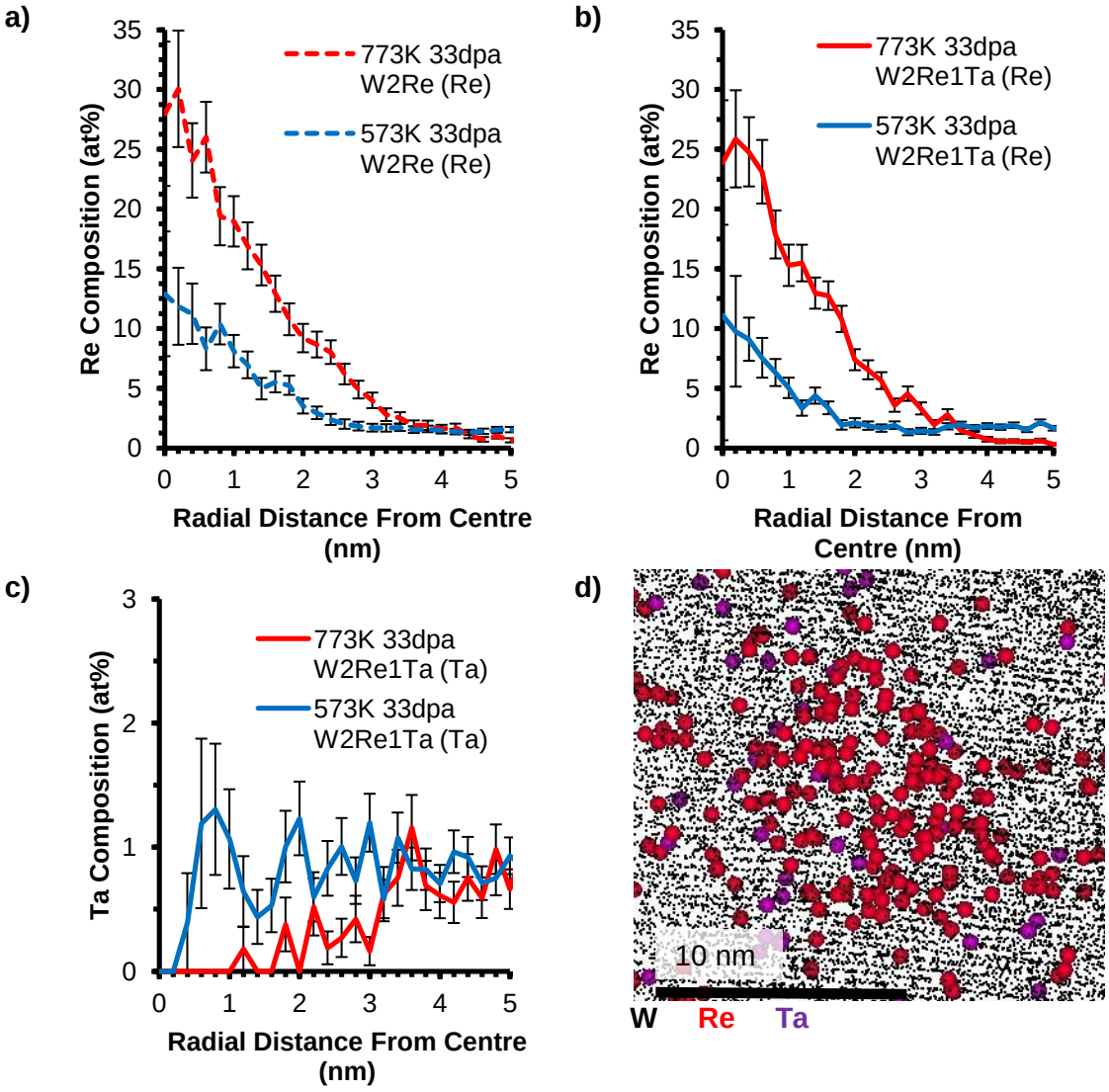

Figure 4.3.3 Proximity histograms showing at both irradiation conditions (a) Re variation within a typical cluster in the W−2Re alloy (reproduced from § 4.2.3b); (b) Re variation within a typical cluster in the W−2Re-1Ta alloy. c) Ta variation within a typical cluster in the W−2Re-1Ta alloy. (d) Typical cluster within W-2Re-1Ta imaged along <110> pole.

A 1D concentration profile is created from a typical cluster in W-2Re-1Ta alloy irradiated at 33dpa 773K as shown in Figure 4.3.4a-b). The clusters were identified

using iso-surface value of 7at.%Re. The choice of iso-surface value was explained previously in §4.2.4.The enrichment at the core reaches 30at.% Re same as the proxigram analyses in Figure 4.3.3a-c). The 1D concentration analysis validates the repeatability and accuracy of the proxigram analysis. It confirms the clusters are strongly enriched at its core.

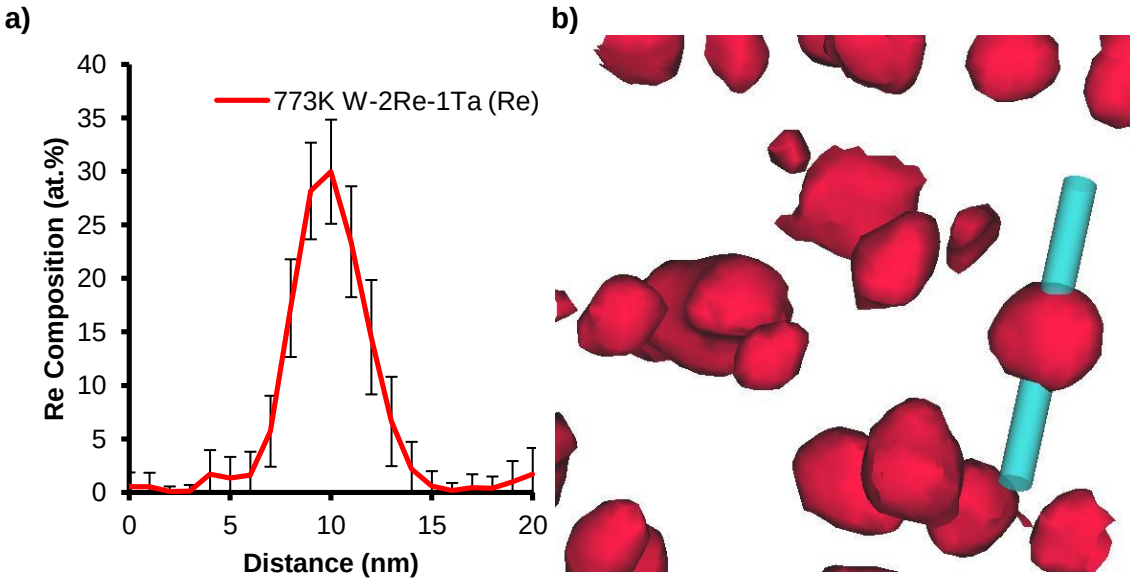

Figure 4.3.4 (a) 1D concentration profile of Re in a typical cluster in W-2Re-1Ta at 33dpa 773K and corresponding iso-surface map (b) at 7at.% Re.

4.3.4 Cluster Size Distributions

Cluster size distribution histograms for W-2Re-1Ta and W-2Re samples irradiated to 33dpa at 573 and 773K and are presented in Figure 4.3.5a-b). The analysed reconstructions each contained 500 – 1000 clusters in accordance with (§3.2.5). To facilitate comparison each plot has been normalised to represent the number of clusters per 1μm^3 volume. All plots feature a sharp drop in values at 0.5-1nm radius

range which is a result of the cluster analysis process; clusters with fewer than 20 solute atoms (i.e. Nmin <20) are discarded.

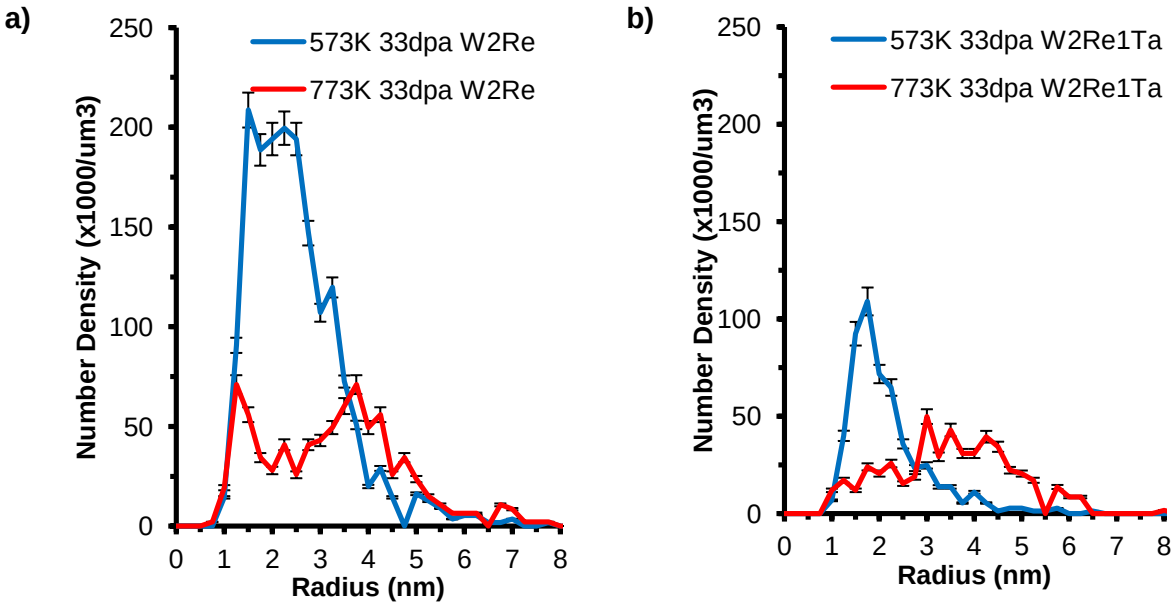

Figure 4.3.5 Number density normalised cluster radius distribution plots for a) W−2Re alloy and b) W−2Re−1Ta at both irradiation conditions.

The presence of Ta in the W-2Re-1Ta alloy correlates with a reduced level of clustering in comparison to the W-2Re alloy. At 573K, the W-2Re-1Ta peak height is twofold smaller than for W-2Re alloy. At 773K, the W-2Re alloy shows a bimodal distribution, with both peaks almost twofold higher than the single peak for the W-2Re-1Ta alloy.

On the other hand, higher irradiation temperatures appear to result in consistent broadening of the cluster distributions for both alloys. At 573K, the distribution breadths for both alloys are consistently 50-60% smaller than the breadth at 773K. Whilst Ta affects the amount of clusters nucleated, it has negligible effect on the size and growth of clusters.

4.3.5 Binary W-4Ta and W-2Re Alloys

Analysis of W-2Re-1Ta alloy suggests Ta is incapable of clustering which is investigated further here for a W-4Ta alloy. Figure 4.3.6a&b) show the distribution of solute atoms within a 4nm thick atom map slice for the W-4Ta and W-2Re alloys respectively, irradiated to 33dpa at 573K. Visually, no significant Ta clustering is apparent in W-4Ta, in contrast the clustered Re atoms in the W-2Re alloy. To justify this statistically, Figure 4.3.6c) shows the radial concentration distribution averaged across all solute atoms in the data sets for this irradiated W-Ta alloy and for the W-2Re alloy irradiated under the same conditions. The analysis of the distribution of Ta atoms in the W-4Ta produces a flat profile, indicating a homogeneous distribution of these solutes, while in the W-2Re alloy, the distribution has a maximum at short inter-atomic distances, indicating clustering.

In Figures 4.3.7a&b), the cluster size distributions are plotted for the W-4Ta and W-2Re alloy irradiated to 33dpa 573K. Here, a lower Nmin parameter of 5 was used to identify smaller clusters. Each graph shows two plots: actual experimental data - “unrandomised” clustered data set and a homogeneous data set that has been compositionally “randomised”. Both “unrandomised” and “randomised” distribution plots show a strong overlap for the for the W-4Ta alloy, unlike that in the clustered W-2Re alloy, which feature large deviations. The result confirms no clusters are detectable in the W-4Ta alloy and proves Ta is incapable of clustering under irradiation.

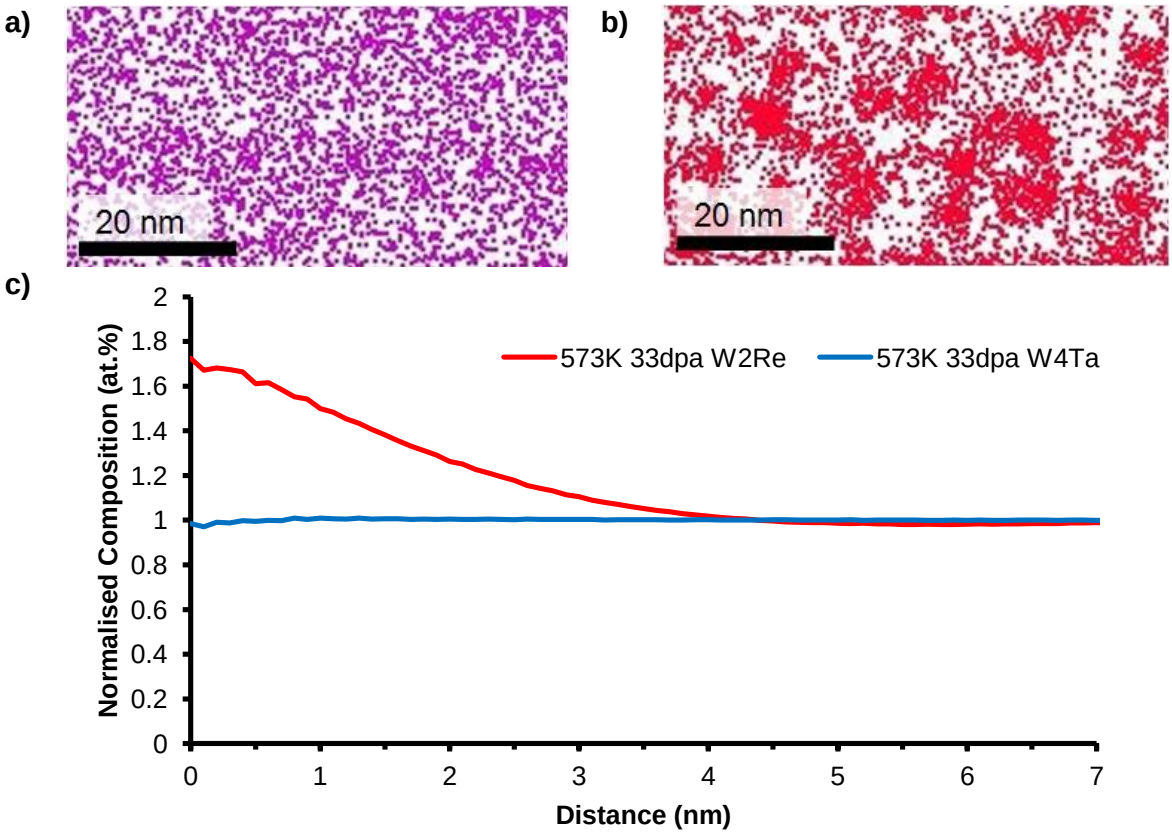

Figure 4.3.6 4nm thick slices through atom maps showing a) Ta atom for W−4Ta 33dpa, 573K and b) Re atoms for W−2Ra 33dpa and 573K. c) Radial distribution function plot for Ta atoms in W−4Ta 33dpa and 573K and Re atoms in W−2Re at 33dpa and 573K.

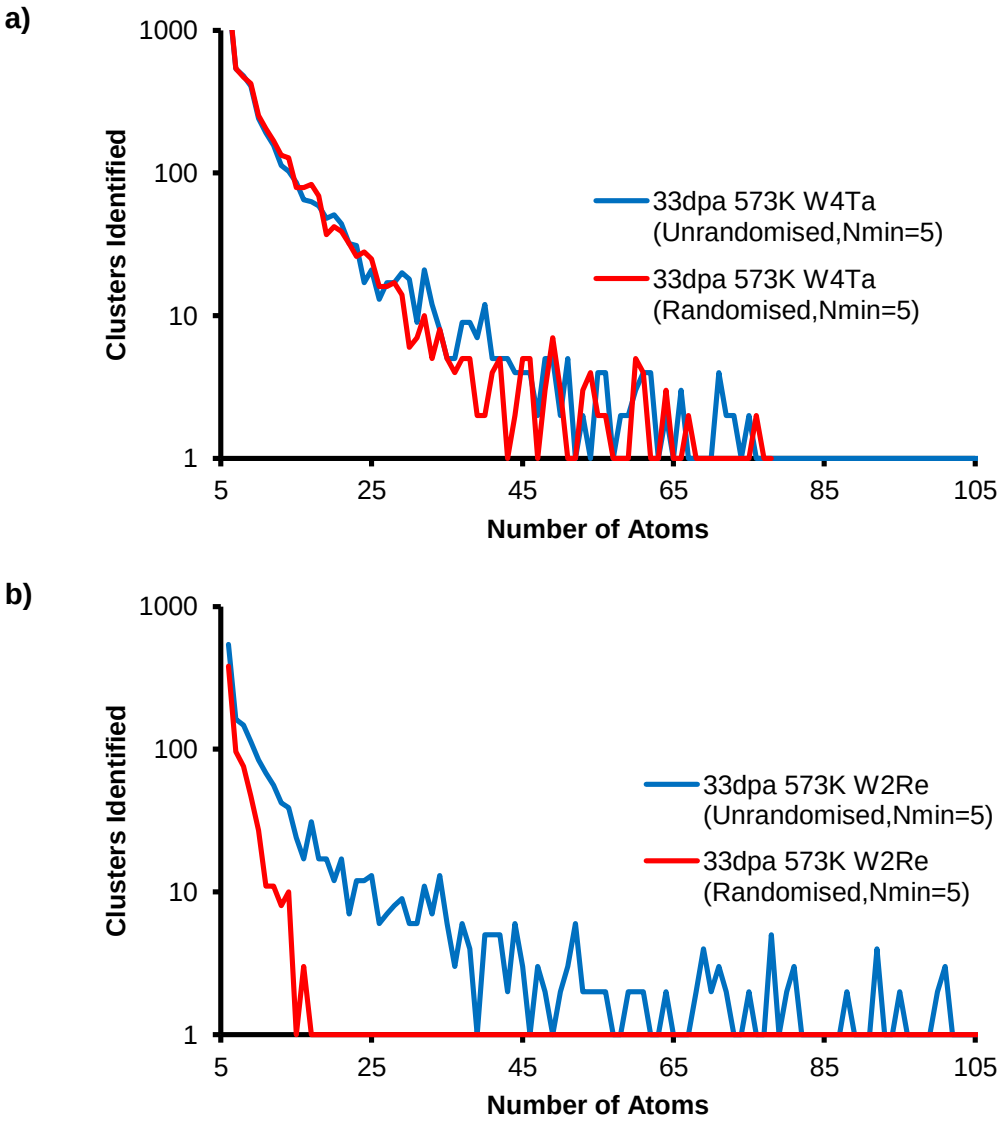

Figure 4.3.7 Cluster size distribution graphs showing cluster frequency for different cluster sizes (measured in number of atoms) for (a) W-4Ta and (b) W-2Re alloys all irradiated to 33dpa 573K.

4.3.6 Discussion: Irradiation of W-2Re-1Ta Alloys

4.3.6.1 Clustering in W-2Re-1Ta and W-Ta alloys

Here, we deliberately selected a higher Ta content alloy; W-4Ta to promote the probability of clustering, however visual atom map scrutiny along with statistical analysis both demonstrate no clusters apparent. Under 33dpa 573K irradiation where only interstitials are mobile [113], Ta interstitials formed in the W-4Ta and W-2Re-1Ta alloy appear to have no tendency to cluster. Where Ta is in coexistence with Re in the W-2Re-1Ta alloy, Ta actually becomes depleted within Re clusters formed, which is clearly demonstrated in the proxigrams of Figure 4.3.3c). The inability of Ta to cluster at 573K could be a reason for the irradiation hardening plateau observed by Armstrong et al. who irradiated W-5Ta alloy to the same temperature and dose [108]. The hardening in W-5Ta is mainly due to dislocation hardening whose density saturates at 1.2dpa onwards according to studies by Yi et al [75]. Only cluster formation brings about a linear increase in irradiation hardening, as noted by Armstrong et al for W-5Re under the same irradiation conditions.

At 773K, where vacancies become mobile, the inability of Ta to form clusters in W-2Re-1Ta alloy is also evident from a diffusion perspective. Under equilibrium conditions, the diffusion coefficients of Re or Ta are very similar at 773K. Ta has an activation energy and diffusion coefficient for diffusion in tungsten of 6.20eV and $6.20x10^{-4}m^2s^{-1}$ respectively, similar to 6.18eV and $4.00x10^{-4}m^2s^{-1}$ for Re [39]. According to the Arrhenius diffusion equation, the diffusion coefficient for Ta in W is $2.3x10^{-44}m^2s^{-1}$ while for Re in W it is $2.0x10^{-44}m^2s^{-1}$. Both solutes therefore have similar diffusion coefficients but Re forms clusters and Ta does not. In fact, Ta is

depleted within the Re clusters; reaching 0at.% at its core (Figure 4.3.3c) and having a mean of 0.1 at.% Ta (Table 4.3.1).

Despite being unable to cluster, Ta still affects the clustering behaviour of Re atoms in the W-2Re-1Ta alloy. At 573 and 773K, the measured cluster number density and volume fraction in W-2Re-1Ta sample is consistently twofold lower than that in the W-2Re sample. Ta is strongly correlated with a reduced amount of cluster formation. However, Ta has minimal effect on cluster size. The cluster size distribution plots in Figure 4.3.4a-b) for W-2Re-1Ta at 773K feature the same range (0.5-7nm) and peak position (3.5 nm) as that of the W-2Re alloy at 773K. The underlying mechanisms involved are unknown and further DFT modelling is required.

4.3.6.3 Irradiation Hardening

The hardening of the alloy samples pre and post irradiation are presented in Figure 4.3.8 with each data point extracted at a depth of 125nm (corresponding with peak damage level). The hardness measurements were taken by Dr Dave Armstrong and Dr Christian Beck. In the unirradiated state, the Ta presence has stronger solid solution hardening effect than Re, in agreement with the available literature [104, 105]. Using a Vickers Hardness test, Field et al reported W-8Re-8Ta alloy has a hardness of 3.39GPa higher than W-8Re alloy with a hardness of 2.92GPa. Here, the W-2Re-1Ta alloy has a hardness of 6.93GPa, 1.08GPa higher than W−2Re alloy with hardness of 5.85 GPa.

However, the W-2Re-1Ta alloy experiences a lesser degree of irradiation hardening compared to the W-2Re alloy. At 33dpa and 573K, the irradiation hardening in the W−2Re-1Ta alloy is 2.26GPa, ~roughly 1GPa lower than the irradiation hardening in W-2Re alloy, 3.27GPa. Similarly, at 33dpa and 773K, the difference in hardening

between ternary and binary alloy is greater, the W-2Re alloy hardening is 3.84GPa whereas the W-2Re-1Ta alloy has a hardening of 2.58GPa. The Ta presence produces a much smaller irradiation hardening effect in the ternary alloy as compared to the binary alloy. Such behaviour is linked to the reduced cluster presence in the W-2Re-1Ta alloy whose cluster volume fraction and number density is consistently smaller in the W-2Re-1Ta than W-2Re alloy at both temperatures.

The W-4Ta alloys irradiated to 33dpa 573K experiences an irradiation hardening of 2.84 GPa. It is difficult to compare with the W-2Re-1Ta alloy given the fourfold difference in Ta content.

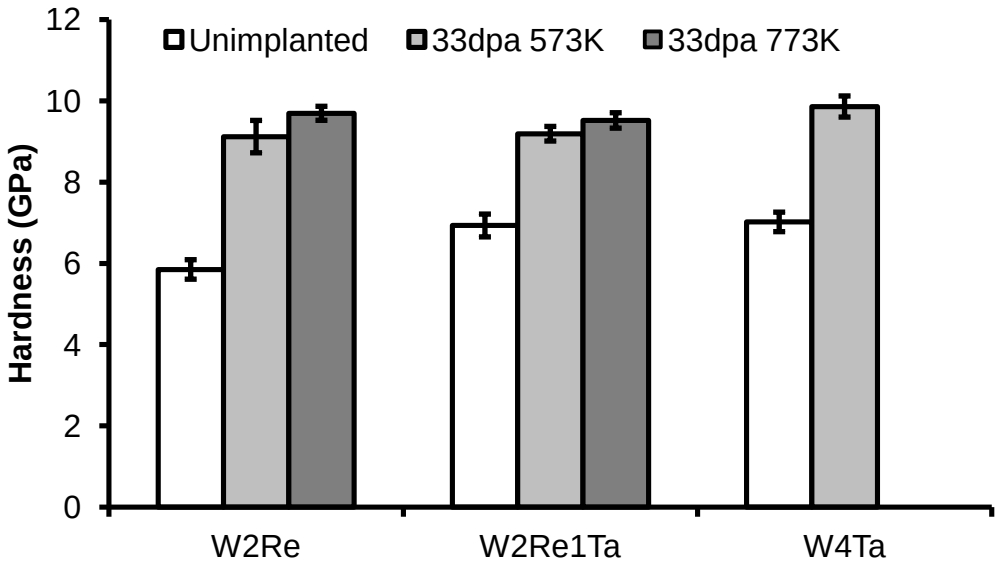

Figure 4.3.8 Hardness of irradiated and unirradiated alloys taken at the 125 nm depth from the material surface.

The same cluster analysis achieved in §4.2.5.5 was used to investigate the angles dislocations subtend in passing through the clusters. The calculated angles are reported in Table 4.3.2 for W-2Re-1Ta alloy irradiated at 33dpa at 573 and 773K. The critical angle for W-1Re-1Os and W-2Re alloys irradiated at the same

conditions are also listed in the table as reproduced from Table 4.2.2. For the W-2Re-1Ta alloy, the angles dislocations subtend are also ~80^{o}. So, like clusters in the W-1Re-1Os and W-2Re alloy, clusters in the W-2Re-1Ta alloy are also coherent and individually offer minimal resistance to dislocation motion. It is interesting to note smaller λ values (higher cluster number density) are correlated with higher irradiation hardening. Hence, higher cluster number density is correlated with larger irradiation hardening. This trend is consistent with §4.2.5.5 where we stated cluster number density has a large effect on irradiation hardening.

Alloy	ΔH at 125nm (GPa)	Δτ [ΔH/5] (GPa)	λ Cluster spacing (nm)	$\Phi_{critical}$ (^{o})
W2Re1Ta 773K	2.58	0.43	5.9	80.2
W2Re1Ta 573K	2.26	0.38	5.7	81.2
W-1Re-1Os 773K	5.38	0.90	3.6	78.5
W-1Re-1Os 573K	3.22	0.54	4.2	80.9
W-2Re 773K	3.84	0.64	4.1	79.9
W-2Re 573K	3.26	0.54	3.6	81.7

Table 4.3.2 Calculated parameters used for determining the critical angles dislocation subtend in passing through the clusters, assuming they harden via the Friedel Relation for under-aged alloys [140].

4.3.7 Summary

The effect of Ta presence in W−Re alloys is investigated using atom probe and nanoindentation analysis. From these studies it is found that:

- Ta in W-Ta and W-2Re-1Ta alloys shows no clustering behaviour at temperatures both above and below the critical vacancy migration temperature 743K [113]. Only Re clustering takes place within the W-2Re-1Ta alloy.
- The cluster number density and volume fraction is reduced where Ta is present in the W-2Re-1Ta alloy. Nonetheless, Ta has minimal effect on cluster composition and radius.
- Analysis of individual clusters formed in the W-2Re-1Ta alloy suggest complete coherency with the BCC tungsten matrix. These clusters are weak obstacles that individually offer small resistance to dislocation motion. Their hardening mechanism is based on a high number density.
- Ta does have a strong solid solution hardening effect but experiences less irradiation hardening compared to W-2Re alloy. The implication of this discovery is highly positive for tungsten fusion reactor components, although the strong solid solution hardening of Ta must be accounted for.

5. Irradiation of a Commercial W-Re Alloy

5.1 Introduction

This final chapter concerns the effect of external variables including free surface, material structure and temperature on clustering behaviour. Commercial alloys are used rather than lab-made alloys as they offer flexibility in specimen shape and structure, needed for the studies undertaken. The commercial alloys have similar levels of impurities as lab-made samples below 300ppm. Additionally, as the fusion reactor will also consist of commercial materials the study undertaken here is a closer simulation of irradiation induced clustering.

For investigating the effect of free surface on cluster behaviour commercial W-25Re alloys wires with diameters of 0.25 and 1mm (Goodfellows Ltd) were irradiated as needle and bulk samples respectively (§2.1.1-2.1.3). The samples were exposed to 1.2dpa of 2MeV W^+ ions at 573 and 773K and analysed in the atom probe.

Grain size and dislocation density effects on cluster formation were studied using W-5Re alloy plate (Plansee Ltd) and wire samples (Goodfellows Ltd) in annealed and unannealed states (§2.1.1-2.1.2), following irradiation with 33dpa W ions at 573K (§2.1.1-2.1.2). The plate samples featured larger grain sizes of 4-10µm diameter compared to the wire samples, 0.5-1µm diameter. The difference in grain size is visually illustrated in Figure 2.1.1 (§2.1.1). Also, the unannealed samples have higher dislocation densities compared to the annealed sample. Armstrong et al [11, 96] used EBSD to measure the density of geometrically necessary dislocations (GND), as 4.8×10^{13}lines/m^2 for annealed and 1.4×10^{14}lines/m^2 for unannealed plate samples.

Finally, the role of temperature on cluster formation across different W-Re contents was examined using annealed W-3Re, W5Re and W25Re alloys wires of 1mm diameter (Goodfellows Ltd) following irradiation to 33dpa at 573 and 773K as bulk samples (§2.1.1 – 2.1.3). These commercial alloys have grain size of 0.5-1μm diameter. The effect of grain size at 773K can be ascertained by comparing the clustering results with lab-made alloys irradiated under the same conditions. The lab-made alloys have considerably larger grain size 1-3mm diameter (Figure2.1.2, §2.1.1) compared to the wire samples.

As with other chapters, all hardness data reported here were obtained and provided by Dave Armstrong and Christian Beck. Their methodology is detailed in §2.1.6.

5.2 Needle vs Bulk Irradiation

5.2.1 Results – Clustering Behaviour in Needle and Bulk Samples

Irradiation induced clusters in the W-25Re alloy following irradiation at 1.2dpa at 573 and 773K are visualised as 6nm thick atom maps in Figure 5.2.1a-d). In each column, the clusters are firstly presented in the full reconstruction and also as separated from the matrix. Only Re atoms (red dots) are shown, illustrating clusters in “bulk” (Figure 5.2.1a&c) and “needle” (Figure 5.2.1b&d) specimens. Note “bulk” refers to wires polished cross-sectionally irradiated as a flat circular area 1mm in diameter while “needle” refers to wires 0.25mm in diameter irradiated as electropolished wires (§2.1.2). Table 5.2.1 shows the averaged cluster composition, diameter, number density and volume fraction for each sample.

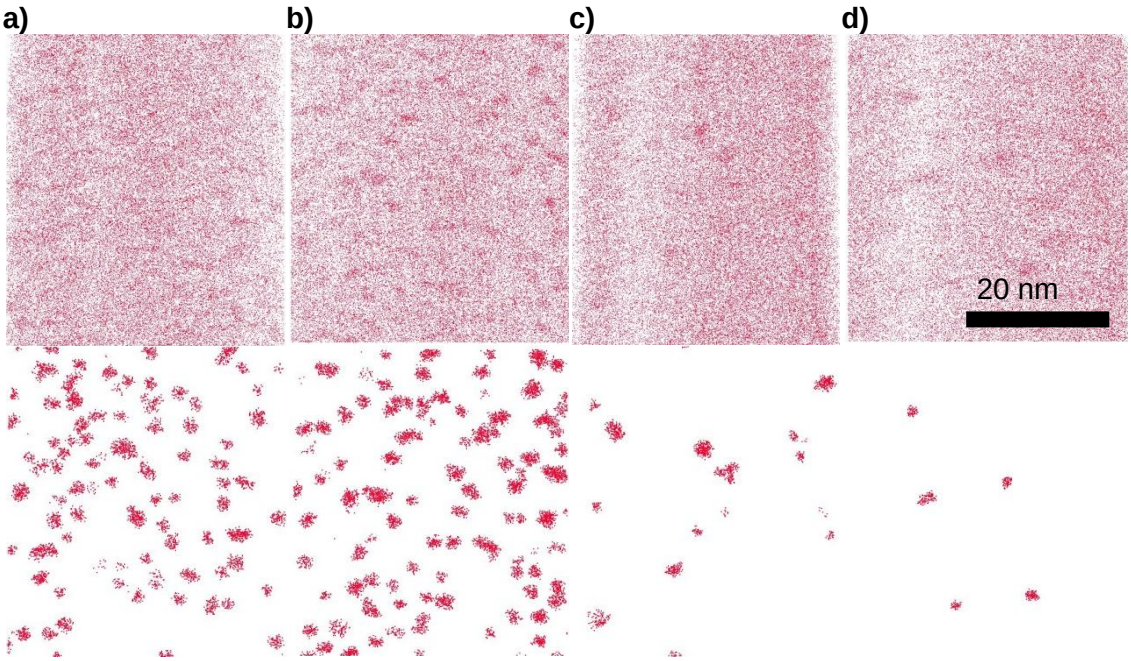

Figure 5.2.1 W-25Re at 1.2 dpa; Atoms maps showing full Re distributions and as isolated clusters for (a) 573K bulk, (b) 573K needle (c) 773K bulk and (d) 773K needle.

	Re Composition (at%)	Average Diameter (nm)	Number Density (x1000/μm^3)	Volume Fraction (%)
1.2dpa 573K (Bulk)	32.6 ± 3.2	2.0 ± 0.5	7001 ± 236	5.9 ± 0.2
1.2dpa 573K (Needle)	34.5 ± 3.3	2.3 ± 0.7	7956 ± 258	10.3 ± 0.3
1.2dpa 773K (Bulk)	35.2 ± 4.1	2.0 ± 0.6	695 ± 58	0.7 ± 0.1
1.2dpa 773K (Needle)	43.6 ± 5.4	1.9 ± 0.4	264 ± 72	0.2 ± 0.1

Table 5.2.1 Average cluster composition, diameter, number density and volume fraction in W-25Re alloy at 1.2 dpa 573K and 773 K, Irradiated as needle and bulk samples.

Figures 5.2.1a-d) appears to show on visual inspection that the wire and bulk samples respond to the two irradiation conditions in a similar manner. However, the quantitative analysis presented in Table 5.2.1 uncovers clear differences. At 573K, the cluster volume fraction in the needle is 10.3%, while that in the bulk is 5.9%.

However, this difference is reversed at 773K, where the cluster volume fraction in the needle sample is 0.2%, and in the bulk sample is 0.7%.

Table 5.2.1 shows the Re composition is consistently higher in the needle sample than the bulk sample, although they are within each other's error bars. At 573K, the clusters in needle sample measured 34.5at.% Re, 1.9at.%Re higher than the bulk sample, 32.6at.%Re. The difference is greater at 773K. The needle sample clusters contain 43.6at.%Re, 8.4at.%Re higher than the bulk sample, 35.2at.%Re. It seems the greater free surface of the needle sample has a slight effect on cluster chemistry.

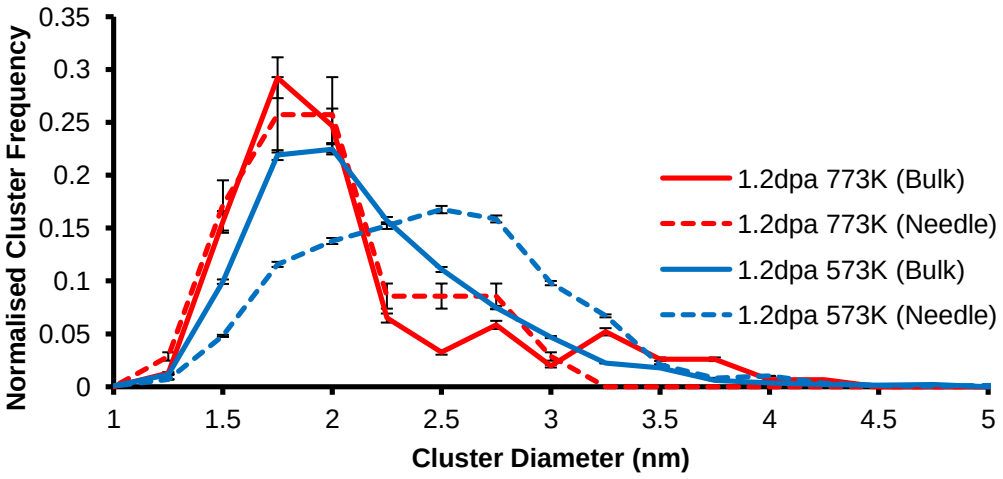

Figure 5.2.2 Cluster size distributions for W-25Re alloy (bulk and needle samples) exposed to 1.2 dpa at 573/773 K.

The cluster nucleation and growth mechanics are explored further with cluster size distribution plots in Figure 5.2.2. Each distribution shows the normalised cluster frequency at different cluster diameters. There are differences between needle and bulk at both temperatures, being most pronounced at 573 K. At 1.2dpa 573K, the peak of the needle sample is shifted further to the right than the bulk sample, indicating that the clusters are coarser in the needle sample relative to the bulk. At

773K, the shape and peak height of the distributions are quite similar, but the cluster distribution in the needle sample extends to 3.2nm diameter, slightly smaller than in the bulk sample, 4.5nm. Thus at the higher irradiation temperature, the mean cluster size is slightly larger in the bulk sample than in the needle sample.

5.2.2 Discussion – Effect of Sample Shape

In the literature, simulations of dislocations in irradiated TEM foils [147] and void/interstitial cluster distribution near grain boundaries in tungsten [148] show that free surface effectively act as defect sinks. Thus, the close proximity of large free surface afforded by the needle samples is likely to have a stronger influence on the cluster formation mechanics when compared against the bulk sample. At 773K, where vacancies drive cluster formation [113], the loss of vacancies to free surface could have brought about the lower cluster volume fraction and number density observed. At 573K, interstitials drive cluster formation so this same loss of vacancies to the free surface may have resulted in less annihilation of interstitials, possibly enabling more clusters to form. As a result, at the lower temperature, cluster behaviour is more pronounced in the needle sample (relative to bulk), while at the higher temperature, the reverse trend is true. These hypotheses have yet to be verified with future DFT and Monte Carlo simulations.

Referring back to §3.2.2, lab-made plate W-25Re alloy was irradiated under same condition: 1.2dpa and 773K. The clusters in this lab-made W-25Re alloy had a number density 6.63×10^5 clusters/μm^3 and volume fraction 0.4%. These values fall within the range of values measured for the commercial W-25Re alloy irradiated at 1.2dpa and 773K in bulk form. But, they are higher than the commercial W-25Re

alloy needle form samples. The repeatability of results for bulk lab-made plate and bulk commercial wire samples confirms the free-surface effect in needle commercial wire specimens. Also, it appears that grain size has negligible effect on clustering at these irradiation conditions. Even though the lab-made alloys have a grain size 1-3mm diameter much greater than commercial wire alloys 0.5-1μm in diameter.

5.3 Effect of Dislocation Density and Grain Size

This sub-section studies the effect of dislocation density and grain size on cluster formation. In order to avoid self-annealing effects, a low irradiation temperature of 573K was chosen, below the vacancy activation temperature, 743K [113]. Also, a larger dose of 33dpa was used to increase the degree of clustering, especially since the 1.2-3.6dpa conditions in §3.2.2 produced minimal clustering. To compare the effect of dislocation density samples are irradiated in annealed and unannealed state. The annealing temperature is used is 1273K below the recrystallisation temperature so grain size remains constant post-annealing. As stated in §5.1, Armstrong et al [11] showed via EBSD, the difference in dislocation density between annealed and unannealed state to be an orders of magnitude difference ($4.8x10^{13}$lines/m^2 for annealed and $1.4x10^{14}$lines/m^2 for unannealed). The grain size effect is achieved by choice of two commercial materials. A commercial wire samples (§2.1.1) with grain size of 0.5-1µm and commercial plate samples (§2.1.1) having larger grain size of 4-10 µm diameter. Also, the impurity content remains constant across all samples studied being in the range 200-300ppm.

5.3.1 Clustering in Plate and Wire samples (Annealed and Unannealed)

The variation of clustering with depth is illustrated for the annealed W-5Re plate sample (grain size: 4-10µm) irradiated to 33dpa at 573K in Figure 5.3.1 (in accordance with §2.3.2), a 4nm thick atom map showing isolated Re clusters. The clustering appears prominent up to ~200nm below the exposed surface beyond which there is a decline in cluster size and number density. The 200nm depth corresponds with the tail of the depth damage profile; the clustering fades into

homogeneity by 300nm, matching SRIM predictions for these implantation conditions (§2.1.3).

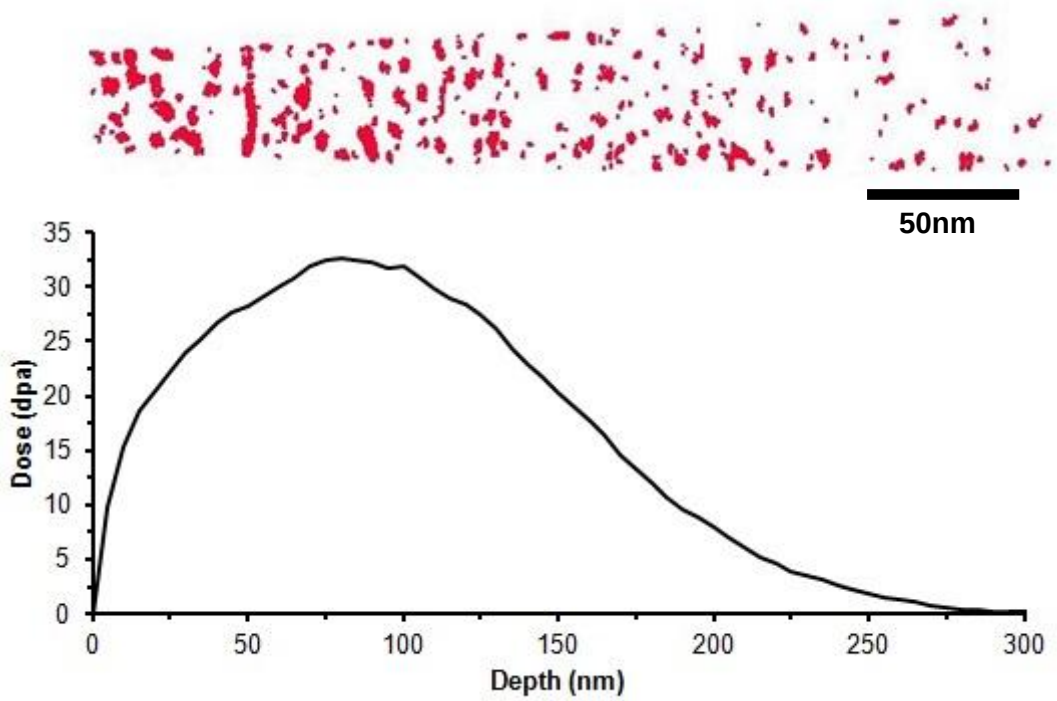

Figure 5.3.1 33dpa 573K Annealed W-5wt.%Re 4nm slice of Re clusters post separation from the reconstruction shown alongside SRIM prediction of dose variation with sample depth.

In the W-5Re alloy irradiated at 33dpa and 573K, cluster formation took place in all plate and wire samples (grain size: 4-10μm and 0.5-1 μm respectively) in annealed and unannealed condition. Figure 5.3.2a-d) presents 2nm thick atom maps taken at the 0–150nm depth range below the material surface. For each sample, the figure shows the representative Re atom maps in the original reconstruction. Alongside it is the clusters as separated from the matrix, with the individual clusters assigned different colours to improve clarity. Table 5.3.1 summarises the cluster

compositions, radii, number densities and volume fraction. The values are averaged from at least 500 clusters.

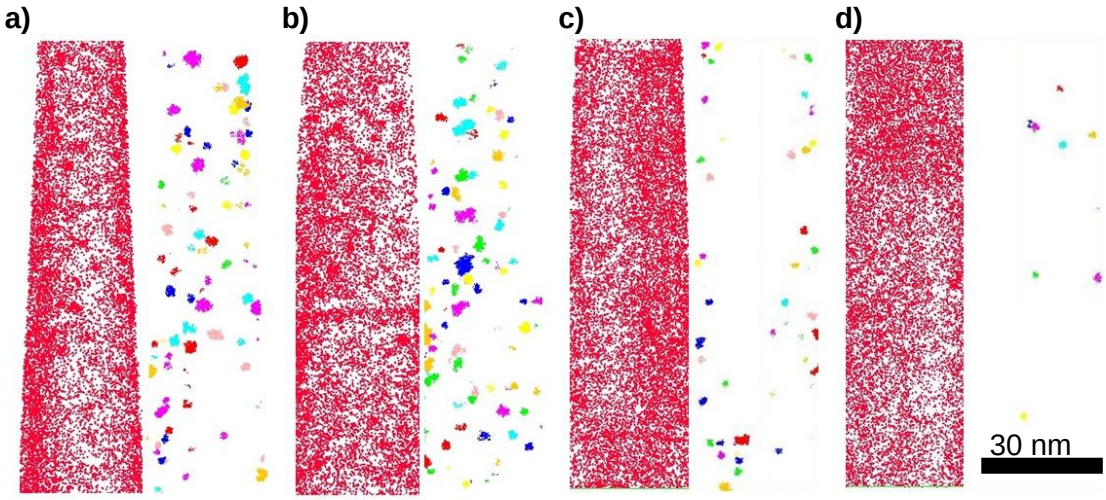

Figure 5.3.2 W-5Re irradiated at 33dpa 573K: Clusters in (a) annealed plate, (b) unannealed plate, (c) annealed wire and (d) unannealed wire samples. The original reconstruction showing all Re atoms is presented alongside the clusters as separated from matrix.

Average Grain Size	Annealed Plate 4-10μm	Unannealed Plate 4-10μm	Annealed Wire 0.5-1μm	Unannealed Wire 0.5-1μm
Cluster Re content (at.%)	13.8 ± 2.3	14.5 ± 2.5	13.7 ± 2.5	13.3 ± 2.3
Cluster Radius (nm)	1.7 ± 0.8	1.6 ± 0.8	1.3 ± 0.7	1.3 ± 0.6
Number Density (x1000/μm^3)	3086± 111	2299 ± 76	1190 ± 58	839 ± 43
Volume Fraction (%)	8.1 ± 0.3	5.5 ± 0.2	1.7 ± 0.1	1.2 ± 0.1

Table 5.3.1. W-5Re irradiated at 33dpa 573K: averaged cluster compositions, radius, number densities and volume fractions for wire and plate samples (annealed and unannealed).

Atom maps of wire and plate samples show a stronger clustering in plate samples than the wire samples. As Table 5.3.1 shows, the cluster volume fraction is 5-8% in the plate samples, significantly higher than for the wire samples, 1-2%. Between

annealed and unannealed samples, the annealed state contains a greater degree of clustering than the unannealed state. The annealed state consistently features a higher cluster number density (by a factor of 1.4-1.5) than their unannealed state for both plate and wire samples.

The cluster Re composition is unaffected by sample type, consistently being ~13.5at.% Re. Similarly the average cluster diameters: 1.3-1.7nm are all within each other's error bars so there are negligible differences.

5.3.3 Cluster Size Distributions

Figure 5.3.3 presents cluster densities counted at different radii in a normalised to a 1μm^3 volume for wire and plate samples in annealed and unannealed state implanted to 33dpa at 573K. The distribution plots are created in accordance with methodlogy described in §3.2.5. All plots feature a cut-off at 0.75nm radius enforced by the Nmin=20 parameter used.

The extent of cluster nucleation and growth is greater in the plate than the wire samples. In Figure 5.3.3, the distribution plot of the plate samples extends to 5nm radius, twofold higher than the wire samples whose plot extends to 2.5nm. Also, there is a marked difference in the peak height of the distribution plots between plate and wire samples. The plate samples peak at 5.5x10^5-6x10^{5}clusters/μm^3; while the wire samples peak at 2.510^5-3.8x10^{5}clusters/μm^3. In addition to having larger clusters, the plate samples have a substantially greater number of clusters, given by the areas under the different curves (cluster number density in Table 5.3.1).

Within each material form, the annealed state is slightly higher in amount of clusters formed. In the plate sample, the annealed state features a larger tailing extending to 5.5nm compared to 4.5nm for the unannealed state. For the wire samples, the annealed state has a higher peak ($3.8x10^5$clusters/μm^3) than the unannealed state ($2.0x10^5$clusters/μm^3).

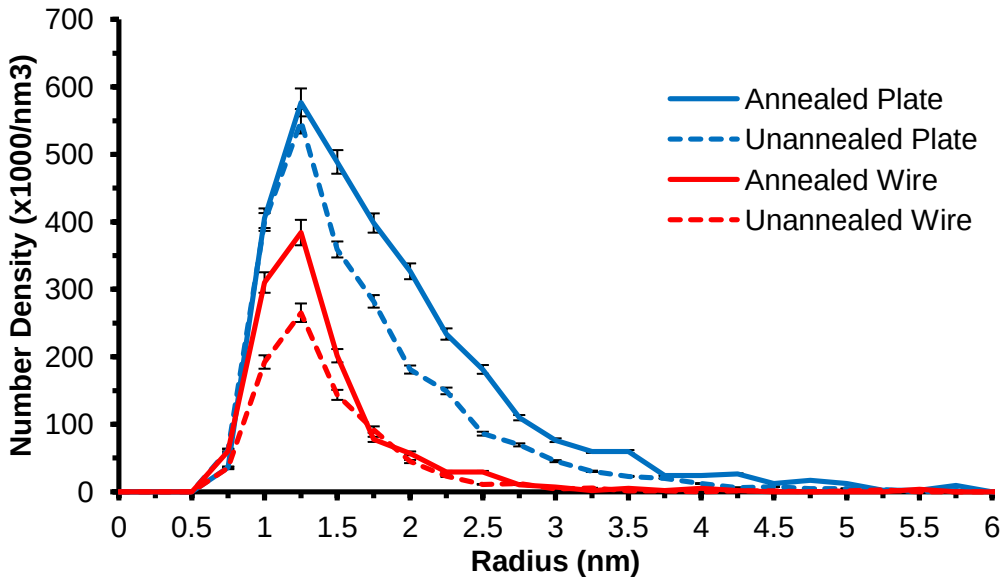

Figure 5.3.3 Cluster size distributions for annealed plate, unannealed plate, annealed wire and unannealed wire of W-5Re alloy irradiated at 33dpa / 573 K.

5.3.4 Grain Boundary Analysis

Grain boundaries within some of the reconstructions enabled detailed cross-sectional chemical analysis to be performed. Figure 5.3.4 shows proximity histogram profiles (see §4.2.4 for details) of grain boundaries in wire and plate samples of W-5Re alloy implanted to 33dpa at 573K. The proxigrams were calculated from a Re iso-surface of 7-8at.% Re and each profile is averaged from 1-2 different grain

boundaries. Also shown is the proxigram of grain boundaries in unirradiated W-5Re alloy as standard for comparison.

The grain boundaries within irradiated plate and wire samples (annealed and unannealed) featured a stronger degree of Re segregation compared to the unirradiated state. The composition at the centre of the grain boundary reaches 11-12at.% Re for the irradiated plate and 9-10at.% Re for the irradiated wire sample, compared to 7-8at.% Re for the unirradiated samples.

a)

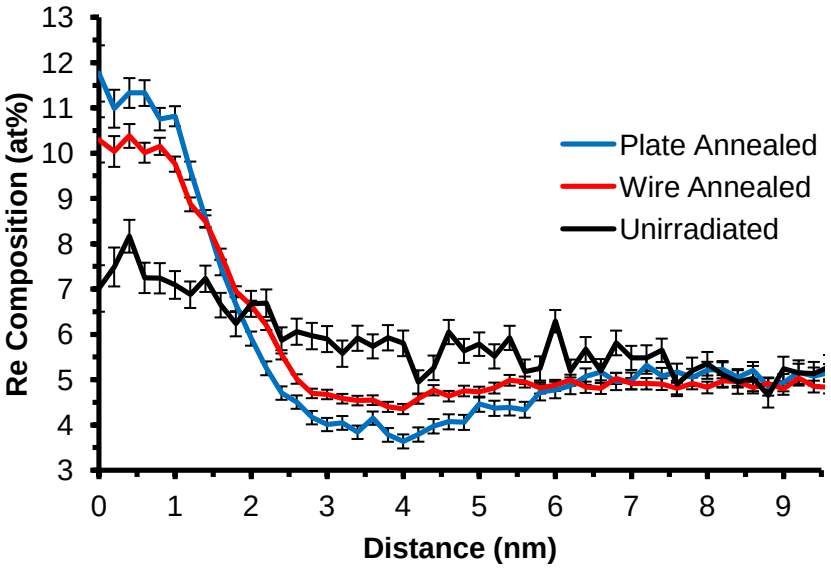

b)

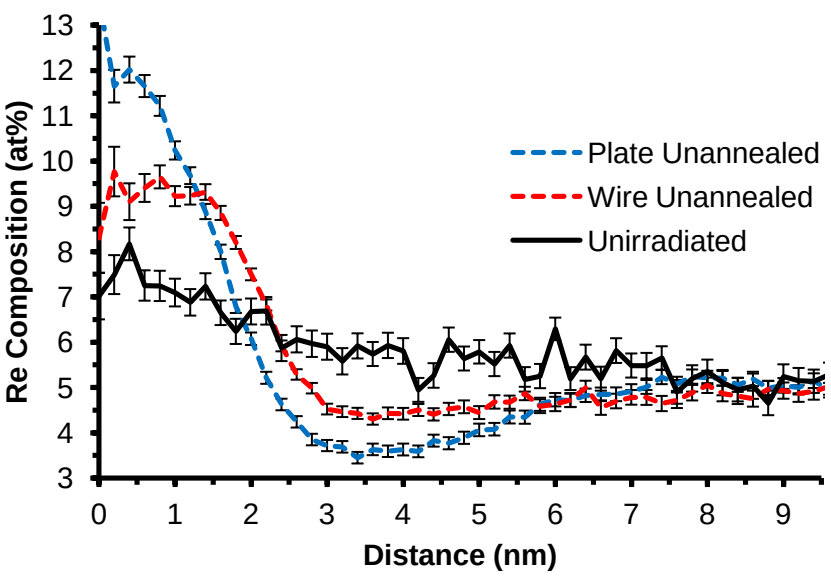

Figure 5.3.4. Proxigram analysis of grain boundaries in W-5Re irradiated to 33dpa at 573K: (a) annealed wire and plate samples and (b) unannealed wire and plate samples.

More pronounced segregation is present in the plate sample as they feature a larger depletion zone. In both Figure 5.3.4a) and b), the Re content in the depletion region (where composition drops below 5at.% Re. It is consistently lower in the plate (~3.5at.%Re) than the wire sample (~4.5at.%Re).

It is difficult to discern trends regarding the effect of annealing. For both wire and plate alloys, the composition at the grain boundary core and the depletion regions have similar values, falling within each other's error bars. Also, I acknowledge further work is needed to analyse more grain boundaries to determine whether segregation varies with grain boundaries.

5.3.5 Discussion – Effectiveness of Defect Sinks

According to literature, grain boundaries can act as defect sinks. Yoshiie et al [148] observed in TEM, a depletion of voids and defect clusters towards grain boundaries in Nickel irradiated to 0.2dpa neutron irradiation at 573K. This behaviour is also reflected in this study where the smaller grained commercial wire samples featured significantly lower cluster number density and volume fraction than the larger grained commercial plate samples. The trend can be extended to dislocations as well. For both commercial wire and plate samples, a more dislocated structure in unannealed state (Armstrong et al identified to have an order of magnitude greater in dislocation density than annealed state using EBSD [11, 96]) is correlated with a

reduced cluster number density and volume fraction compared to low dislocation density structures (annealed). Thus, the literature finding in conjunction with the trends seen in this experiment suggests grain boundaries and dislocations act as defect sinks.

Between grain boundaries and dislocation networks, it appears grain boundaries have a greater effect in hindering cluster development than the latter. It is evident when comparing the difference in cluster volume fractions in Table 5.3.1. A high dislocation density (unannealed plate or wire sample) brings about 1.5-2 times lower cluster volume fraction than a low dislocation density sample (annealed plate or wire sample). The difference factor is smaller compared to the effect of grain size. Small grained samples (commercial wire sample) have a cluster volume fraction 5-8 times lower than large grained (commercial plate sample).

Close examination of cluster size distributions in Figure 5.3.3 shows samples with smaller grain size or higher dislocation density consistently reduces the peak height or range. It is possible the loss of point defect to defect sinks reduces the total point defect population. Thus there is less drive for cluster formation to take place.

Re grain boundary segregation was also observed in this study. The work here is relevant with prior work by Humphry-Baker [53, 119] who also measured grain boundary enrichment of unirradiated commercial wire W-5Re alloy. Humphry-Baker measured a peak enrichment of 7.5at.% Re same as value reported here in Figure 5.3.4: 7-8at.% Re. The repeatability of this result highlights the accuracy of the experiment and analysis.

Additionally, I observed radiation enhanced grain boundary enrichment within W-Re alloys for first time. Grain size proved to have a strong effect on the degree of

enrichment whilst differences in dislocation density result in negligible differences. A possible explanation could be that the wire samples which feature smaller grain sizes offer a shorter diffusion distance for transport of Re compared to the plate samples that have a larger grain size. Hence, Re segregating to grain boundaries in wire sample are more saturated relative to that in plate samples.

5.3.6 Discussion – Irradiation Hardening of Wire and Plate Samples

Hardness measurements by Armstrong (personal communications) of the irradiated W-5Re plate and wire samples (annealed and unannealed) are reported in Table 5.3.6 (§2.1.6). Hardness values in the unirradiated state are listed in the first column and they vary due to differences in grain size and dislocation densities. Samples can however be compared with each other through the irradiation hardening values listed in the third column. Upon inspection, the strongest degree of hardening occurs for the annealed plate sample, 4.09GPa. The other three conditions have a similar hardening response of ~2.7GPa.

	Irradiated (GPa)	Unirradiated (GPa)	Hardening (GPa)
Annealed Plate	9.64 ± 0.78	5.55 ± 0.07	4.09 ± 0.78
Unannealed Plate	9.47 ± 0.56	6.78 ± 0.14	2.69 ± 0.56
Annealed Wire	10.32 ± 0.26	7.65 ± 0.02	2.67 ± 0.26
Unannealed Wire	11.68 ± 0.66	9.00 ± 0.45	2.68 ± 0.66

Table 5.3.6 Hardness of irradiation conditions pre and post irradiation (33dpa 573 K) of plate and wire samples in annealed and unannealed state for W-5Re alloy.

In section 5.3.5, it was found that low dislocation density (annealed samples) and large grain size (4-10μm in plate samples compared to 0.5-1 μm wire samples) promote cluster development. Thus, the annealed plate sample which satisfies this

condition has the highest degree of irradiation hardening. In comparing with the unannealed plate, the results do show smaller cluster volume brought about by a high dislocation density, reduces the degree of irradiation hardening. The trend is further reinforced by published literature data. In related hardness studies by Armstrong et al. [11, 149], the same commercial plate W-5Re sample was irradiated to 0-13dpa at 573K. The annealed plate showed a consistently higher irradiation hardening (0.8-1.3GPa) than the unannealed plate (0.2-0.4GPa) across the dose range studied.

However, the trend is not consistent between unannealed plate and unannealed wire samples. There is an order of magnitude difference in cluster number density between them (Table 5.3.1) but their irradiation hardening are both at ~2.7GPa. Similarly there is no difference between the annealed wire and unannealed wire samples. To speculate, it is likely the cluster volume fractions for these three samples are rather small and the dislocation hardening (as discussed in §3.3.4) might have a more dominant effect.

5.4 Effect of Irradiation Temperature

5.4.1 Visualising and Quantifying Clusters at 573 and 773 K

Atom maps of commercial wire W-3Re, W-5Re and W-25Re alloys (grain size of 0.5-1μm diameter, §2.1.1) irradiated to 33dpa at 573 and 773K are presented in Figure 5.4.1a). All atom maps are 2nm thick slices of the original reconstruction with only Re atoms displayed. For each sample, the clusters as separated from the matrix (§2.3.2) are shown alongside the original reconstruction for clarity. Similarly, the atom maps of lab-made W-2Re, W-5Re and W-25Re alloys (grain size of 1-3mm, §2.1.1) irradiated to 33dpa 773K are reproduced from §3.2.2 and shown in Figure 5.4.1b) and presented in same format.

To quantify these clusters, the averaged composition, diameter, length, number density and volume fraction are reported in Table 5.4.1 for each commercial alloy irradiated to 33dpa at 573K or 773K. The W-25Re alloy irradiated to 33 dpa at 773K features rod-shaped clusters so their lengths are reported (according to §3.2.4). Spherical clusters are present in other samples (§3.2.3) and their diameter is listed in Table 5.4.1. The corresponding cluster features for lab-made alloys, W-2Re, W-5Re and W-25Re at 33dpa 773K are reported in Table 5.4.2, reproduced from §3.2.2. The matrix Re and overall bulk composition are reported in Table 5.4.1 for both commercial and lab-made (§3.2.2) alloys. At both irradiation temperatures the bulk Re content is unchanged post irradiation.

At the same 33dpa dose, all commercial alloys irradiated at 773K featured greater cluster densities compared to the 573K condition. For the lower Re content alloys, W-3Re and W-5Re, clusters formed under at 773K have larger diameters than at 573K: For example, in Figure 5.4.1, the clusters in W-5Re alloy at 773K have

diameters of 10nm and strong local Re depletion whereas the 573 K condition has smaller 2nm diameter clusters and there is minimal Re depletion. In the W-25Re alloy, rod shaped clusters form at 773K while at 573K only smaller spherical clusters ~2mm diameter formed. The same variation with irradiation temperature was seen in lab-made W-2Re alloy irradiated to 33dpa 573 and 773K in §4.2.1 - §4.2.3.

The higher (bulk) Re content in commercial alloys raises the amount of clusters nucleated at either temperature. At 573K, the W-25Re alloy has a cluster number density fourfold higher than the W-3Re alloy. Similarly, at 773K, the cluster number density in the W-25Re alloy is also 4 times higher than W-3Re alloy.

The effect of different grain size between commercial and lab-made samples at 773K is apparent. In Table 5.4.2, grain size has slight effect on cluster chemistry and size with the values mostly within each other's error bars. Only the cluster number density which is consistently higher in the commercial alloys (small grain size 0.5-1μm diameter) than the lab-made alloys (large grained 1-3mm diameter). This is most pronounced for the W-25Re alloy, as there is a 30% increase in the cluster number density in commercial alloy relative to the lab-made alloy.

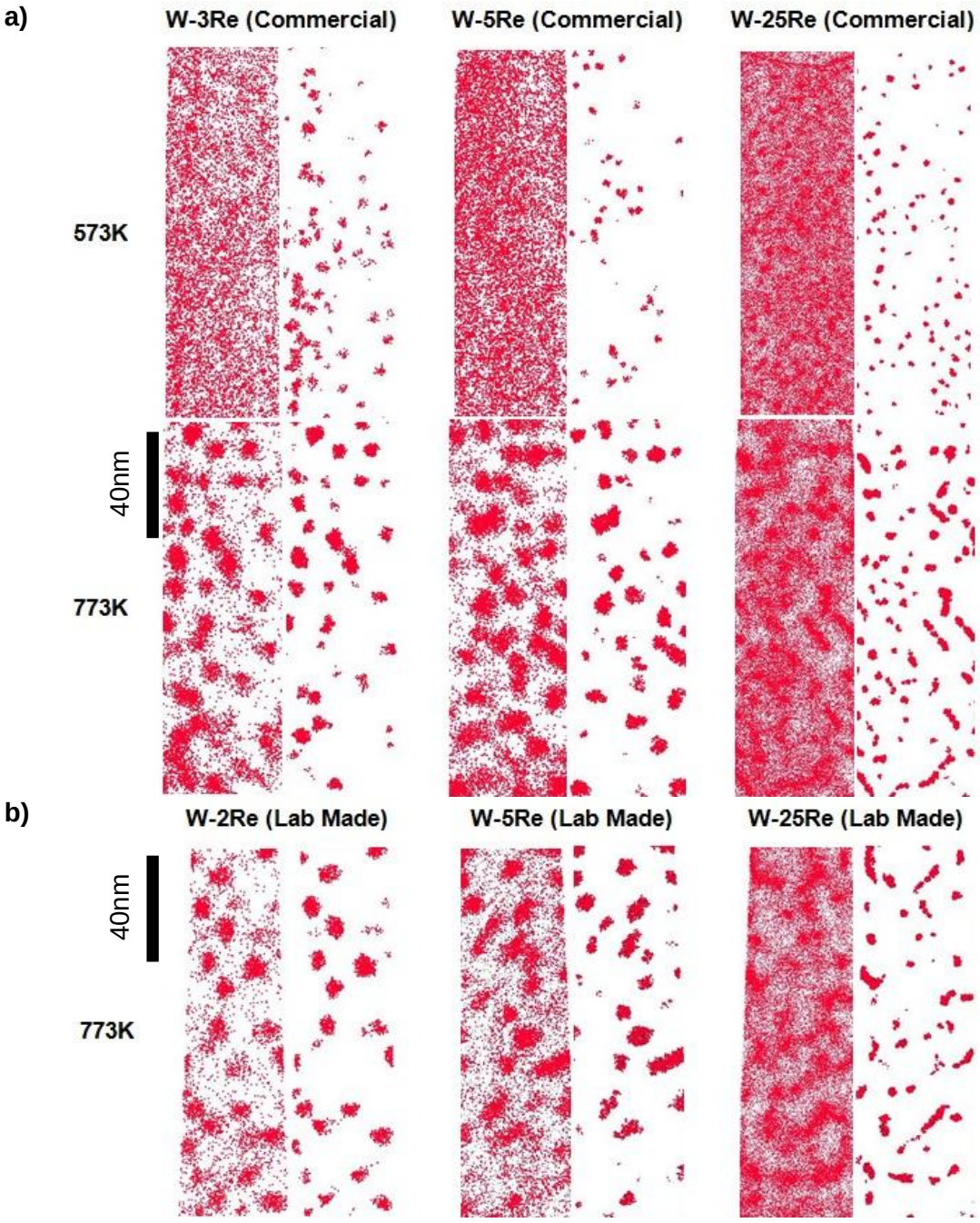

Figure 5.4.1 (a) Atoms maps of commercial W-3Re, W-5Re and W-25Re alloys irradiated to 33dpa at 573 and 773K. (b) Atom maps of lab-made W-2Re, W-5Re and W-25Re alloys irradiated to 33dpa 773K (reproduced from §3.2.2). For each sample, the Re clusters as separated from the matrix is shown alongside the original atom map.

Commercial Wire Alloy Grain Size	33dpa 773K W-3Re 0.5-1μm	33dpa 773K W-5Re 0.5-1μm	33dpa 773K W-25Re 0.5-1μm	33dpa 573K W-3Re 0.5-1μm	33dpa 573K W-5Re 0.5-1μm	33dpa 573K W-25Re 0.5-1μm
Cluster Re (at.%)	18.0±3.9	21.4±3.4	54.6±5.5	9.8±1.7	13.7±2.5	45.9±4.7
Matrix Re (at.%)	2.0±0.1	3.4±0.5	21.9±0.1	2.9±0.1	5.1±0.7	24.2±0.2
Bulk Re (at.%)	3.3±3.0	4.8±3.4	24.5±5.5	3.2±1.7	5.2±2.5	25.0±4.7
Diameter/Length (nm)	5.1±2.6	4.5±2.4	5.0±3.0	3.6±2.0	2.6±1.4	1.8±0.7
Number Density (x1000/μm^3)	1018±52	1284±58	3872±101	1502±81	1190±58	4734±128
Volume Fraction (%)	8.1±0.4	7.6±0.3	8.0±0.2	4.4±0.2	1.7±0.1	3.7±0.1

Table 5.4.1 Averaged cluster composition, radius, number density and volume fraction for commercial wire W-3Re, W-5Re and W-25Re alloys (grain size 0.5-1μm) irradiated at 33dpa 573K and 773K.

Lab-Made Alloys Grain Size	33dpa 773K W-2Re 1-3mm	33dpa 773K W-5Re 1-3mm	33dpa 773K W-25Re 1-3mm
Cluster Re (at.%)	12.8±2.9	19.1±4.0	53.4±5.3
Matrix Re (at.%)	1.2±0.1	3.2±0.5	22.9±0.5
Bulk Re (at.%)	2.3±2.9	4.9±4.0	25.0±5.3
Diameter/Length (nm)	6.6±3.8	5.3±3.4	5.1±3.6
Number Density (x1000/μm^3)	812±54	1010±51	2942±121
Volume Fraction (%)	11.2±0.7	10.4±0.5	6.8±0.3

Table 5.4.2 Averaged cluster composition, radius, number density and volume fraction for lab-made W-2Re, W-5Re and W-25Re alloys (grain size 1-3mm) irradiated at 33dpa 773K (reproduced from §3.2.2).

5.4.2 Cluster Size Distributions after irradiation at 573K and 773K

Cluster size distributions for commercial W-3Re, W-5Re and W-25Re alloys irradiated at 33dpa, 573 and 773K are plotted in Figure 5.4.2. Also shown are size distributions for lab-made W-2Re, W-5Re and W-25Re alloys irradiated to 33dpa at 773K, reproduced from §3.2.5. Each plot is created from 500 – 2000 clusters and normalised to a 1 μm^3 volume. The plots are produced in accordance with methodology detailed in §3.3.5

The higher irradiation temperature of 773K features a higher degree of cluster growth than 573K condition. This is evident in the bimodal cluster size distributions present for all alloys at 773K, while only a single peak is present for each alloy at 573K. At 773K, the bimodal distributions for all alloys extend to 10-12nm diameters, consistently larger than 4-8nm maximum diameters of the single peak distributions at 573K.

At 573K, the distribution peaks are higher than for the 773K distributions, indicating that more clusters have nucleated at the lower temperature. For example, the W-25Re alloy has a peak height of $5.0x10^5$clusters/μm^3 at 773K, an order of magnitude smaller than the peak height at 573K, $1.4x10^6$ clusters/μm^3.

At 33dpa 773K, the shape, peak height and extent of distributions for the commercial alloys are similar to the lab-made alloys. The only difference is distribution size (area under the graph) where the commercial alloys consistently feature slightly larger area than the lab-made alloy.

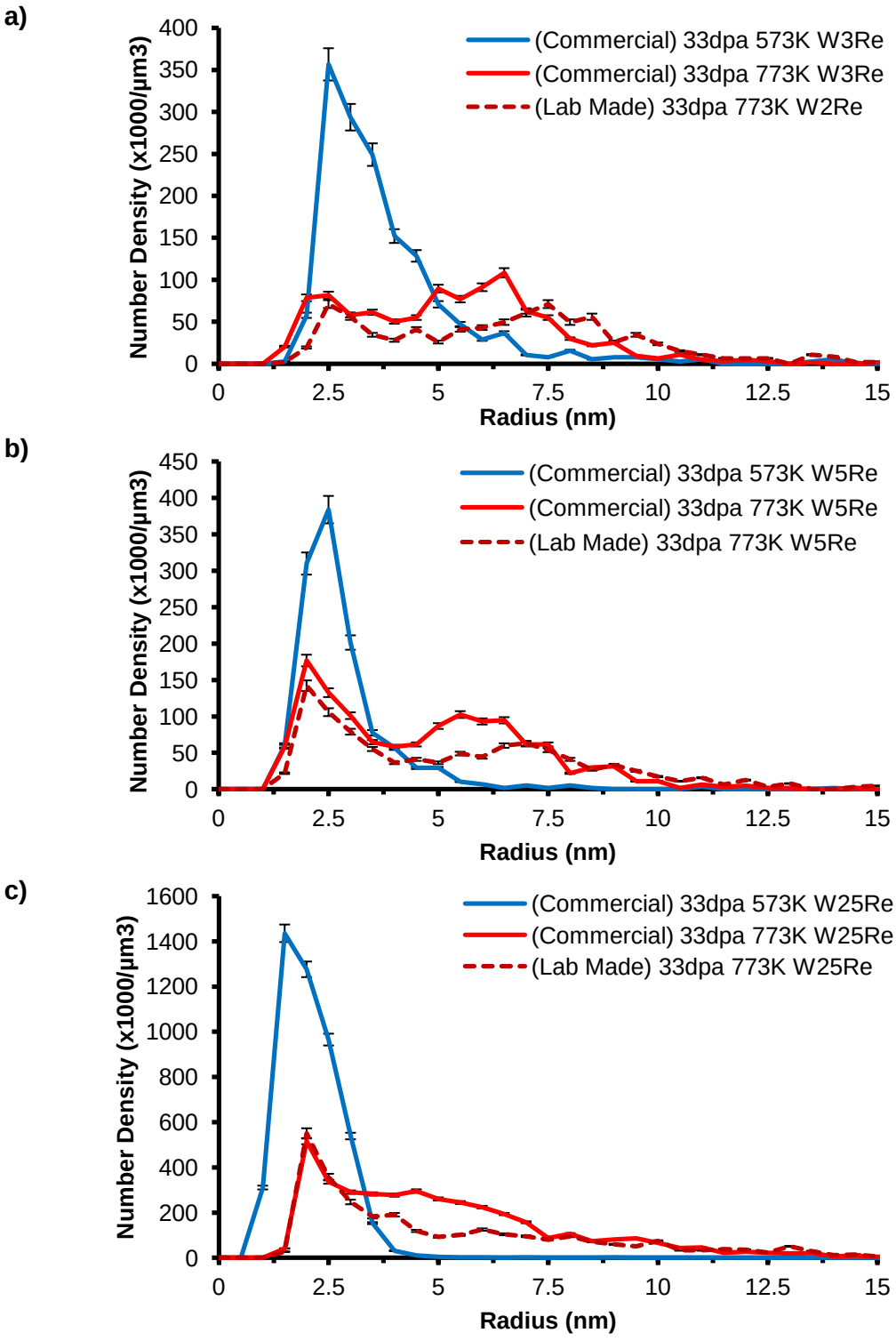

Figure 5.4.2 Cluster size distributions at 33dpa at 573 and 773K for commercial/lab-made alloys of (a) W-2Re and W-3Re, (b) W-5Re and (c) W-25Re alloys. The lab-made alloy data reproduced from §3.2.5.

5.4.3 Proxigram Analysis

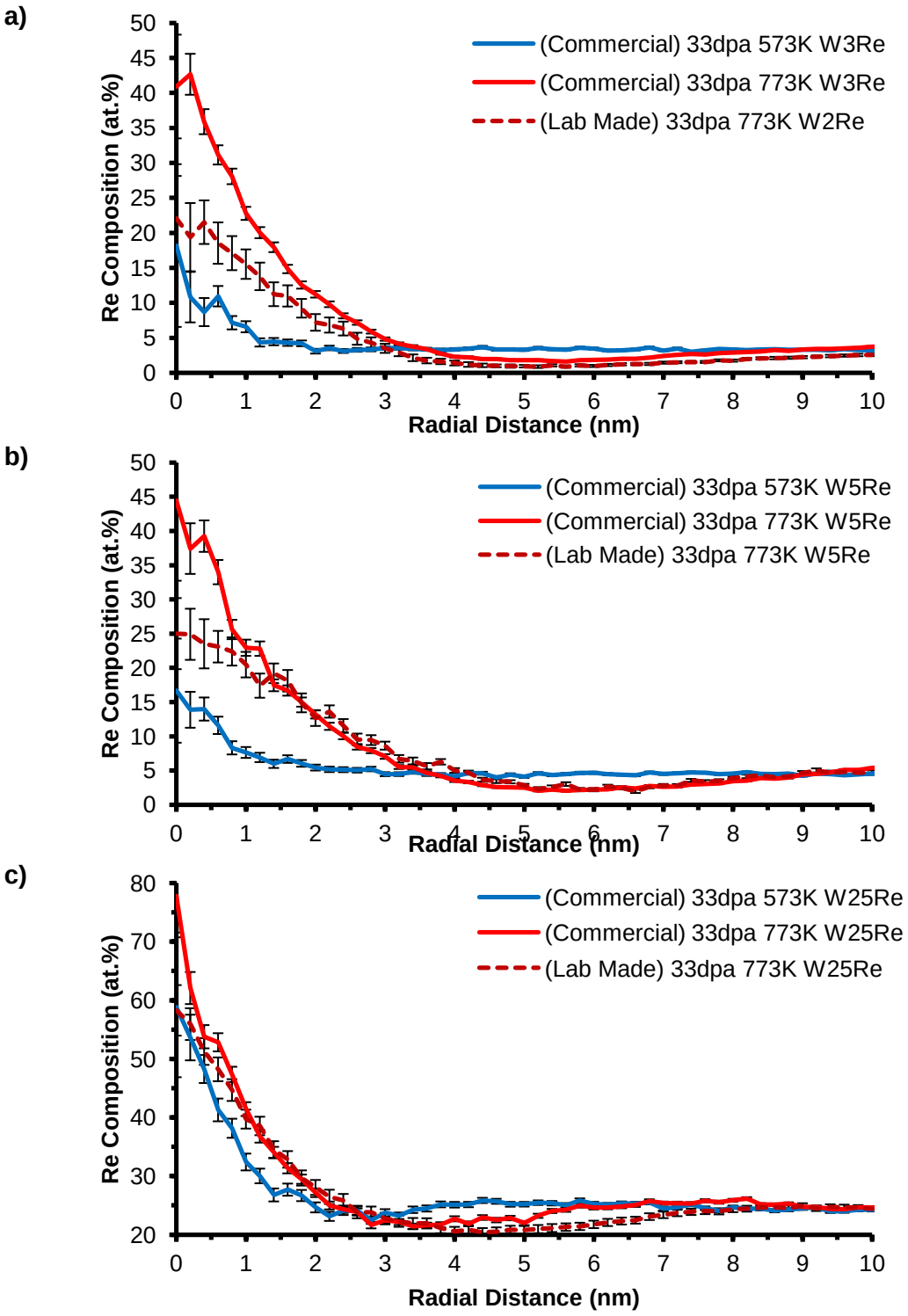

Figure 5.4.3 Proxigram analysis of average sized clusters in commercial/lab-made (a) W-2Re/W-3Re, (b) W-5Re and (c) W-25Re alloys irradiated to 33dpa at 573 and 773K.

The radial compositional profile of the clusters was evaluated through proximity histogram analysis (§4.2.4). Clusters in the commercial and lab-made alloys were identified using iso-surfaces set at 60% of the range of Re composition listed in Table 3.4.1. Figure 5.4.3 shows proxigram plots averaged for 10 median sized clusters for each alloy type: commercial W-3Re, W-5Re and W-25Re alloys irradiated to 33dpa at 573 and 773K and lab-made alloys W-2Re, W-5Re and W-25Re alloys irradiated to 33dpa at 773K. The 0nm value initially set at the interface was shifted it to the cluster centre to simplify scaling.

The higher irradiation temperature introduces a stronger level of solute enrichment in commercial alloys. At 773K, the Re composition at the cluster core is 40at.% for both W-3Re and W-5Re alloys, 2.5 times higher than at 573K. The W-25Re alloy measured 75at.% Re at the cluster centre at 773K compared to 65at.% Re at 573K. A stronger degree of solute segregation takes place as temperature is increased and also as the bulk composition increases.

The smaller grain size in the commercial alloy appears to be linked to a higher cluster core composition as compared to the larger grain sized lab-made alloys. In the W-5Re commercial alloy the core cluster composition is 45at.%Re, twofold higher than the core composition in the lab-made alloy, 27at.%Re. Similarly, the W-25Re commercial alloy has a cluster core composition of 75at.%Re higher than the lab-made alloy by 10at.%Re.

The greater degree of Re enrichment for irradiation at 773K is also accompanied by a large Re depletion zone (where the content drops below the bulk) surrounding the clusters. At 773K, clusters in the W-3Re alloy have local Re content depleted to 1.5at.%. Similarly, the matrix surrounding clusters in W-5Re is depleted to 2.2at.%

while for the W-25Re alloy it is 21at.%. Interestingly, the size of the depletion zone decreases with the bulk Re content. For W-3Re alloy, the depletion zone is 3.5nm long, much greater than in the W-25Re alloy, 2.5nm long.

5.4.4 Discussion – Clustering Across Different Irradiation Conditions

The irradiation temperatures were selected to be at either side of the critical temperature for vacancy activated migration, 743K [113]. In theory, the 573K temperature should therefore induce a self-interstitial driven cluster formation while 773K should be vacancy dominated. Assuming this to be true, the experimental results show vacancies promote a stronger degree of cluster formation than self-interstitials. It is evident when considering the cluster chemistry, size and volume fraction which is consistently higher at 773K. Clusters formed in commercial alloys at 773 K featured a higher volume fraction in the range of 7-9at.% compared to 2-4% at 573K. The cluster size distributions in Figure 5.4.2 showed at 773K, vacancies promoted cluster growth resulting in larger diameter or lengths compared to 573K. The lab-made W-2Re alloy irradiated to 33dpa 573 and 773K mirrored this behaviour. In §4.2.3, the cluster volume fraction of W-2Re is 11.2% at 773K compared with 7.3% at 573K. However, this trend is only apparent at a high damage level of 33dpa. At 1.2dpa 573 and 773K in commercial W-25Re alloy (§5.2.1), the lower temperature featured a greater cluster volume fraction.

A difference in clustering behaviour is evident when comparing commercial alloys with lab-made alloys. Commercial alloys have smaller grain size of 0.5-1.0μm diameter compared to 0.5-3mm diameter grains in the lab-made alloy. The cluster size distributions in Figure 5.4.2 show the commercial alloy to have a greater

number density than the lab-made alloys, especially at 5-7.5nm diameter range. For all three compositions studied, more clusters have nucleated in the commercial alloys, where the grain size is smaller. Additionally, the proxigrams in Figure 5.4.3 show that the core Re composition in the clusters of commercial W-3Re, W-5Re and W-25Re alloys are consistently 20at.% higher than the core composition of the lab-made alloys. Thus, smaller grain size is correlated with more enriched clusters. To explain these trends, it is possible the larger defect sink afforded by having smaller grain size reduced self-interstitial defect population, minimising annihilation of vacancies. This hypothesis is consistent with findings at 573K in § 5.3, where smaller grain sized samples also had a lower cluster number density.

The cluster diameter and number density data is used to derive the inter-cluster spacing at 33dpa 773K for the commercial wire and lab-made plate alloys. In Table 5.4.3, the cluster spacing is calculated by approximating the clusters to be spherical and homogeneously distributed. The only issue is rod shaped cluster in the W-25Re alloys and they are also roughly approximated as spherical clusters in Table 5.4.3. The radius is calculated from the average volume of the rod shaped clusters. Using the cluster radius and number density values in Table 5.4.1&5.4.2 the cluster spacing is calculated by the following equation 5.4.1.

$$Cluster\ spacing = \left(\frac{1}{Cluster\ number\ density}\right)^{\frac{1}{3}} \quad \text{Eqn (5.4.1)}$$

The average diffusion distance is then calculated from the cluster spacing using equation 5.4.2 below. Here we assume the distance from the midpoint between clusters to the outer periphery of the cluster to be average distance solutes travel.

$$Diffusion\ Distance\ = \frac{1}{2}[Cluster\ Spacing - (2\ \times Cluster\ Radius)] \quad \text{Eqn (5.4.2)}$$

The diffusivity of the cluster is calculated using relationship shown in equation 5.4.3 below as derived from Fick's first law. The "q" value is the dimensionality constant taken as 6 and t is the total time equated as the total irradiation time 91494 seconds.

$$(diffusion\ distance)^2 = q \times D \times t \quad \text{Eqn (5.4.3)}$$

The last column of Table 5.4.3 is the diffusivity as estimated using the Lescoat et al [139] method which assumes clusters to be defect sinks. The parameters and analysis methods are detailed in §4.2.5.

	Cluster Radius (nm)	Cluster Number Density (µm-3)	Cluster Spacing (nm)	Diffusion Distance (nm)	Diffusivity (equation 5.4.3) (m2/s)	Diffusivity (ref [139]) (m2/s)
(Commercial) W3Re	2.6	1.02×10^{6}	9.9	2.4	1.07×10^{-23}	5.18×10^{-26}
(Commercial) W5Re	2.3	1.28×10^{6}	9.2	2.4	1.01×10^{-23}	4.65×10^{-26}
(Commercial) W25Re	1.8	3.87×10^{6}	6.4	1.4	3.69×10^{-24}	1.97×10^{-26}
(Lab-Made) W2Re	3.3	8.12×10^{6}	10.7	2.1	7.73×10^{-24}	4.99×10^{-26}
(Lab-Made) W5Re	2.7	1.01×10^{6}	10.0	2.3	9.92×10^{-24}	5.02×10^{-26}
(Lab-Made) W25Re	1.9	2.94×10^{6}	7.0	1.6	4.49×10^{-24}	2.37×10^{-26}

Table 5.4.3 Estimation of Re diffusivity from mean diffusion distance for commercial wire and lab-made plate W-Re alloys. Also listed in this table corresponding diffusivity of Re for W-Re alloys calculated using the Lescoat et al [139] method detailed in §4.2.5.3.

The double of the diffusion distance yields ~4.2-4.8nm for W-2Re, W-3Re and W5Re (commercial and lab-made) alloys. It matches the depletion zone: ~5nm measured from the proxigrams in Figure 5.4.3a-b). Similarly, the double of the diffusion distance for W-25Re alloy (commercial and lab-made) is ~3nm same as the depletion zone size as noted in the proxigrams in Figure 5.4.3c). The close

match between the diffusion distance and depletion zone size show it is linked with the cluster number density. The higher cluster number density in the W-25Re thus brought about the smaller depletion zone.

The diffusivity values are calculated by two different means in Table 5.4.3. The diffusivity values as calculated from the diffusion distance is 2-3 orders of magnitude greater than the diffusivity as determined from the Lescoat et al method [139]. Both values are much higher than the thermodynamic value for Re at 773K: 2.0×10^{-44} $m^2 s^{-1}$ (§4.2.5.3). So relative to the expected equilibrium diffusion value, calculated irradiation enhanced diffusivities are realtively similar. Further, the diffusivity is consistently higher in commercial wire than the lab-made alloys. It suggests the smaller grain size in the commercial wire samples has increased the diffusivity of Re and act as a defect sink. It reinforces statements made ealier.

5.4.5 Discussion – Irradiation Hardening of Commercial W-Re Alloys

Hardness of commercial wire W and W-Re alloys before and after irradiation are plotted in Figure 5.4.7; data provided by David Armstrong (personal communication). W shows negligible degree of irradiation hardening compared to the alloys, as the error bars of irradiated samples overlap with the non-irradiated sample. As no clusters are present in W, the slight hardening is most likely due to vacancy clusters and dislocation loops which have a smaller hardening effect [73-75].

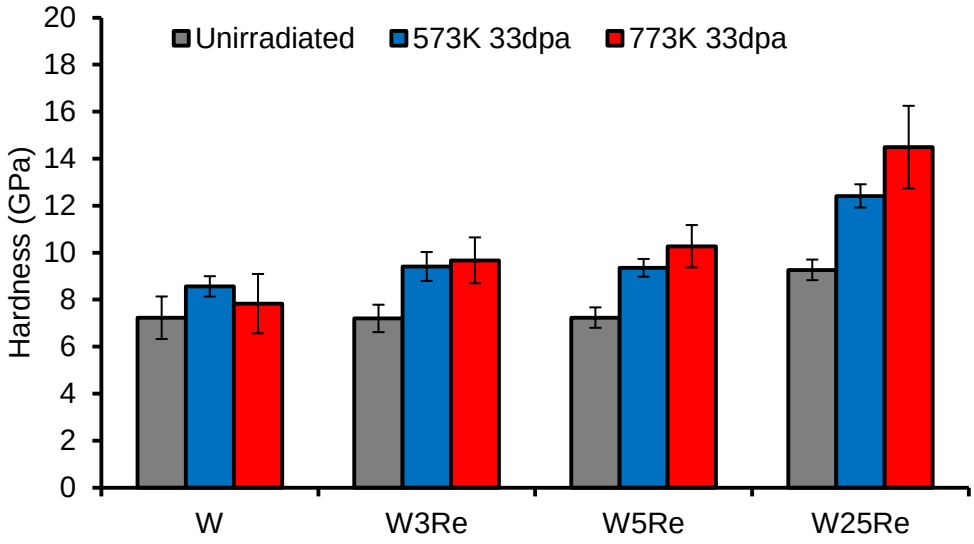

Figure 5.4.7 Hardness at 125 nm depth of W, W-3Re, W-5Re and W-25Re; unirradiated and at 33dpa 573 and 773 K.

The irradiation hardening of the commercial W-Re alloy increases with the bulk Re content. At 773K, the W-25Re alloy hardened by 5GPa, twice as high as in the W-3Re alloy. Similarly, at 573K, the W-25Re experienced a hardening of 3GPa compared to 2GPa for W-3Re. The bulk Re content and cluster number density varied the most with irradiation hardening so they are plotted against irradiation hardening in Figure 5.4.8 to search for correlations. A linear relationship was assumed which quantifies the clear and strong link between bulk Re content and irradiation hardening as well as cluster number density and irradiation hardening.

The irradiation hardening of W-1Re-1Os alloys at 33dpa 773K from §4.2.5 are also plotted in Figure 5.4.8a-b). In Figure 5.4.8a), the irradiation hardening of the W-1Re-1Os alloy is highest even though it has a low Re content. The deviation due to Os presence is attributed to its higher cluster number density as Figure 5.4.8b) shows a closer correspondence with the trend lines for W-Re alloys at 33dpa 773K.

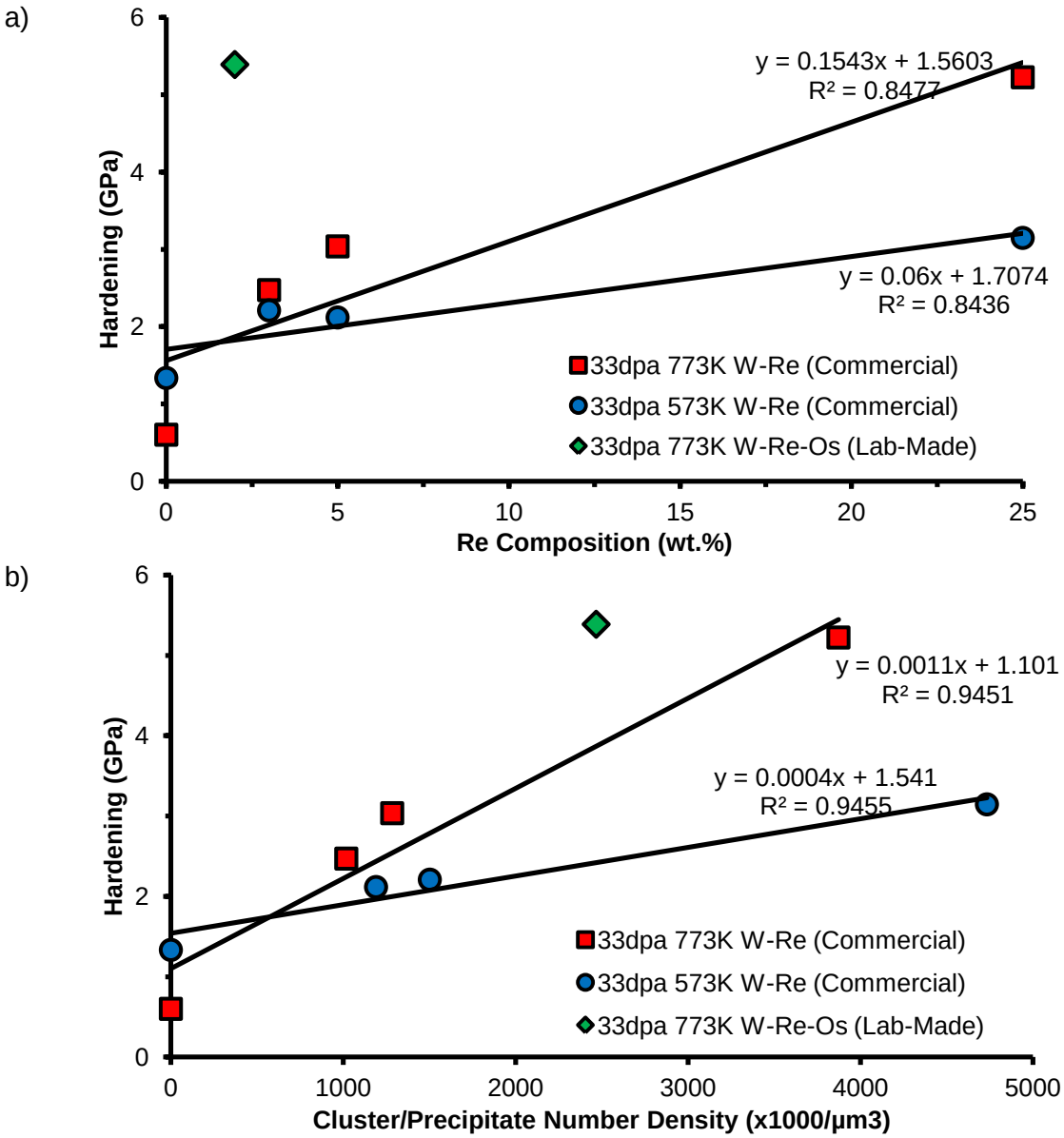

Figure 5.4.7 (a) Bulk Re content and (b) Cluster number density plotted against irradiation hardening for 33dpa and 573/773K in all commercial W-Re alloys. The W-Re-Ta and W-Re-Os alloy at 33dpa 773K from §4 are also plotted.

5.5 Chapter Summary

A thorough investigation was undertaken to quantify the effect of free surface, grain size, dislocation density, and temperature on the cluster formation and its hardening response. They are summarised in the following points:

- Free surface alters the clustering behaviour at 1.2dpa at 573 and 773 K by acting as a defect sink. However, difference is mostly the number density and volume fraction as discerned quantitatively in §5.2.1-5.2.2.
- Whilst both grain boundaries and dislocations hinder cluster development, grain boundaries have a greater influence (Table 5.3.1). Whilst more work is needed to understand dislocations, I hypothesised grain boundaries act as a defect sink for interstitials reducing the amount of clusters nucleated (§5.3.4).
- Irradiation enhanced Re grain boundary segregation was observed. Whilst there is minimal difference between annealed and unannealed states, the larger grain sized (plate) sample featured greater Re enrichment. This effect is attributed to the relatively smaller area for Re segregation (§5.3.5).
- The bulk Re content is positively correlated with the cluster number density and cluster composition and negatively correlated with cluster size (volume). This trend is evident across different grain size, temperature and dose (§5.4.5).
- The irradiation hardening of commercial wire alloys show a positive correlation with cluster bulk Re content and number density (§5.4.6). Comparison of hardening data with W-Re-Os alloy further confirmed the dependency of hardness on cluster number density.

6. Summary and Conclusions

Radiation induced precipitation is an inevitable phenomenon detrimental to tungsten plasma facing components operating within fusion reactors. This thesis investigated irradiation induced clustering brought about by the presence of key transmutation species. Three major aspects were explored: evolution of Re clusters, Os and Ta clustering and effect of microstructural (grain size and dislocation) and environmental variables (dose and temperature).

The effect of dose and bulk Re content on cluster formation was investigated first. W-xRe alloys (x: 2, 5, 10, 25at.%)) were irradiated under doses 1.2, 3.9 and 33dpa at 773K. It was found cluster size, composition and volume fraction progressively increases with dose. The cluster nucleation and growth mechanics also change with dose. At 1.2 and 3.9dpa, more clusters have nucleated relative to 33dpa condition which involves a greater degree of cluster growth. Between the low dose (1.2 and 3.9dpa) and high dose (33dpa), cluster development is suspected to be brought about by a combination of Ostwald ripening and joining of individual clusters. This was observed consistently across all alloys and shows cluster formation is promoted by radiation enhanced point defect population. At the same time, I acknowledge a longer irradiation time also could help promote cluster formation. This can be investigated by analysing in clusters within samples exposed to differing dose rates.

At the highest damage level alone, increased bulk Re content was found to be correlated with a high cluster number density. Higher bulk Re content alloys have more Re for segregating to cluster nucleation points (vacancy cluster). Thus, the correlation supports the hypothesis of clusters evolving from nano-voids due to Re being attracted to vacancies. Additionally, rod shaped clusters form in W-25Re alloy

only, having <110> orientation and in coexistence with spherical clusters. The rod clusters resemble Chi phase precipitates in neutron irradiation experiments [46] and have similar composition to them too. They reveal a transition from clusters to precipitates is taking place.

The clustering behaviour was related to their measured irradiation hardening. Nanomechanical tests showed W-Re alloys go through an initial stage of dislocation hardening followed by cluster hardening. At 1.2 and 3.9dpa, dislocation hardening is dominant because the clusters are too small and sparse to affect mechanical properties strongly.

This thesis also investigated the clustering behaviour of transmutation species: Ta and Os. At 33dpa at 573K and 773K, it seemed that Ta has no tendency to form clusters in W-Ta binary alloys and is expelled from Re clusters in the W-Re-Ta ternary. It is not thermodynamically favourable for Ta to form clusters. The presence of Ta is correlated with a reduced cluster number density, volume fraction and irradiation hardening. Despite this, Ta still has a strong solid solution hardening effect that may embrittle the material.

Os was found to have the opposite effect on irradiation clustering behaviour compared to Ta. At both temperatures, clusters formed in the W-Re-Os ternary are predominantly enriched in Os. At 773K, there is a twofold higher cluster number density for the W-Re-Os alloy relative to the W-Re alloy, due to it being more energetically favourable for Os to segregate than Re. The strongest degree of irradiation hardening occurred in the W-Re-Os alloy followed by the W-Re and W-Re-Ta alloy. The hardening is partly correlated with cluster number density which is especially high in the W-Re-Os alloy and lowest in the W-Re-Ta alloy.

For all the alloys investigated thus far, the clusters induced are all coherent with the matrix and appear to be solute segregations. This was proven through atom probe lattice imaging as well as mathematical models: Friedel Relations. Clusters in W-Re, W-Re-Ta and W-Re-Os alloys all cause dislocations to subtend by similar angle of ~80^{o} indicating they offer minimal resistance individually.

The final aspects investigated were the effect of free surface, dislocation density, grain size and temperature on Re cluster formation. Two sample forms of: needle and bulk were irradiated to 1.2dpa at 573 and 773K. The measured cluster number density and size was much greater in the needle at 573K relative to the bulk while the reverse trend was evident at 773K. The defect sink provided by free surface of needle reduced the self-intersitial population at 573K minimising the amount of annihilation with vacancies. At 773K, where vacancies are mobile, the loss of vacancies to free surface brought about smaller cluster number density. These are merely hypotheses and further computational modelling is needed to validate this.

To understand the impact of dislocations and grain size on cluster formation, commercial W-5Re alloys of plate form (large grain size 4-10µm diameter) and wire form (small grain sizes 0.5-1µm) and in annealed and unannealed state were irradiated at 33 dpa 573K. A reduced cluster volume fraction was measured where the dislocation density was high and grain size was small. This showed both dislocations and grain boundaries act as defect sinks hindering cluster formation. Of the two variables, grain boundaries have the greatest effect.

To determine the effect of self-interstitials and vacancies on cluster formation, commercial wire W-3Re, W-5Re and W-25Re alloys (0.5-1µm diameter grain size) were irradiated to 33 dpa at 573 and 773K, above and below the vacancy activation

temperature 743K [113]. A consistently lower density of clusters, having smaller degree of Re enrichment, were formed at 573K. Further, through comparing clusters in these commercial alloys at 773K with clusters in lab-made W-Re alloys (1-3mm diameter grain size) at 33dpa 773K, commercial alloys consistently feature a greater cluster number density and higher core Re content. Thus, the smaller grain size in commercial alloys increases the degree of clustering at 773K. It is suspected; the loss of interstitials at 773K to grain boundaries avoided loss of vacancies to annihilation and promoted cluster formation.

To summarise all the data obtained throughout this thesis, Figure 5.4.5a-b) plots the cluster number densities across the commercial and lab-made alloys for various irradiation conditions covered in this thesis. Only at high dose of 33dpa, the bulk Re composition appears to be directly correlated with the cluster number density. This trend is evident at both temperatures 573 and 773K and is true for commercial wire (small grain size, 0.5-1μm diameter) and lab-made (large grain size, 1-3mm diameter) alloys. The trend is also comparable with neutron irradiation experiments by Tanno et al [46]. At 1.54dpa and 1023K, the measured precipitate number density in a W-10Re alloy is $4.2x10^{22}m^{-3}$, an order of magnitude greater than that in the W-5Re alloy at $0.7x10^{22}m^{-3}$. Overall, bulk Re composition is positively correlated with cluster number density at high damage levels. It is repeatable across different temperatures, grain sizes and types of irradiation.

The averaged cluster composition is plotted against the bulk Re content in Figure 5.4.6a-b) for commercial and lab-made alloys irradiated in all conditions considered in this thesis. In commercial and lab-made alloys at 33dpa and 773K, the cluster compositions are very similar. The difference in grain size between them has no effect on the cluster chemistry. The effect of bulk Re content, dose and temperature

is also evident in this figure, as it increases the degree of cluster enrichment. The cluster Re content is 2–5 times greater than the bulk Re content for all irradiation conditions. The cluster composition for commercial wire alloys at 33dpa 773K is higher than commercial wire alloys at 33dpa and 573K. Similarly, the cluster composition in lab-made alloys at 33dpa 773K is also consistently ~8at.%Re higher than the lab-made alloys at 1.2 and 3.9dpa 773K. Overall, only the grain size has minimal effect on cluster composition.

To compliment the number density plots in Figure 5.4.6a-b), the average cluster volume is plotted against the bulk Re content in Figure 5.4.7a-b) for commercial and lab-made alloys at various irradiation conditions. The average cluster volume decreases exponentially with the bulk Re content regardless of the dose, grain-size or irradiation temperature. The trend is reverse of that for number density and bulk Re content. The results are consistent with data in Table 5.4.1-5.4.2.

A higher irradiation temperature, dose and grain size appears to increase the cluster volume (size). Between the temperatures 573 and 773K, Figure 5.4.7a) shows higher temperature enhances the cluster size by factor of 2-4. In Figure 5.4.7b), increased dose from 1.2 to 33dpa also enhances cluster size by same factor. Comparing between commercial and lab-made alloys at 33dpa 773K, the lab-made alloys having a larger grain size (diameter 1-3mm) has a cluster volume twofold higher than commercial alloys of smaller grain size (diameter 0.5-1μm).

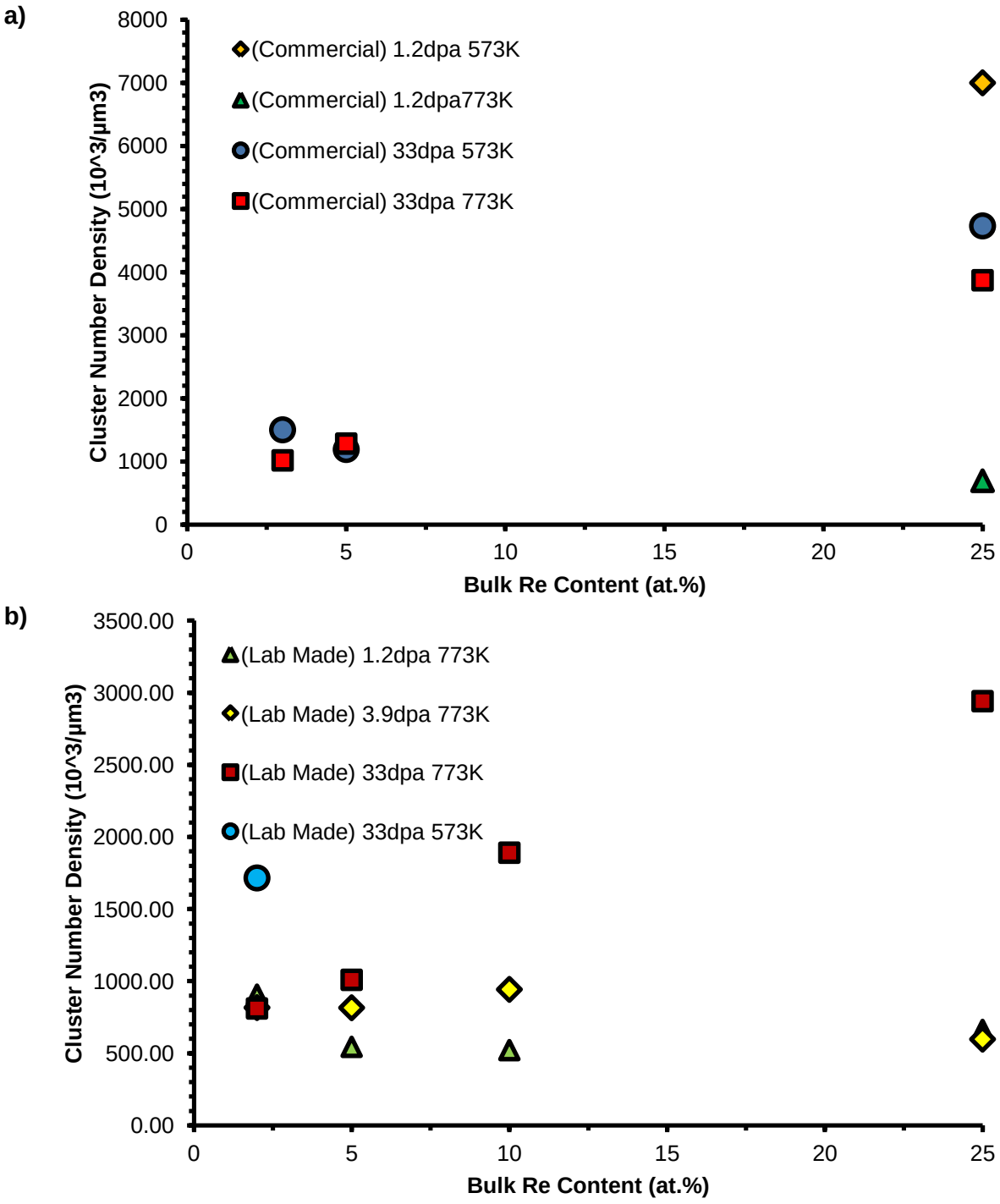

Figure 5.4.5 Cluster number density of irradiated W-Re alloys plotted against bulk Re Content for a range of irradiation conditions in (a) commercial (diameter 0.5-1µm) and (b) lab-made alloys (diameter 1-3mm).

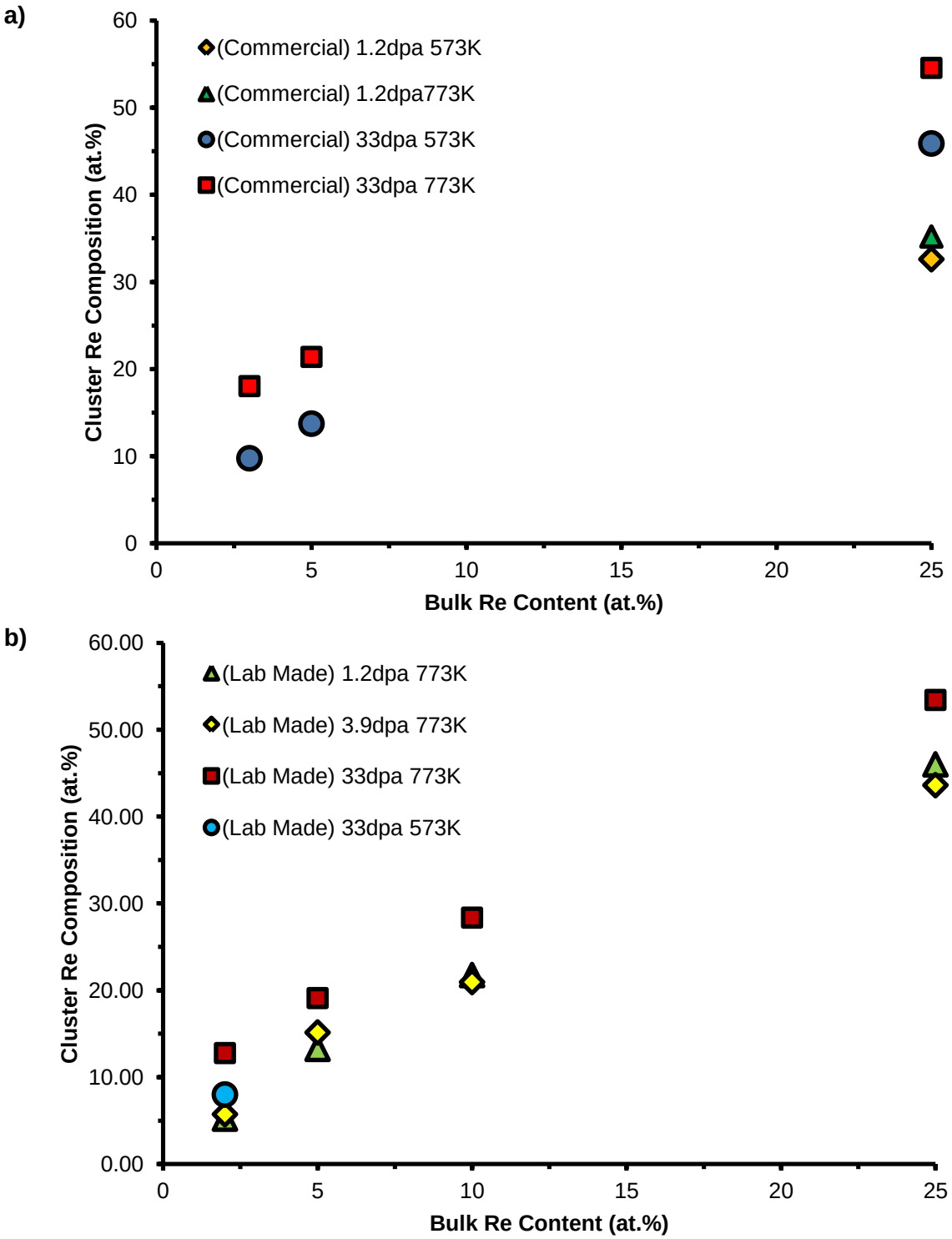

Figure 5.4.6 Averaged cluster composition of irradiated W-Re alloys plotted against the bulk Re content for a range of irradiation conditions in (a) commercial and (b) lab-made alloys.

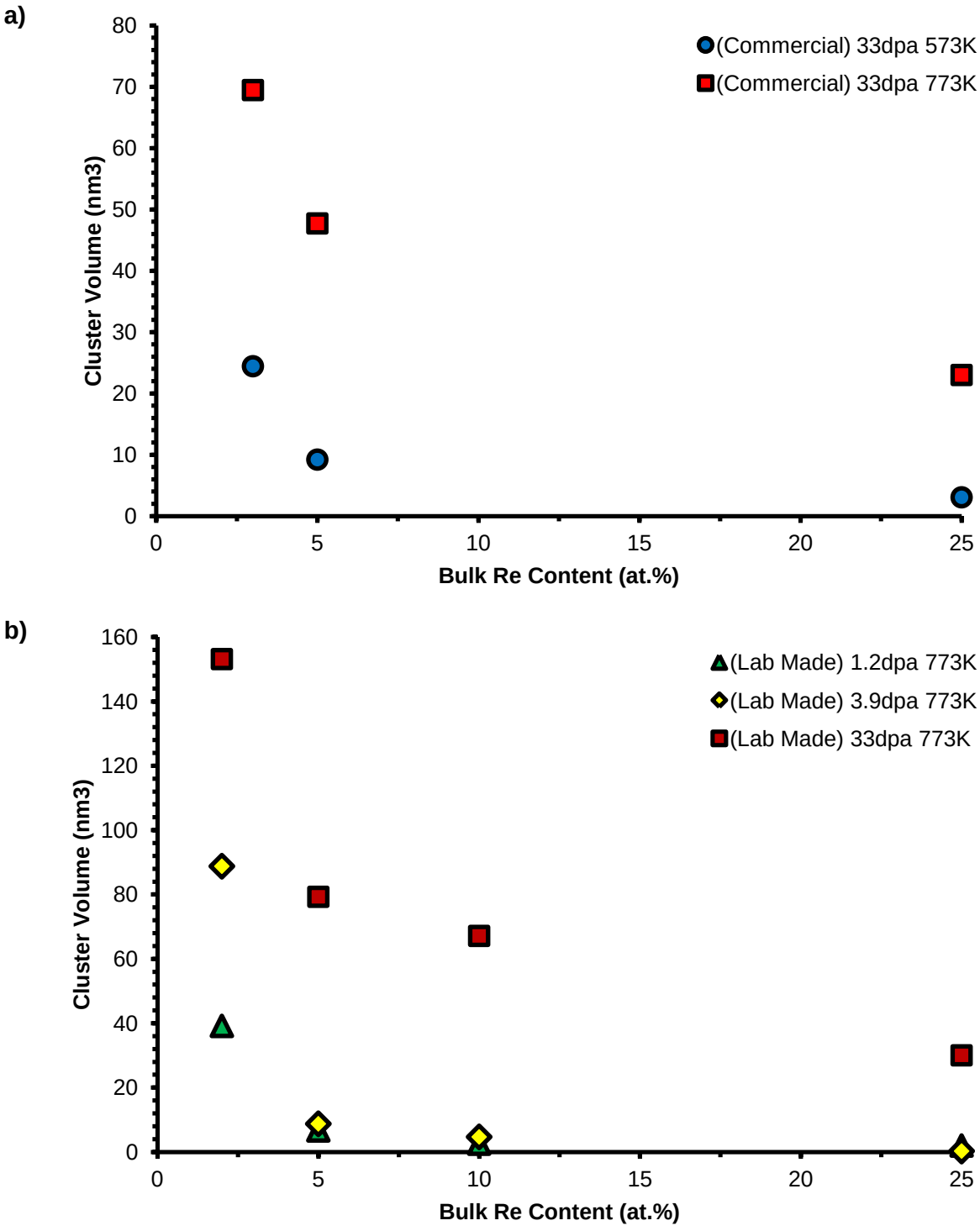

Figure 5.4.7 Averaged cluster volume of irradiated W-Re alloys plotted against the bulk Re content for a range of irradiation conditions in (a) commercial and (b) lab-made alloys.

In the context of fusion reactors, the cluster compositions all studied here offer close approximation of the transmutation path expected and clues as to improving plasma facing component lifetime. For the DEMO fusion reactor, the W-Re-Ta and W-Re-Os alloy composition used here are similar to that expected in tungsten plasma facing components after 5 years of reactor operation [18, 19]. The analysis performed here shows Os and Ta have strong effect on clustering behaviour. Ta has most positive effect as it reduces the degree of cluster formation and thus irradiation hardening. On the other hand, studying W-2Re, W-5Re, W-10Re and W-25Re mirrors the Re transmutation species formed as operating times increase from 5 years to 15 years. Cluster number density increases as bulk Re content increased which also enhanced the degree of irradiation hardening. It suggests the precipitation embrittlement will only accelerate over time.

To remedy the effect of Os presence and increased Re content, it would be ideal to use a W-5Ta alloy instead of pure tungsten as it would delay the rate of Re transmutation and their clustering. W-5Ta does have inherently poor mechanical properties as noted by Armstrong et al and Rieth et al [106, 108] but compared to the irradiation hardening from Re and Os presence, it is still negligible. Further, Gilbert et al [18, 19] simulated the transmutation species after 5year of operation in fusion power plant for a W-30Ta alloy. The composition expected after transmutation is W-19Ta-2.67Re very different from what is expected for pure tungsten: W-3.80Re-1.38Os. Additionally, for components operating below the vacancy activation temperature 743K [113], it would be best to use a heavily dislocated and small grain sized sample as they act as effective defect sinks for hindering cluster formation. Above 743K, samples with large grain size would be better suited as relatively less clusters form.

7. Future Work

More investigation is necessary to verify, validate and explore some areas of the thesis that are still unclear. Hence future avenues of further research are listed below:

FIM imaging: The limitation of the atom probe model used is that it has a low detection efficiency of 37%, which along with field aberrations could introduce a certain degree of inaccuracy in the measurement of cluster size/composition and even evade detection of smaller clusters. I would suggest validating the atom probe measurements acquired in this chapter by analysing the same clusters in a 3DAP Field Ion Microscope (FIM). This can image 100% of atoms on the needle surface. FIM imaging of Re clusters could put to rest some of the doubts that still exist in this thesis surrounding the cluster behaviour, in particular, cluster structure.

Exposing W-Re alloys to higher doses: To understand better how the clusters develop into precipitates it is still necessary to irradiate W-Re to higher doses, e.g. of 66dpa or 99dpa. A future experiment would be to irradiate the alloy to such doses at 773K to reveal how the clusters transition into precipitates, which is currently unknown. Collaborations can be developed with Oak Ridge to compare the spherical and needle precipitates in neutron irradiated with the ion irradiation induced clusters.

W-Re-Os-Ta alloys: There is still very little known about the effect of Ta and Os together. The most obvious analysis would be to irradiate W-2Re-1Os-1Ta alloy at 33dpa and 773K and compare with the data already available in this thesis. Additionally its essential to understand how increasing the amount of Os or Ta affects Re clustering so alloy compositions with higher Os and Ta contents should

also be included. In particular, W-Os binary alloys should be investigated alongside the ternary alloys as well.

W-Re ODS alloys: In the final results chapter, it was found that hindering point defects could reduce the cluster formation taking place. It would be interesting to investigate W-Re alloys with nanosized ODS particles which could potentially act as defect sinks just like it does for steels. A W-Re-ODS alloy would be exposed to 33 dpa 773K and determine the extent of clustering when compared with a W-Re alloy.

Annealing of samples: There are no experimental data to date that show the stable phase at temperatures below ~1273K. It is difficult to know with 100% certainty whether the clusters formed under irradiation are thermodynamically stable phases or not. Annealing the samples at ~1000K can determine the stability of the phases under thermodynamic conditions.

8 References

1. Agency, T.I.E., *Key world energy statistics*. 2014: http://www.iea.org/publications/freepublications/publication/key-world-energy-statistics-2014.html. p. 82.

2. Scientists, U.o.C. *The hidden costs of fossil fuels*. 2015 [cited 2015.

3. Agency, U.S.E.P. *The sources and solutions of fossil fuel*. 2015 [cited 2015.

4. McCracken, G. and P. Stott, *Fusion: the energy of the universe*. 2005, London: Elsevier Academic Press. 186.

5. Derek, S., *DEMO (Fusion Workshop Presentation)*. 2012, Culham Centre for Fusion Energy. p. 21.

6. Zinkle, S.J., *Advanced materials for fusion technology.* Fusion Engineering and Design, 2005. **74**: p. 31-40.

7. Zinkle, S.J. and J.T. Busby, *Structural materials for fission & fusion energy.* Materials Today, 2009. **12 (Issue 11)**: p. 12-19.

8. Baluc, N., *materials for fusion power reactors.* Plasma Physics and Controlled Fusion, 2006. **48**: p. B165-B177.

9. Bolt, H., et al., *materials for the plasma-facing components of fusion reactors.* Journal of Nuclear Materials, 2004. **329-333**: p. 66-73.

10. Butterworth, G.J., *Low activation structural materials for fusion.* Fusion Engineering and Design, 1989. **11**: p. 231-244.

11. Armstrong, D.E.J., et al., *Hardening of self ion implanted tungsten and tungsten 5-wt% rhenium.* Journal of Nuclear Materials, 2013. **432**: p. 428-436.

12. Marquis, E.A., et al., *Nuclear reactor materials at the atomic scale*, in *Materials Today*. 2009, Elsevier. p. 30-37.

13. Tomabechi, K., *International Thermonuclear Experimental Reactor, ITER.* Fusion Engineering and Design, 1989. **8**: p. 43-49.

14. Davis, J.W., et al., *Assessment of tungsten for use in the ITER plasma facing components.* Journal of Nuclear Materials, 1998. **258-263**: p. 308-312.

15. Griffith, S. *iter divertor under final review (http://www.iter.org)*. 2012 [cited 2012 11 April].

16. Antusch, S., et al., *Powder injection molding - an innovative manufacturing method for he-cooled DEMO divertor components.* Fusion Engineering and Design, 2011. **86**: p. 1575-1578.

17. Lasser, R., et al., *structural materials for DEMO: the EU development, strategy, testing and modelling.* Fusion Engineering and Design, 2007. **82**: p. 511-520.

18. Gilbert, M.R. and J.-C. Sublet, *neutron-induced transmutation effects in W and W-alloys in a fusion environment.* Nuclear Fusion, 2011. **51**(043005): p. 13.

19. Gilbert, M.R., et al., *An integrated model for materials in a fusion power plant: transmutation, gas production, and helium embrittlement under neutron irradiation.* Nucleear Fusion, 2012. **52**(083019): p. 12.

20. Raj, B., et al., *Challenges in materials research for sustainable nuclear energy.* MRS Bulletin, 2008. **33**: p. 327-337.

21. *the virtual vessel (http://www.efda.org/2011/08/the-virtual-vessel-5/?view=gallery-264)*. 2011 [cited 2012.

22. *limiters and divertors: the concept (http://www.efda.org)*. 2012 [cited 2012 11 April].

23. Sakurai, S., et al., *design study of plasma-facing components for JT-60SA.* Fusion Engineering and Design, 2007. **82**: p. 1767-1773.

24. Xu, Q., N. Yoshida, and T. Yoshiie, *dynamic simulation of multiplier effects of helium plasma and neutron irradiation on microstructural evolution in tungsten.* Materials Transaction, 2006. **46**: p. 1255-1260.

25. Merola, M. *Japanese domestic agency pushes divertor technology (https://www.iter.org/newsline/152/478)*. 2010 [cited 2015.

26. Energy, F.f. *F4E signs the procurement arrangement on divertor cassette integration (http://fusionforenergy.europa.eu/mediacorner/newsview.aspx?content=594)*. 2012 [cited 2015.

27. Hasegawa, A., et al., *Property change mechanism in tungsten under neutron irradiation.* Journal of Nuclear Materials, 2011. **417**: p. 491-494.

28. Hasegawa, A., et al., *Neutron irradiation effects on tungsten materials.* Fusion Engineering and Design, 2014. **89**: p. 1568-1572.

29. Fukuda, M., et al., *Microstructural development of tungsten and tungsten-rhenium alloys due to neutron irradiation in HFIR.* Journal of Nuclear Materials, 2014. **455**: p. 460-463.

30. Yih, S.W.H. and C.T. Wang, *Tungsten: sources, metallurgy, properties and applications*. 1979, New York: Planum Press. 500.

31. Rieck, G.D., *tungsten and its compounds*. 1967, Oxford, UK: Pergamon Press. 138.

32. Keys, L.K., J.P. Smith, and J. Moteff, *Stage III recovery in neutron irradiated tungsten.* Scripta Metallurgica, 1967. **1**: p. 71-72.

33. Keys, L.K. and J. Moteff, *Neutron irradiation and defect recovery of tungsten.* Journal of Nuclear Materials, 1970: p. 260-280.

34. Raffo, P.L., *Yielding and fracture in tungsten and tungsten -rhenium alloys*, N.A.a.S. Administration, Editor. 1968, National Aeronautics and Space Administration: Lewis Research Center, Cleveland, Ohio, USA. p. 39.

35. Tran-Huu-Loi, et al., *Brittle fracture of polycrystalline tungsten.* Journal of Materials Science, 1985. **20**: p. 199-206.

36. Rieth, M. and A. Hoffmann, *Influence of microstructure and notch fabrication on impact bending properties of tungsten materials.* International Journal of Refractory Metals and Hard Materials, 2010. **28**: p. 679-686.

37. Villars, P., A. Prince, and H. Okamoto, *Handbook of Ternary Alloy Phase Diagrams: Mg-Ni-P to Y-Zn-Zr*. 1995: ASM International.

38. Mundy, J.N., et al., *Self-diffusion in tungsten.* Physical Review B, 1978. **18**(12): p. 6566-6575.

39. Neumann, G. and C. Tuijn, *Self-Diffusion and Impurity Diffusion in Pure Metals*. Pergamon Materials Series. 2009, United Kingdom: Elsevier. 350.

40. Liu, Z. and Y.A. Chang, *evaluation of the thermodynamic properties of the Re-Ta and Re-W systems.* Journal of Alloys and Compounds, 2000. **299**: p. 153-162.

41. Ekman, M., K. Persson, and G. Grimvall, *phase diagram and lattice instability in tungsten-rhenium alloys.* Journal of Nuclear Materials, 2000. **278**: p. 273-276.

42. Elliott, r.P., *constitution of binary alloys, first supplement*. 1965, San Francisco, USA: McGraw-Hill Book Company. 875.

43. Slater, J.C., *Atomic Radii in Crystals.* the Journal of Chemical Physics, 1964. **40**: p. 3199-3205.

44. Turchi, P.E.A. and A. Gonis, *First-principles study of stability and local order in substitutional Ta-W alloys.* Physics Review B, 2001. **64**: p. 085112.

45. Ohba & Morito Laobratory, S.U. *Crystal Structure (http://www.geocities.jp/ohba_lab_ob_page/structure6.html)*. 2000 [cited 2015.

46. Tanno, T., et al., *Precipitation of solid transmutation elements in irradiated tungsten alloys.* Materials Transactions, 2008. **49**: p. 2259-2264.

47. Berne, C., et al., *Site occupancy in the Re-W sigma phase.* Physical Review B, 2001. **64**(144103).

48. Dearnaley, G., et al., *ion implantation in solids*. defects in crystallina solids. Vol. 8. 1973, Amsterdam, Netherlands: North-Holland Publishing Company. 802.

49. Chadderton, L.T., *radiation damage in crystals*. 1965, London, UK: Spottiswoode, Ballantyne & Co Ltd. 202.

50. Thompson, M.W., *defects and radiation damage in metals*. 1969, London, UK: Cambridge University Press. 384.

51. Ziegler, J. *particle interaction with matter (http://www.srim.org)*. 2012 [cited 2012.

52. Ziegler, J.F., M.D. Ziegler, and J.P. Biersack, *SRIM - The stopping and range of ions in matter (2010).* Nuclear Instruments and Methods in Physics Research B, 2010. **268**: p. 1818-1823.

53. Humphry-Baker, S.A., *atomic scale studies of fusion materials: atom probe study of tungsten-rhenium alloys (part ii thesis)*. 2008: Oxford University. p. 121.

54. Nastasi, M., J.W. Mayer, and J.K. Hirvonen, *Ion-solid interactions: fundamentals and applications*. 1996, Cambridge, UK: Cambridge University Press. 540.

55. *proceedings of the international school of physics: radiation damage in solids*. 1960, London, UK: Academic Press. 942.

56. Danilowicz, R.L., *Point Defect Calculations in Tungsten (NASA Technical Note TN D-4918)*. 1968, National Aeronautics and Space Administration (NASA): Ohio, USA. p. 15.

57. Nguyen-Manh, D., A.P. Horsfield, and S.L. Dudarev, *self-interstitial atom defects in bcc transition metals: group-specific trends.* Physical Review B, 2006. **73**: p. 020201-1.

58. Dudarev, S.L., P.M. Derlet, and C.H. Woo, *Driven mobility of self-interstitial defects under electron irradiation.* Beam Interactions with Materials & Atoms, 2007. **256**: p. 253-259.

59. Zhou, W.H., et al., *Dynamical behaviors of self-interstitial atoms in tungsten.* Journal of Nuclear Materials, 2013. **437**: p. 438-444.

60. Kong, X.S., et al., *First-principles calculations of transition metal-solute interactions with point defects in tungsten.* Acta Materialia, 2014. **66**: p. 172-183.

61. Becquart, C.S., et al., *Microstructural evolution of irradiated tungsten: Ab initio parameterisation of an OKMC model.* Journal of nuclear materials, 2010. **403**: p. 75-88.

62. Becquart, C.S. and C. Domain, *Solute-point defect interactions in bcc systems: focusing on first principles modelling in W and RPV steels.* Current Opinion in Solid State and Materials Science, 2012. **16**: p. 115-125.

63. Herschitz, R. and D.N. Seidman, *an atomic resolution study of homogeneous radiation-induced precipitation in a neutron irradiated W-10at.%Re alloy.* Acta Metallurgica, 1984. **32**: p. 1141-1154.

64. Herschitz, R. and D.N. Seidman, *an atomic resolution study of radiation-induced precipitation and solute segregation effects in a neutron-irradiated W-25at.%Re alloy.* Acta Metallurgica, 1984. **32**: p. 1155-1171.

65. Cottrell, G.A., *Formation of WRe and WRe3 platelets in irradiated W-Re alloys.* Energy Materials, 2006. **1**: p. 245-248.

66. Cottrell, G.A., *Evolution of WRe platelets in irradiated W-Re alloys.* Energy Materials, 2008. **3**: p. 20-23.

67. Wilson, K.L., M.I. Basks, and D.N. Seidman, *An in situ field-ion microscope study of the recovery behaviour of ion-irradiated tungsten and tungsten alloys.* Acta metallurgica, 1980. **28**: p. 89-102.

68. Suvorov, A.L. and D.E. Dolin, *Field ion microscopy study of the interactions between self interstitials and impurities in metals.* applied surface science, 1996. **94/95**: p. 384-390.

69. He, J.C., A. Hasegawa, and K. Abe, *Effects of transmutation elements on the defect structure development of W irradiated by protons and neutrons.* Journal of Nuclear Materials, 2008. **377**: p. 348-351.

70. Ciupinski, L., et al., *TEM observations of radiation damage in tungsten irradiated by 20 MeV W ions.* Nuclear instruments and methods in physics research B, 2013. **317**: p. 159-164.

71. Grzonka, J., et al., *Electron microscopy observations of radiation damage in irradiated and annealed tungsten.* Nuclear Instruments and methods in physics research B, 2014. **340**(27-33).

72. Ogorodnikova, O.V., et al., *Annealing of radiation-induced damage in tungsten under and after irradiation with 20 MeV self-ions.* Journal of nuclear materials, 2014. **451**: p. 379-386.

73. Ferroni, F., et al., *High temperature annealing of ion irradiated tungsten.* Acta materialia, 2015. **90**: p. 380-393.

74. Yi, X., et al., *In situ study of self-ion irradiation damage in W and W-5Re at 500C.* Philosophical Magazine, 2012. **93**: p. 1715-1738.

75. Yi, X., et al., *Characterisation of radiation damage in W and W-based alloys from 2 MeV self-ion near-bulk implantations.* Acta Materialia, 2015. **90**: p. 163-177.

76. He, J., et al., *Fabrication and characterisation of W-Re-Os alloys for studying transmutation effects of W in fusion reactors.* Materials Transactions, 2004. **45**: p. 2657-2660.

77. He, J., et al., *Microstructural development and irradiation hardening of W and W-(3-26) wt% Re alloys after high temperature neutron irradiation to 0.15 dpa.* Nuclear Fusion, 2006. **46**: p. 877-883.

78. Tanno, T., et al., *Effects of transmutation elements on neutron irradiation hardening of tungsten.* Materials Transactions, 2007. **48**: p. 2399-2402.

79. Tanno, T., et al., *Effects of transmutation elements on the microstructural evolution and electrical resistivity of neutron-irradiated tungsten.* Journal of Nuclear Materials, 2009. **386**: p. 218-221.

80. Tanno, T., et al., *Microstructural development in neutron irradiated tungsten alloys.* Materials Transactions, 2011. **52**: p. 1447-1451.

81. Seidman, D.N., et al., *Direct observations of the primary state of radiation damage of ion-irradiated tungsten and platnum.* Nuclear instruments and methods, 1981. **182/183**: p. 477-481.

82. Wei, C.-Y., M.I. Current, and D. Seidman, *Direct observation of the primary state of damage of ion-irradiated tungsten I. Three-dimensional spatial distribution of vacancies.* Philosophica magazine, 1981. **44**: p. 459-491.

83. Sato, S., A. Kohyama, and N. Igata, *FIM investigation of radiation damage in tungsten caused by 300keV Ni+ ions.* Applied Surface Science, 1994. **76/77**: p. 285-290.

84. Hardie, C.D., et al., *Effects of irradiation temperature and dose rate on the mechanical properties of sel-fion implanted Fe and Fe-Cr alloys.* Journal of Nuclear Materials, 2013. **439**: p. 33-40.

85. Hu, R., *Irradiation effects on Fe-Cr alloys*, in *Materials*. 2012, University of Oxford: Oxford, United Kingdom. p. 244.

86. Williams, D.B. and C.B. Carter, *Transmission Electron Microscopy: A Textbook for Materials Science (2nd Edition)*. 2009, USA: Springer Science. 760.

87. Herschitz, R. and D.N. Seidman, *Radiation-induced precipitation in fast-neutron irradiated tungsten-rhenium alloys: an atom-probe field-ion microscopy study.* Nuclear instruments and methods in physics research B, 1985. **7/8**: p. 137-142.

88. Di Maio, D. and S.G. Roberts, *Measuring fracture toughness of coatings using focused-ion-beam-machined microbeams.* Journal of Materials Research, 2004. **20**: p. 299-302.

89. McCarthy, J., et al., *FIB micromachined submicron thickness cantilevers for the study of thin film properties.* Thin Solid Films, 2000. **358**: p. 146-151.

90. Vlassak, J.J. and W.D. Nix, *A new bulge test technique for the determination of young's modulus and poisson's ratio of thin films.* Journal of Materials Research, 1992. **7**: p. 3242-3249.

91. Kiener, D., et al., *A further step towards an understanding of size-dependent crystal plasticity: in situ tension experiments of minaturized single-crystal copper samples.* Acta Materialia, 2008. **56**: p. 580-592.

92. Bei, H., et al., *Compressive strengths of molybdenum alloy micro-pillars prepared using a new technique.* Scripta Materialia, 2007. **57**: p. 397-400.

93. Frick, C.P., et al., *Size effect on strength and strain hardening of small-scale [111] nickel compression pillars.* Materials Science and Engineering A, 2008. **489**: p. 319-329.

94. Armstrong, D.E.J., A.J. Wilkinson, and S.G. Roberts, *Measuring anisotropy in young's modulus of copper using microcantilever testing.* Journal of Materials Research, 2009. **24**: p. 3268-3276.

95. Oliver, M.C. and G.M. Pharr, *Improving technique for determining hardness and elastic modulus using load and displacement sensing indentation experiments.* Journal of Materials Research, 1992. **7**(6): p. 1564-1580.

96. Armstrong, D.E.J. and T.B. Britton, *Effect of dislocation density on improved radiation hardening resistance of nano-structured tungsten-rhenium.* Materials Science and Engineering: A, 2014. **611**: p. 388-393.

97. Rau, R.C., J. Moteff, and R.L. Ladd, *Comparison of microstructure with mechanical properties of irradiated tungsten.* Journal of nuclear materials, 1967. **24**: p. 164-173.

98. Rau, R.C., R.L. Ladd, and J. Moteff, *Voids in irradiated tungsten and molybdenum.* Journal of nuclear materials, 1969. **33**: p. 324-327.

99. Steichen, J.M., *Tensile properties of neutron irradiated TZM and tungsten.* Journal of Nuclear Materials, 1976. **60**: p. 13-19.

100. Research, A.M. *Tungsten/Rhenium Wire (http://www.advent-rm.com/catalogue/alloys.aspx)*. 2013 [cited 2013; Materials Supplier Company].

101. Garfinkle, M., W.R. Witzke, and W.D. Klopp *superplasticity in tungsten-rhenium alloys*. 1968. 22.

102. Klopp, W.D. *review of ductilizing of group VIA elements by rhenium and other solutes*. 1968. 32.

103. Ralph, B. and D.G. Brandon, *a field ion microscope study of some tungsten-rhenium alloys.* Philosophical Magazine, 1963. **8**: p. 919-934.

104. Field, A.L., et al., *Research and development of tantalum and tungsten based alloys*, B.o.N.W. Navy, Editor. 1961: Westinghouse Research Laboratories, Pittsburgh 35, Pennsylvania. p. 199.

105. Wurster, S., et al., *Fracture behaviour of tungsten-vanadium and tungsten-tantalum alloys and composites.* Journal of Nuclear Materials, 2011. **413**: p. 166-176.

106. Rieth, M., et al., *Recent progress in research on tungsten materials for nuclear fusion applications in europe.* Journal of Nuclear Materials, 2013. **432**: p. 482-500.

107. Hanna, L.R., *Atomic scale study of tungsten-tantalum alloys for fusion applications*, in *Materials Science*. 2013, Oxford: Oxford. p. 112.

108. Armstrong, D.E.J., A.J. Wilkinson, and S.G. Roberts, *Mechanical properties of ion-implanted tungsten-5 wt% tantalum.* Physica Scripta, 2011. **2011 (Issue T145)**: p. 014076 (4pp).

109. Villars, P., A. Prince, and H. Okamoto, *Handbook of Ternary Alloy Phase Diagrams*. 1995, Materials Park, Ohio, USA: ASM International.

110. *Osmium tetroxide(http://www.michigan.gov/documents/mdch-osmium_tetroxide_fs_109244_7.pdf)*. 2004.

111. Biochemistry, U.C.a. *standard operating procedure working with osmium tetroxide*. 2009. 5.

112. Gault, B., et al., *Atom probe microscopy*. 2012, New York, USA: Springer Science. 396.

113. Seidman, D.N., *On the point-defect annealing mechanism for stage III recovery in irradiated or quenched tungsten.* Scripta Metallurgica, 1979. **13**: p. 251-257.

114. Troev, T., N. Nankow, and T. Yoshiie, *Simulation of displacement cascades in tungsten irradiated by fusion neutrons.* Nuclear Instruments and Methods in Physics Research B, 2011. **269**: p. 566-571.

115. Schaffer, M., B. Schaffer, and Q. Ramasse, *Sample preparation for atomic-resolution STEM at low voltages by FIB.* Ultramicropscopy, 2012. **114**: p. 62-71.

116. Bas, P., et al., *a general protocol for the reconstruction of 3D atom probe data.* Applied Surface Science, 1995. **87/88**: p. 298-304.

117. Kelly, T.F. and M.K. Miller, *invited review article: atom probe tomography.* Review of Scientific Instruments, 2007. **78**: p. 031101-1.

118. Kelly, T.F. and M.K. Miller, *atom probe tomography.* Review of Scientific Instruments, 2007. **78**: p. 031101-1.

119. Miller, M.K. and G.D.W. Smith, *atom probe microanalysis: principles and applications to materials problems*. 1989, Pennsylvania, USA: Materials Research Society. 277.

120. Miller, M.K., et al., *atom probe field ion microscopy*. 1996, Oxford, UK: Oxford University Press. 509.

121. Gault, B., et al., *Influence of surface migration on the spatial resolution of pulsed laser atom probe tomography.* Journal of Applied Physics, 2010. **108**: p. 044904-1.

122. Marquis, E.A. and B. Gault, *Determination of the tip temperature in laser assisted atom-probe tomography using charge state distributions.* Journal of Applied Physics, 2008. **104**(084914).

123. Hyde, J.M., et al., *A sensitivity analysis of the maximum separation method for the characterization of solute clusters.* Ultramicroscopy, 2011. **111**: p. 440-447.

124. Styman, P.D., et al., *Quantitative methods for the APT analysis of thermally aged RPV steels.* Ultramicroscopy, 2013. **132**: p. 258-264.

125. Williams, C.A., et al., *Defining clusters in APT reconstructions of ODS steels.* Ultramicroscopy, 2012. **pii: S0304-3991(12)00298-7. doi: 10.1016**.

126. Nabarro, F.R.N., *The influence of elastic strain on the shape of particles segregating in an alloy.* Proceedings of the physics society, 1940. **52**: p. 90-93.

127. Oh-ishi, K., et al., *Effect of laser power and specimen temperature on atom probe analysis of magnesium alloys.* Ultramicroscopy, 2011. **111**: p. 715-718.

128. Kamiyama, E., et al., *Atom probe tomography study on $Ge_{1-x-y}Sn_xC_y$ heteroepitaxial film on Ge substrates.* Thin Solid Films, 2015. **592**: p. 54-58.

129. Meher, S., et al., *Determination of solute site occupancies with y' precipitates in nickel-based superalloys via orientation-specific atom probe tomography.* Ultramicroscopy, 2015. **In Press, Corrected Proof**.

130. Frost, H.J. and K.C. Russell, *Particle stability with recoil resolution.* Acta Metallurgica, 1982. **30**: p. 953-960.

131. Heinig, K.H., et al., *Interfaces under ion irradiation: growth and taming of nanostructures.* Applied Physics A: Materials Science & Processing, 2003. **77**: p. 17-25.

132. Monnet, I., et al., *Microstructural investigation of the stability under irradiation of oxide dispersion strengthened ferritic steels.* Journal of Nuclear Materials, 2004. **335**: p. 311-321.

133. Debelle, A., et al., *Helium behaviour and vacancy defect distribution in helium implanted tungsten.* Journal of Nuclear Materials, 2007. **362**: p. 181-188.

134. Debelle, A., M.F. Barthe, and T. Sauvage, *First temperature stage evolution of irradiation-induced defects in tungstne studied by positron annihilation spectroscopy.* Journal of Nuclear Materials, 2008. **376**: p. 216-221.

135. Lhuiller, P.E., et al., *Helium retention and early stages of helium-vacancy complexes formation in low energy helium-implanted tungsten.* Journal of Nuclear Materials, 2013. **433**: p. 305-313.

136. Williams, R.K., et al., *Irradiation induced precipitation in tungsten based W-Re alloys.* Metallurgical Transactions A, 1983. **14A**: p. 655-666.

137. Arkhipova, N.K., et al., *Tungstne-series impurity diffusion in single-crystal tungsten.* Physical Review B, 1984. **30**(4): p. 1788-1796.

138. Zhang, Z.W., et al., *Effects of proton irradiation on nanocluster precipitation in ferritic steel containing fcc alloying additions.* Acta Materialia, 2012. **60**: p. 3034-3046.

139. Lescoat, M.L., et al., *Radiation-induced ostwald ripening in oxide dispersion strengthened ferritic steels irradiated at high ion dose.* Acta Materialia, 2014. **78**: p. 328-340.

140. Lui, M.W. and I. Le May, *On the "friedel relation" in precipitation hardening.* Scripta Metallurgica, 1975. **9**: p. 587-589.

141. Abbaschian, R., L. Abbaschian, and R.E. Reed-Hill, *Physical Metallurgy Principles (4th Edition)*. 2010, USA: Cengage Learning. 750.

142. Ashby, M.F. and D.R.H. Jones, *Engineering Materials 1: An Introduction to Properties, Applications & Design*. 4 ed. 2012, UK: Butterworth-Heinemann. 472.

143. Russell, K.C. and L.M. Brown, *A dispersion strengthening model based on differing elastic moduli applied to the iron-copper system.* Acta Metallurgica, 1972. **20**: p. 969-974.

144. Tanno, T., et al., *Precipitation of Solid Transmutation Elements in Irradiated Tungsten Alloys.* Materials Transactions, 2008. **49**(10): p. 2259-2264.

145. Tanno, T., et al., *Effects of transmutation elements on neutron irradiation hardening of tungsten.* Materials Transactions, 2007. **48**(9): p. 2399-2402.

146. Cottrell, G.A., *sigma phase formation in irradiated tungsten, tantalum and molybdenum in a fusion power plant.* Journal of Nuclear Materials, 2004. **334**: p. 166-168.

147. Ferroni, F., E. Tarleton, and S. Fitzgerald, *Dislocation dynamics modelling of radiation damage in thin films.* Modelling and Simulation in Material Science and Engineering, 2014. **22**: p. 1-18.

148. Yoshiie, T., *Factors that influence cascade-induced defect growth in pure metals and model alloys.* Materials Transactions, 2005. **46**: p. 425-432.

149. Armstrong, D.E.J., P.D. Edmondson, and S.G. Roberts, *Effects of sequential tungsten and helium ion implantation on nano-indentation hardness of tungsten.* Applied Physics Letters, 2013. **102**: p. 251901 (DOI: 10.1063/1.4811825).